Study of neutrino interactions in the near detector of T2K

Chiraz Ferchichi

CEA, IRFU, SPP

Université Paris-Sud

A thesis submitted for the degree of

Docteur en Sciences de l'Université Paris-Sud
Spécialité : Physique des particules

Defended on June 25th, 2014 in front of the committee:
Sotiris LOUCATOS (président du jury)
Dario AUTIERO (rapporteur)
Brahim BACCARI (rapporteur)
Achille STOCCHI (examinateur)
Georges VASSEUR (directeur de thèse)

Remerciements

Ma thèse n'aurait pas existé et été terminée sans la contribution et le soutien de plusieurs personnes.

J'aimerais remercier mes rapporteurs, Dario Autiero et Brahim Baccari, qui ont pris de leur temps pour lire mon manuscrit et m'ont autorisée à soutenir cette thèse, ainsi que les autres membres de mon jury, Sotiris Loucatos et Achille Stocchi, pour avoir accepté cette tâche et pour leur présence à ma soutenance.

J'exprime ma gratitude au service de physique des particules de Saclay, surtout pour l'accueil chaleureux au début de ma thèse par Ursula Bassler et Didier Vilanova. Merci de m'avoir offert toutes les ressources nécessaires à mon travail.

J'ai une place spéciale pour mon directeur de thèse Georges Vasseur qui a encadré tout mon travail. Je le remercie énormément pour son aide durant toute ma thèse. Il a été à l'écoute de toutes mes questions et ouvert à toutes discussions en physique. Je le remercie de m'encourager à poser des questions et discuter sans me juger. Grâce à son expérience, il a su répondre à toutes mes interrogations avec beaucoup de clarté. Merci à Georges pour sa disponibilité, son sérieux et sa gentillesse. Merci pour sa patience avec moi et son calme pendant la période où je n'avançais pas. Merci pour sa compréhension. Merci à Georges qui m'a rendu confiance sous son encadrement. Pendant ma thèse, j'ai appris beaucoup de lui : l'efficacité, l'organisation, la rapidité, etc. J'ai eu de la chance de travailler avec Georges, je tenterai de m'en inspirer dans le futur.

Merci à Sandrine Emery qui m'a beaucoup aidée sur l'analyse, qui a pris cette charge avec beaucoup de responsabilité et qui a pris le

temps de m'expliquer doucement et de différentes manières. J'étais souvent éblouie par sa créativité scientifique et ses réflexions. Merci pour sa gentillesse et sa tendresse.

Je n'oublierai jamais le plaisir de la recherche que j'ai trouvé à discuter avec Georges et Sandrine dans chaque réunion. Pendant ma thèse, j'ai pensé plusieurs fois arrêter, mais à chaque fois j'ai trouvé un encouragement énorme pour finir la thèse. Jamais dans toute ma vie personne ne m'a encouragée dans mon parcours académique comme Sandrine et Georges. Au point que lorsque je pense arrêter ma thèse, je pense aussi aux aides de Georges et Sandrine. Je suis très reconnaissante envers eux.

Je dis aussi merci à tous les membres permanents du groupe T2K que j'ai côtoyés et qui m'ont toujours ouvert leur porte : Edoardo Mazzucato qui a répondu à chaque fois à mes questions sur la TPC ou les runs de T2K avec beaucoup de précision, et aussi Olivier Besida et Sara Bolognesi. Merci à mon chef d'équipe Marco Zito de m'avoir acceptée dans son équipe et de m'avoir conseillé de suivre les cours d'une école sur les neutrinos.

Je remercie également les jeunes docteurs de ce groupe T2K à Saclay, Flor de Maria Blaszczyk, Michael Macaire et Vyacheslav Galymov, et aussi Claudio Giganti et Javier Caravaca de l'expérience T2K avec qui j'ai pu souvent échanger mes questions contre des réponses au cours de ma thèse.

Merci pour ma marraine Anne-Isabelle Etienvre qui s'est continuellement souciée de mon bien-être au sein du labo et Frederic Deliot pour ses conseils.

Merci à Jean-Marc, Samira et Sotiris pour leur humanité, leurs encouragements, leurs aides et leurs conseils constructifs et rassurants. Je ne pourrai jamais assez les remercier.

Merci pour les autres membres du SPP que j'ai croisés dans le couloir et auprès de qui je trouvais toujours un sourire : Patrice Perez, Paul

Colas, Bertrand Vallage, Jean-Francois Glicenstein, Pierre Brun, ...

Merci aux doctorants et jeunes docteurs du labo : Anais Moller, Joany Manjares Ramos, Sarah Puisieux, Emilien Chapon, Fabrice Balli, Homero Martinez Bruzual, Timothée Delubac, Vincent Durand, Emilie Ramos, Léa Gauthier et surtout mon ancien collègue de bureau Denis Wouters.

Merci à Cristina Volpe pour son cours sur le neutrino. Merci à tous mes enseignants qui m'ont beaucoup appris, surtout mon père à l'école, puis ma professeure de physique-chimie au lycée Sabah, ensuite mon professeur de physique quantique Bourgou et enfin mon directeur de thèse Georges.

Merci à ma famille : à mon père et à ma mère qui m'ont beaucoup donné. Merci à mes soeurs Mouna, Imène et Rim et à mon frère Ramzi pour leurs encouragements surtout pendant ma thèse.

Finalement merci à moi.

Citations d'Albert Einstein :

"C'est le rôle essentiel du professeur d'éveiller la joie de travailler et de connaître."

"Il est plus facile de briser un atome que de briser un préjugé."

"La peur bloque la compréhension intelligente de la vie."

"Une personne qui n'a jamais commis d'erreurs n'a jamais innové."

"La valeur d'un homme réside dans ce qu'il donne et non pas dans ce qu'il est capable de recevoir."

Abstract

The T2K experiment studies the properties of neutrinos, particularly neutrino oscillations. It takes place in Japan and uses a muonic neutrino beam produced by the J-PARC accelerator complex, a near detector, ND280 on the J-PARC site in order to characterise the beam, and a far detector, Super-Kamiokande 295 km away in order to measure the neutrino oscillations. The near detector is also used to study the neutrino interactions and the goal of this thesis is the measurement of muonic neutrino deep inelastic scattering cross sections.

The thesis first introduces neutrino physics, then the T2K experiment and more particularly the time projection chambers of the near detector, and its data quality checking that I was in charge of. The analysis is based on the T2K data recorded until 2013. The selection of charged current muonic neutrino interactions is then presented, as well as a preliminary study of the selection of charged current muonic neutrino interactions with the production of a neutral pion. A criterion on track multiplicity allows enriching the former sample in interactions corresponding to a neutrino deep inelastic scattering. Finally a fit, first validated on simulated data, allows the extraction of the muonic neutrino deep inelastic scattering cross sections.

Résumé

L'expérience T2K étudie les propriétés des neutrinos, en particulier le phénomène d'oscillation des neutrinos. Se déroulant au Japon, elle utilise un faisceau de neutrinos muoniques produit par le complexe d'accélérateurs J-PARC, un détecteur proche, ND280 sur le site même de J-PARC pour caractériser le faisceau, et un détecteur lointain, Super-Kamiokande situé à 295 km pour mesurer les oscillations de neutrinos. Le détecteur proche permet également d'étudier les interactions des neutrinos et cette thèse porte sur la mesure des sections efficaces de diffusion profondément inélastique des neutrinos muoniques.

Le manuscrit commence par introduire la physique des neutrinos, puis l'expérience T2K et en particulier les chambres à projection temporelle du détecteur proche, en insistant sur la vérification de la qualité des données, dont j'avais la charge. L'analyse porte sur les données de T2K enregistrées jusqu'en 2013. La sélection d'interactions de neutrinos muoniques par courant chargé est ensuite présentée, ainsi qu'une étude préliminaire de la sélection d'interactions de neutrinos muoniques par courant chargé avec production d'un pion neutre. Un critère portant sur la multiplicité des traces permet d'enrichir le premier lot en interactions correspondant à une diffusion profondément inélastique de neutrinos. Finalement un ajustement, validé d'abord sur des données simulées, permet d'extraire les sections efficaces de diffusion profondément inélastique des neutrinos muoniques.

Contents

Introduction

During the three years of my thesis, there were a lot of progress in neutrino physics. The last unknown angle, θ_{13}, among the three mixing angles governing neutrino oscillations, was measured. By sending a muonic neutrino (ν_μ) beam produced with an accelerator and looking for electronic neutrino (ν_e) appearance in a far detector located 295 km away, the T2K experiment in Japan obtained in 2011 a first indication of a non zero value of θ_{13} with a significance of 2.5 σ. With more statistics, T2K measured θ_{13} with a significance of 7.3 σ in 2013. This was the first observation of the oscillation from ν_μ to ν_e.

In the meantime, by studying the disappearance of electronic antineutrinos produced in nuclear reactors, the Double Chooz experiment in France, the Daya Bay experiment in China, and the Reno experiment in Corea provide an independent determination of θ_{13}. The measurement of θ_{13} by reactor experiments is independent from the δ phase, the last unkown element in the PMNS unitary matrix which explains neutrino mixing. In contrast, the T2K measurement does depend upon δ through higher order terms in the probability of oscillation from ν_μ to ν_e. Therefore, by combining the two measurements, some information can be obtained to constrain the value of δ.

However, a neutrino experiment of a new generation is necessary in order to perform a full study of the δ phase. This quantity is fundamental, as it is linked to the violation of the CP symmetry, the symmetry between particles and antiparticles. An option for such a future experiment is a long baseline neutrino experiment, where a ν_μ beam is sent to a huge far detector, as in T2K. But the distance between the beam production and the far detector may reach 2300 km, as in the European LBNO project. At such distances, the interesting neutrino energy range for oscillations is around a few GeV. The main charged current

interactions of neutrinos having that energy is the charged current deep inelastic scattering. Therefore, to prepare future neutrino experiments, it is important to have a good knowledge of the cross section of this process. The goal of this thesis is to perform a measurement of the ν_μ neutrino charged current deep inelastic scattering cross section.

This measurement is done using the near detector ND280 of the T2K experiment. ND280 is located at J-PARC close to the beam production, 280 m away. Its goals are to characterise the neutrino beam before oscillation and also measure neutrino cross sections. Its tracker is based upon three time projection chambers. For one year and a half, I have been in charge of checking the data quality of the time projection chambers.

This thesis summarises my work on T2K during the three years I spent at the particle physics department of the institute of research into the fundamental laws of the Universe at the CEA research center in Saclay.

The first chapter is an introduction to neutrino physics. The T2K experiment is described in the second chapter. The third chapter gives a more detailed description of the time projection chambers. The data quality checking of these time projection chambers is reviewed in the fourth chapter. The fifth chapter explains the first step of the data analysis, which is the event selection. The tools used in the analysis are described in the sixth chapter. Finally the seventh chapter gives the results of the analysis.

Chapter 1

Neutrino physics

This chapter is an introduction to neutrino physics. In section 1.1, the main steps in the history of the neutrino are reviewed. Section 1.2 deals specifically with the neutrino oscillations: the formalism and our current knowledge. Finally, section 1.3 focuses on the interactions of neutrinos with matter.

1.1 Neutrino history

We first see in subsection 1.1.1 how the neutrino was postulated and then discovered in its different flavours. Then the history of various deficits in measured neutrino rates leading to the establishment of neutrino oscillations is described in subsection 1.1.2.

1.1.1 Discovery of neutrinos

Around 1930, the β decay was understood as the decay of one neutron within a radioactive nucleus giving a proton and an electron. The kinematics is simple for this two-body decay and the electrons resulting from this process were expected to be monoenergetic. However, a continuous energy spectrum was observed experimentally for these electrons with the expected energy being the endpoint of the spectrum, as illustrated in figure 1.1. This measurement led to a serious problem: was energy conservation violated in β decays?

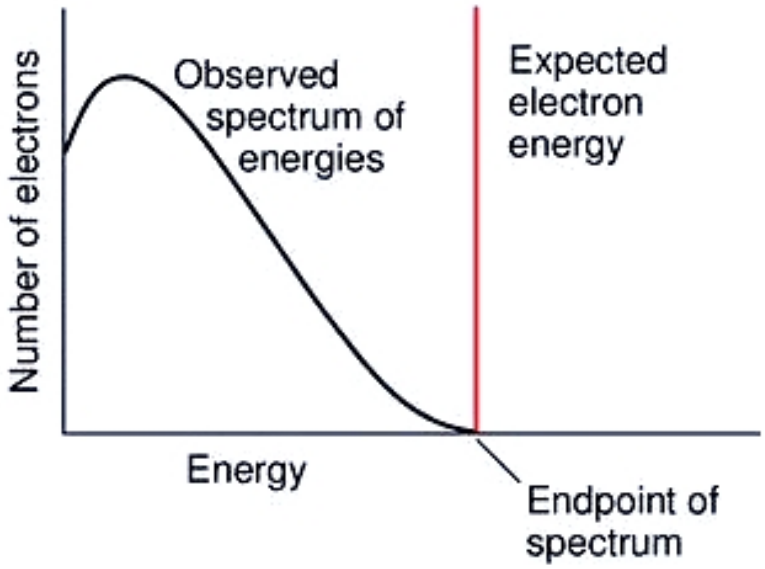

Figure 1.1: Energy spectrum of the electron from β decay. A monoenergetic spectrum was expected, but a continuous one was observed.

In order to save the principle of energy conservation, Pauli made the hypothesis in 1930 that the β decay was in fact a three-body decay [1]. The third decay product, which carries the missing fraction of the energy and no electric charge, is not detected in the experiments. The name of neutrino was given to this hypothetical particle by Fermi in 1934 [2]. It means the 'small neutral one' in Italian.

The neutrino experimental discovery occured more than twenty years afterwards. Antineutrinos produced in the Savannah River nuclear reactor (South Carolina, USA) were detected in 1956 by Reines and Cowan [3] through the inverse β reaction: $\bar{\nu}\, p \rightarrow e^+\, n$. An average rate of three interactions per hour was measured in a detector made with 4,200 liters of liquid scintillator. This was a low rate, corresponding to a very small cross section of the order of 10^{-38} cm^2. This explained why it took so much time to observe neutrino interactions.

That was not the end of the story, as a new type of neutrino was discovered in pion decays at the Brookhaven National Laboratory (USA) in 1962 [4]. While the already known neutrino, ν_e, is associated to the electron, this newly discovered

one, ν_μ, is associated to the muon. When interacting via the charged current weak intearction, described in section 1.3, it produces a muon and not an electron as ν_e does.

The neutrinos were then incorporated in the emerging Standard Model of particle physics. They were described as massless elementary particles with no electric charge (hence having no electromagnetic interactions) and no colour charge (hence having no strong interactions). Consequenlty, neutrinos interact only through the weak interaction, either via a $W^\pm$ boson or a Z^0 boson. The former interactions are called charged current interactions, while the latter are called neutral current interactions.

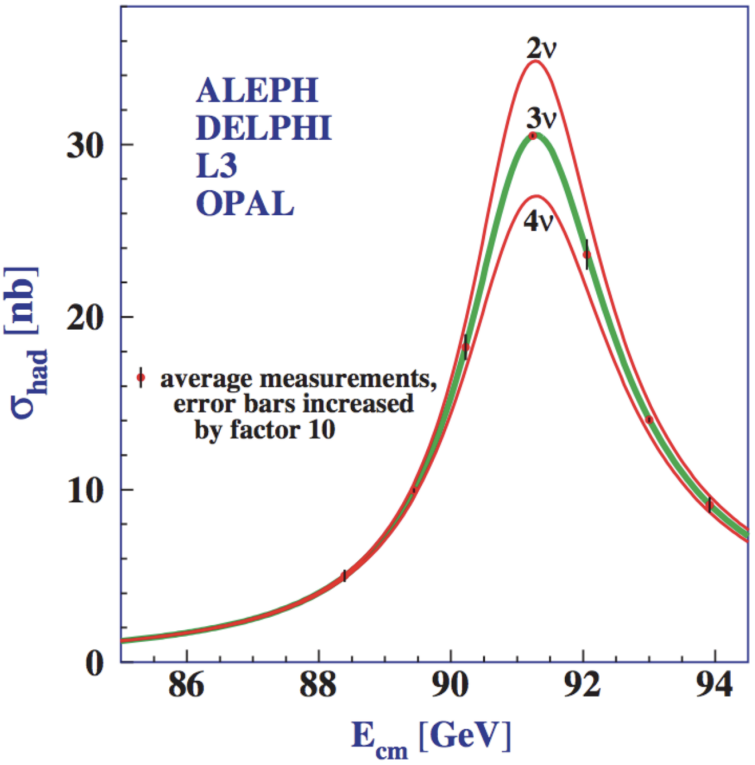

Figure 1.2: Hadronic cross section as a function of energy around the Z^0 mass. The curves show the expectation for 2, 3 (in green), and 4 neutrino flavours. The combined measurements from the four LEP experiments are given by the red points. They agree nicely with the 3 neutrino flavour hypothesis [5].

The start of the Large Electron Positron (LEP) collider at CERN (Geneva,

Switzerland) in 1989 brought new information on neutrinos. By measuring the invisible width of the Z^0 boson, as illustrated in figure 1.2, the four LEP experiments, ALEPH, DELPHI, L3, and OPAL, were able to prove that there were exactly three neutrino flavours, which coupled to the Z^0 [5]. The neutrino of the third generation, ν_τ, associated to the tau lepton, was discovered in 2001 by the DONUT experiment at Fermilab (USA) [6].

1.1.2 Do neutrinos oscillate?

1.1.2.1 Solar neutrinos

With all the fusion nuclear reactions happening inside, the Sun produces an enormous number of neutrinos. Besides, only neutrinos with the electronic flavour are produced in the Sun. The solar flux expected on the Earth was estimated at $10^8\,\nu_e$ /s/m^2. The first try to measure this flux, shown in figure 1.3, was performed by the chlorine experiment [7] at the Homestake mine (USA) starting in the late 1960s. Solar neutrinos may interact with chlorine atoms: $\nu_e + {}^{37}\mathrm{Cl} \rightarrow {}^{37}\mathrm{Ar} + e^-$. The radioactive argon atoms are chemically extracted in order to count them. However, only one third of the expected neutrinos were detected. The deficit was confirmed by other experiments based either on gallium radiochemical detectors, SAGE [8] in Baksan (Russia) and GALLEX [9] and then GNO [10] in Gran Sasso (Italy), or on water Cherenkov detectors, Kamiokande [11] followed by SuperKamiokande [12] in Kamioka (Japan). The technique of water Cherenkov detectors is explained in more details later in section 2.4.

Several explanations were proposed:

- the solar model was wrong and did not predict the correct neutrino flux from the Sun,
- a large fraction of neutrinos decay in flight,
- neutrinos can oscillate from one flavour to another,
- neutrinos have another strange and unknown feature.

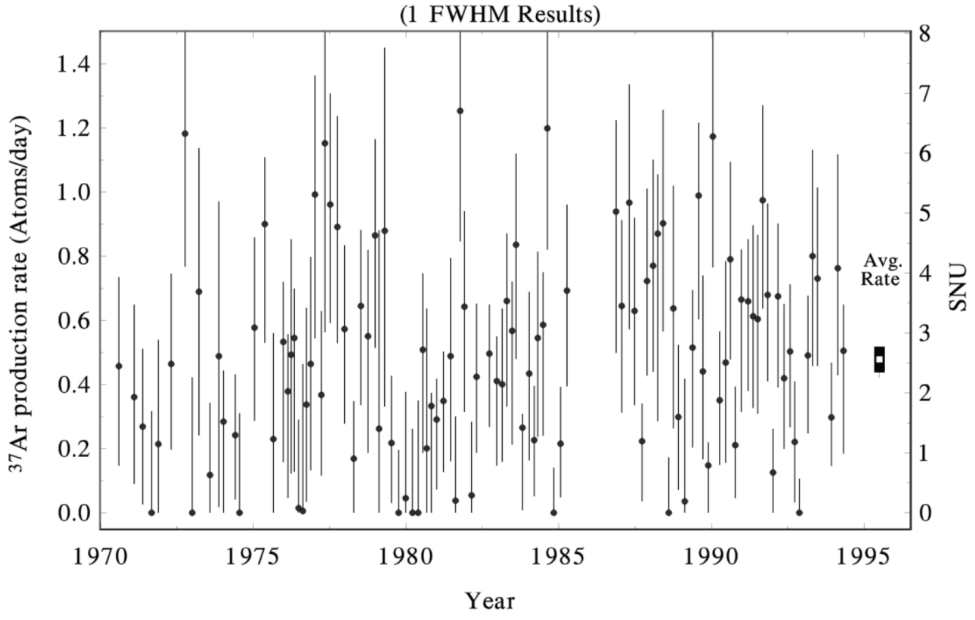

Figure 1.3: Detection rate of solar neutrinos over 25 years by the Homestake experiment.

The neutrinos produced in the Sun have an energy smaller than 20 MeV, thus smaller than the muon or tau lepton mass. So, the ν_μ or ν_τ neutrinos, which would be created through neutrino oscillation, do not have enough energy to perform a charged current interaction and produce a muon or tau lepton. Hence, the radiochemical or water Cherenkov experiments cannot detect them and are only able to measure the deficit in ν_e.

That is why the oscillation hypothesis remained controversial for a long time. It was solved by the Sudbury Neutrino Observatory (SNO) experiment [13] in 2002. The SNO detector is a water Cherenkov detector filled with heavy water, containing deuterium atoms. In addition to the usual charged current interactions producing an electron, neutrinos can also interact with a deuterium atom through a neutral current interaction, breaking it in its two constituents, the proton and the neutron, whose subsequent capture by another nucleus produces a detectable light. Thus the experiment is able to measure not only the charged current interactions, only possible for ν_e, but also the neutral current interactions, equally possible for the three neutrino types. This gives a measurement of both the ν_e

flux and the total neutrino flux. The fact that the latter was compatible with the expected solar flux, while the former was smaller, was the final proof that a substantial fraction of neutrinos, produced as ν_e in the Sun, are detected as ν_μ or ν_τ on Earth. In other words, solar neutrinos do oscillate.

1.1.2.2 Atmospheric neutrinos

A few years before the solar puzzle was solved, it was shown, by studying the so-called atmospheric neutrinos, that ν_μ neutrinos did oscillate.

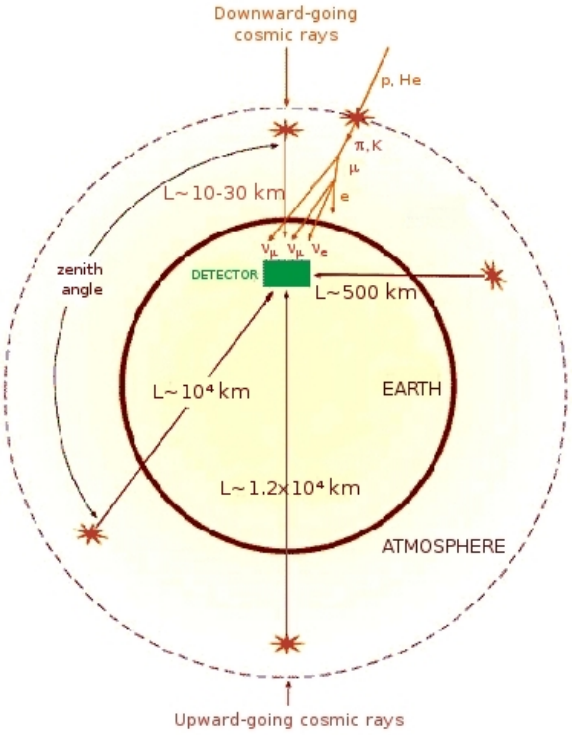

Figure 1.4: Definition of the zenith angle for atmospheric neutrinos.

The cosmics rays also produce lots of neutrinos. The cosmic rays are essentially high energy protons. When they reach the upper atmosphere of the Earth, they interact with it and produce a large number of secondary particles. Most of them are pions. The charged pions decay as $\pi^+ \rightarrow \mu^+\nu_\mu$ and $\pi^- \rightarrow \mu^-\bar{\nu}_\mu$. The

muons subsequently decay as $\mu^+ \rightarrow e^+\nu_e\bar{\nu}_\mu$ and $\mu^- \rightarrow e^-\bar{\nu}_e\nu_\mu$. So the interactions of cosmic rays in the atmosphere result in the production of atmospheric neutrinos in the ratio of one electronic neutrino for two muonic neutrinos.

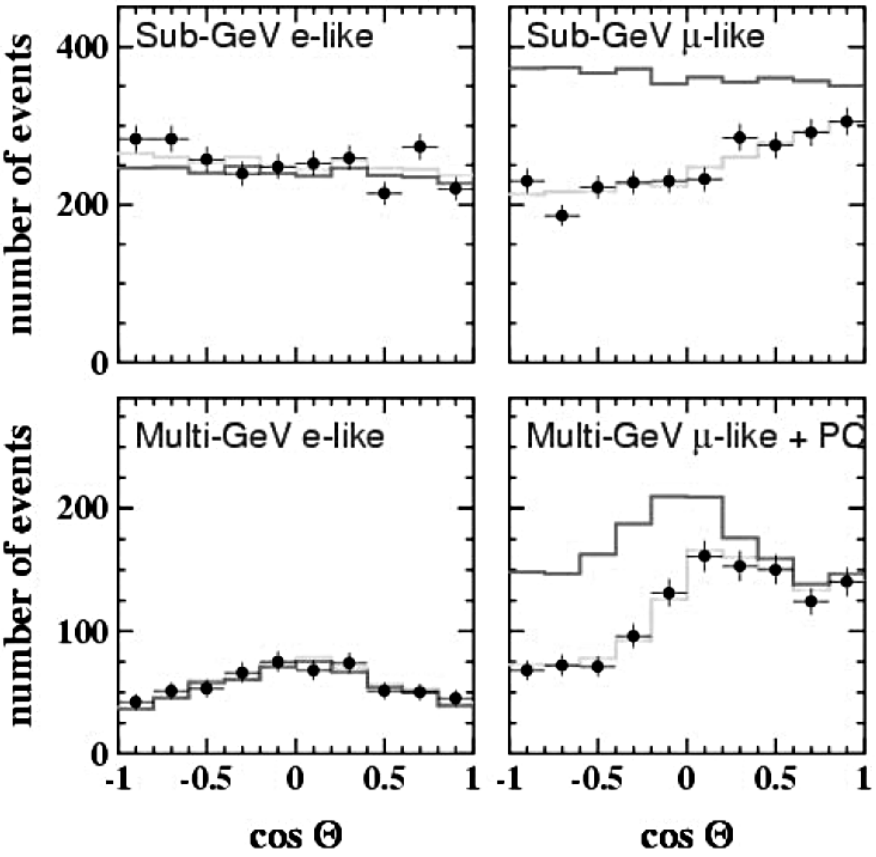

Figure 1.5: Number of neutrino interactions detected by SuperKamiokande as a function of the zenith angle for (left) ν_e and (right) ν_μ candidates in the (top) sub-GeV and (bottom) multi-GeV energy range. The solid line gives the prediction without oscillation, while the light line gives the prediction with the oscillation parameters adjusted to the best values [14].

Several water Cerenkov experiments started to detect atmospheric neutrinos and to study the ratio ν_μ over ν_e in the 1980s. As in the solar neutrino sector, there were discrepancies between the measured ratio and the expected ratio. In 1998, the SuperKamiokande experiment proved that the effect was due to

neutrino oscillation [14]. The analysis is based on the dependence of the ν_μ and ν_e spectra on the zenith angle, defined in figure 1.4. This angle is related to the distance between the neutrino production point and the detector. As illustrated in figure 1.5, the ν_e spectra is in good agreement with the prediction without oscillation, while there is a clear deficit for ν_μ candidates, especially the upward-going ones (those going through the Earth). This deficit is completely explained by an oscillation from ν_μ to ν_τ. This was the first observation of neutrino oscillation.

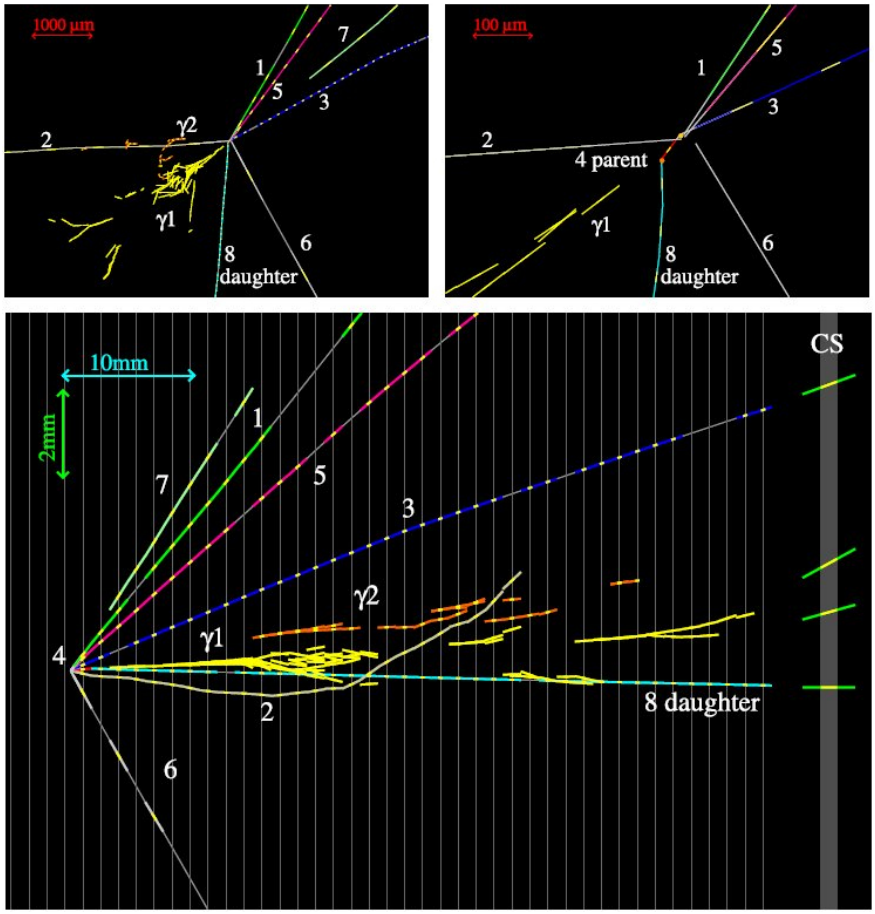

Figure 1.6: Event displays of the first ν_τ candidate from the OPERA experiment [15]. (Top) transverse views (left) unzoomed and (right) zoomed on the vertex region and (bottom) longitudinal view.

Although the atmospheric ν_μ are believed to oscillate to ν_τ, ν_τ appearance had

not been seen. This was achieved later by the OPERA experiment. Using a ν_μ beam produced at CERN, its detector in Gran Sasso National Laboratory, 730 km away, was able to detect ν_τ candidates [15], the first of which was detected in 2010 and is shown in figure 1.6. As of today, the OPERA experiment has observed four ν_τ candidates.

1.2 Neutrino oscillations

The mechanism of neutrino oscillation is introduced in subsection 1.2.1. Then the current knowledge of the neutrino oscillation parameters is described in subsection 1.2.2.

1.2.1 Mechanism

The idea of neutrino oscillation was first proposed by Pontecorvo [16] in 1957, as a $\nu - \bar{\nu}$ oscillation similar to the the $K^0 - \bar{K}^0$ oscillation. It was developped by Maki, Nagawa, and Sakata [17] and reformulated as an oscillation between the different neutrino flavours.

Neutrinos are produced and detected by weak interaction in a given flavour eigenstate: ν_e, ν_μ, or ν_τ. These flavour (or interaction) eigenstates are different from the neutrino mass (or propagation) eigenstates: ν_1, ν_2, and ν_3, with masses m_1, m_2, and m_3, respectively. The flavour eigenstates are a linear combination of the mass eigenstates. While propagating, the coefficients of the linear combination evolve since each mass eigenstate has its own frequency governing the phase evolution. This leads to a mixing process: a neutrino may be detected with a different flavour than the one initially produced. This flavour changing process, which violates the lepton number conservation, is known as neutrino oscillation.

The relation between the mass eigenstates and the flavour eigenstates is given by the Pontecorvo-Maki-Nagawa-Sakata (PMNS) matrix U_{PMNS} :

$$\begin{pmatrix} \nu_e \\ \nu_\mu \\ \nu_\tau \end{pmatrix} = \begin{pmatrix} U_{e1} & U_{e2} & U_{e3} \\ U_{\mu 1} & U_{\mu 2} & U_{\mu 3} \\ U_{\tau 1} & U_{\tau 2} & U_{\tau 3} \end{pmatrix} \begin{pmatrix} \nu_1 \\ \nu_2 \\ \nu_3 \end{pmatrix}. \tag{1.1}$$

The PMNS matrix is the equivalent in the neutrino sector of the Cabibbo-Kobayashi-Maskawa (CKM) matrix in the quark sector [18]. It is a unitary matrix: $U^{\dagger}_{PMNS}U_{PMNS} = 1$. It can be parametrised with three mixing angles, θ_{12}, θ_{13}, and θ_{23}, and one phase δ. (Note that there are two additional phases in case the neutrino is its own antiparticle; however these two phases play no role in neutrino oscillations.) The PMNS matrix is often written as:

$$U_{PMNS} = \begin{pmatrix} 1 & 0 & 0 \\ 0 & c_{23} & s_{23} \\ 0 & -s_{23} & c_{23} \end{pmatrix} \begin{pmatrix} c_{13} & 0 & s_{13}e^{-i\delta} \\ 0 & 1 & 0 \\ -s_{13}e^{i\delta} & 0 & c_{13} \end{pmatrix} \begin{pmatrix} c_{12} & s_{12} & 0 \\ -s_{12} & c_{12} & 0 \\ 0 & 0 & 1 \end{pmatrix} \tag{1.2}$$

with $c_{ij} = \cos\theta_{ij}$ and $s_{ij} = \sin\theta_{ij}$.

The oscillation probability for a flavour eigenstate α to oscillate into a flavour eigenstate β is given by:

$$\begin{aligned} P(\nu_\alpha \to \nu_\beta; L, E) \quad &= \delta_{\alpha\beta} - 4\sum_{i>j} \Re(U^*_{\alpha i}U_{\beta i}U_{\alpha j}U^*_{\beta j}) \sin^2[1.27\Delta m^2_{ij}(L/E)] \\ &\quad +2\sum_{i>j} \Im(U^*_{\alpha i}U_{\beta i}U_{\alpha j}U^*_{\beta j}) \sin[2.54\Delta m^2_{ij}(L/E)] \end{aligned} \tag{1.3}$$

where $\Delta m^2_{ij} = m^2_i - m^2_j$ is expressed in eV^2, the propagation length L in km, and the initial neutrino energy E in GeV.

In particular, the two relevant oscillation probabilities for the T2K experiment are, when neglecting higher order effects:

- the ν_μ disappearance probability, whose measurement allows a precise determination of the so-called atmospheric neutrino parameters, θ_{23} and Δm^2_{32}:

$$P(\nu_\mu \to \nu_\mu) \cong 1 - \sin^2(2\theta_{23}) \sin^2\left(1.27\Delta m^2_{32}\frac{L}{E}\right), \tag{1.4}$$

- the ν_e appearance probability, whose determination allows a measurement of θ_{13}, which was unkown at the beginning of the experiment:

$$P(\nu_\mu \to \nu_e) \cong \sin^2(2\theta_{13}) \sin^2(\theta_{23}) \sin^2\left(1.27\Delta m^2_{31}\frac{L}{E}\right). \tag{1.5}$$

1.2.2 Current knowledge

1.2.2.1 Measurement of θ_{12}

The solar neutrino oscillation (the disappearance of ν_e coming from the Sun) is governed by the parameters θ_{12} and Δm^2_{21}. It can also been studied using the $\bar{\nu}_e$ coming from nuclear reactors, as in the KamLAND experiment [19], which uses a 1 kton scintillating liquid detector and takes place in Kamioka in Japan. The solar neutrino experiments give a better constraint on θ_{12}, while KamLAND provides a very precise determination of Δm^2_{21} [20], as illustrated in figure 1.7.

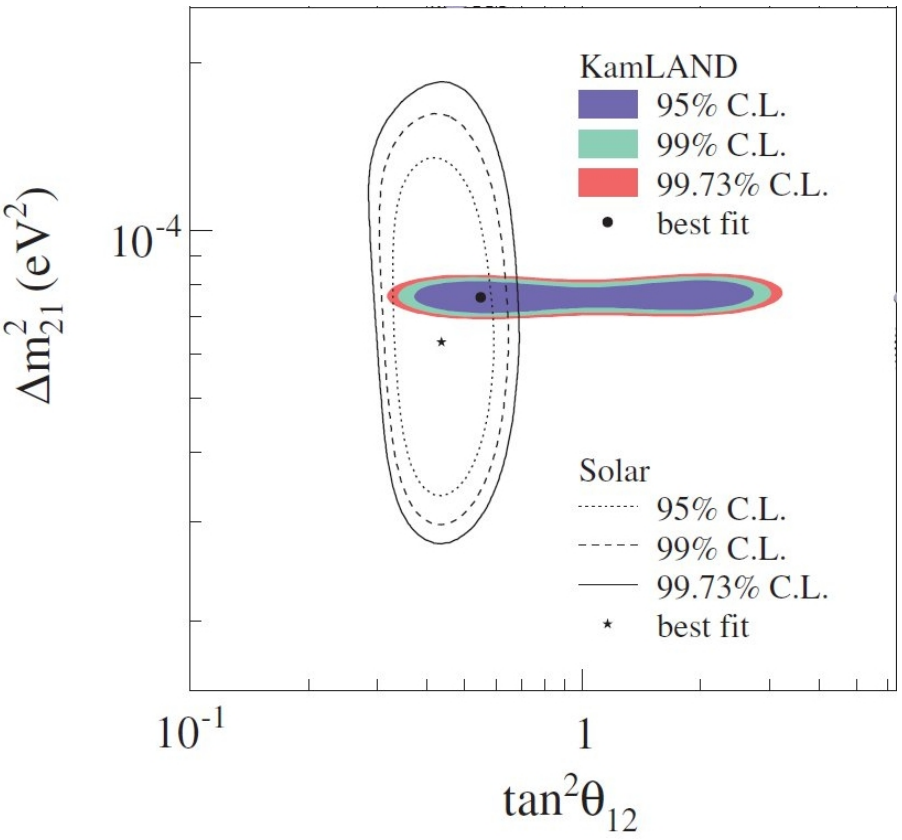

Figure 1.7: Constraints on the oscillation parameters $\tan^2\theta_{12}$ and Δm^2_{21} coming from the solar and KamLAND experiments [20].

The best measurement of these two parameters comes from a global fit, including all solar neutrino experiments and the KamLAND experiment, which

gives [21]:

$$\sin^2 2\theta_{12} = 0.857 \pm 0.024 \text{ and } \Delta m^2_{21} = (7.5 \pm 0.2) \times 10^{-5} \text{ eV}^2/c^4. \quad (1.6)$$

This corresponds to a value of $\theta_{12} = (34 \pm 1)^\circ$.

1.2.2.2 Measurement of θ_{23}

The atmospheric neutrino oscillation (the disappearance of ν_μ produced in the atmosphere by cosmic rays) is governed by the parameters θ_{23} and Δm^2_{32}. As seen in subsection 1.1.2, these parameters have been first measured by Superkamiokande. This oscillation can also been studied in experiments using a ν_μ beam produced by an accelerator by looking for ν_μ disappearance. This was pioneered by K2K [22], using a beam from KEK in Japan sent to the SuperKamiokande detector. MINOS [23] is a similar experiment in the United States, using a beam from Fermilab sent to a 5.4 kton iron-scintillator detector in the Soudan mine 735 km away. And of course, the T2K experiment, which will be described in much more details in chapter 2, is also performing this measurement.

Currently, as illustrated in figure 1.8, the MINOS experiments gives a slightly better constraint on $|\Delta m^2_{32}|$, while T2K has just published the best determination of θ_{23} [24]. The T2K results are:

$$\sin^2 \theta_{23} = 0.51 \pm 0.06 \text{ and } |\Delta m^2_{32}| = (2.5 \pm 0.1) \times 10^{-3} \text{ eV}^2/c^4. \quad (1.7)$$

As a value close to 45° is found for θ_{23}, the result is expressed as a function of $\sin^2 \theta_{23}$, rather than as a function of $\sin^2 2\theta_{23} = 4 \sin^2 \theta_{23}(1 - \sin^2 \theta_{23}) \sim 1$.

Note that only the absolute value $|\Delta m^2_{32}|$ is determined in all these experiments. Consequently, there are two possibilities for the mass ordering:

- the normal hierarchy (NH), if $m_2 < m_3$,
- the inverted hierarchy (IH), if $m_2 > m_3$.

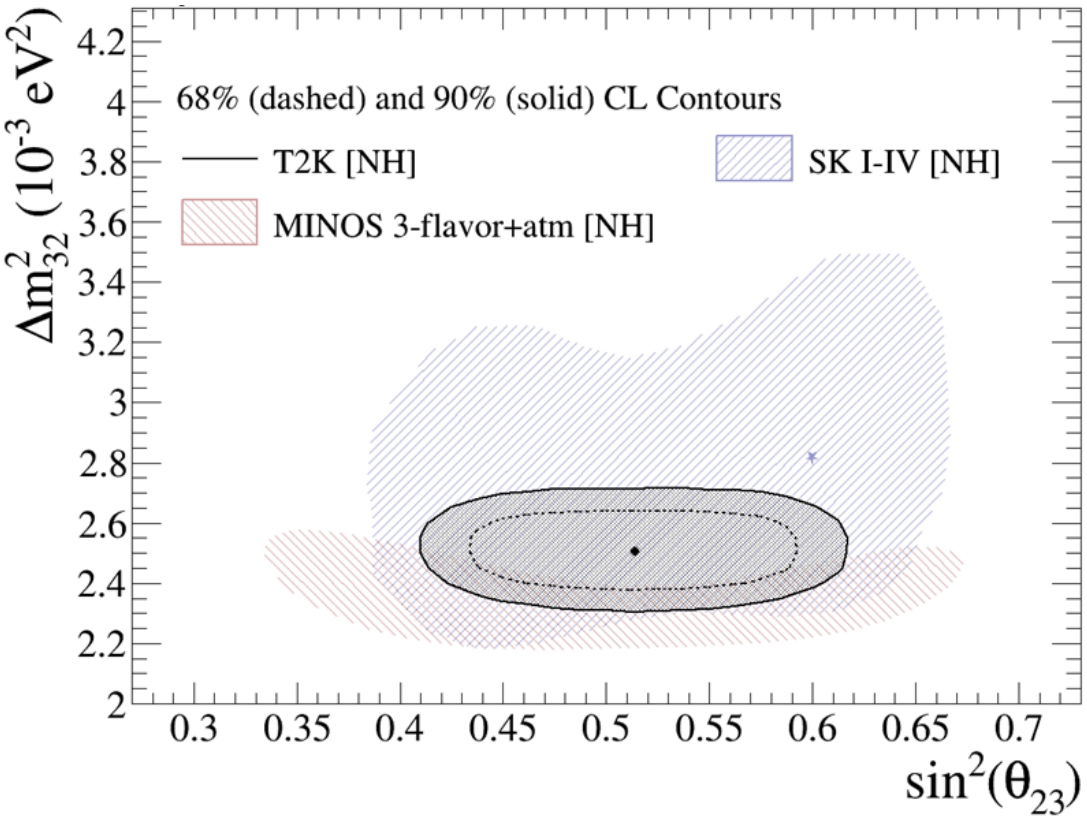

Figure 1.8: Constraints on the oscillation parameters $\sin^2\theta_{23}$ and $|\Delta m^2_{32}|$ coming from the T2K, MINOS, and SuperKamiokande experiments assuming normal hierarchy (NH). The regions shown for MINOS and SuperKamiokande are at 90 % CL, while the contours for T2K corresponds to (dashed line) 68 % CL and (solid line) 90 % CL [24].

1.2.2.3 Measurement of θ_{13}

Almost all of the ν_μ disappearance is due to the oscillation into ν_τ, seen in the previous subsection. However a tiny fraction of ν_μ oscillates to ν_e. This oscillation is governed by the parameters θ_{13} and Δm^2_{31}. As $\Delta m^2_{21} << \Delta m^2_{32}$, we already know $\Delta m^2_{31} \sim \Delta m^2_{32}$. The parameter θ_{13} was unknown until 2011.

Two ways are pursued to measure it. The first one is to look for ν_e appearance in a ν_μ beam. This is what T2K is doing. This provides a measurement of θ_{13} which depends upon the δ phase and the neutrino mass hierarchy through higher

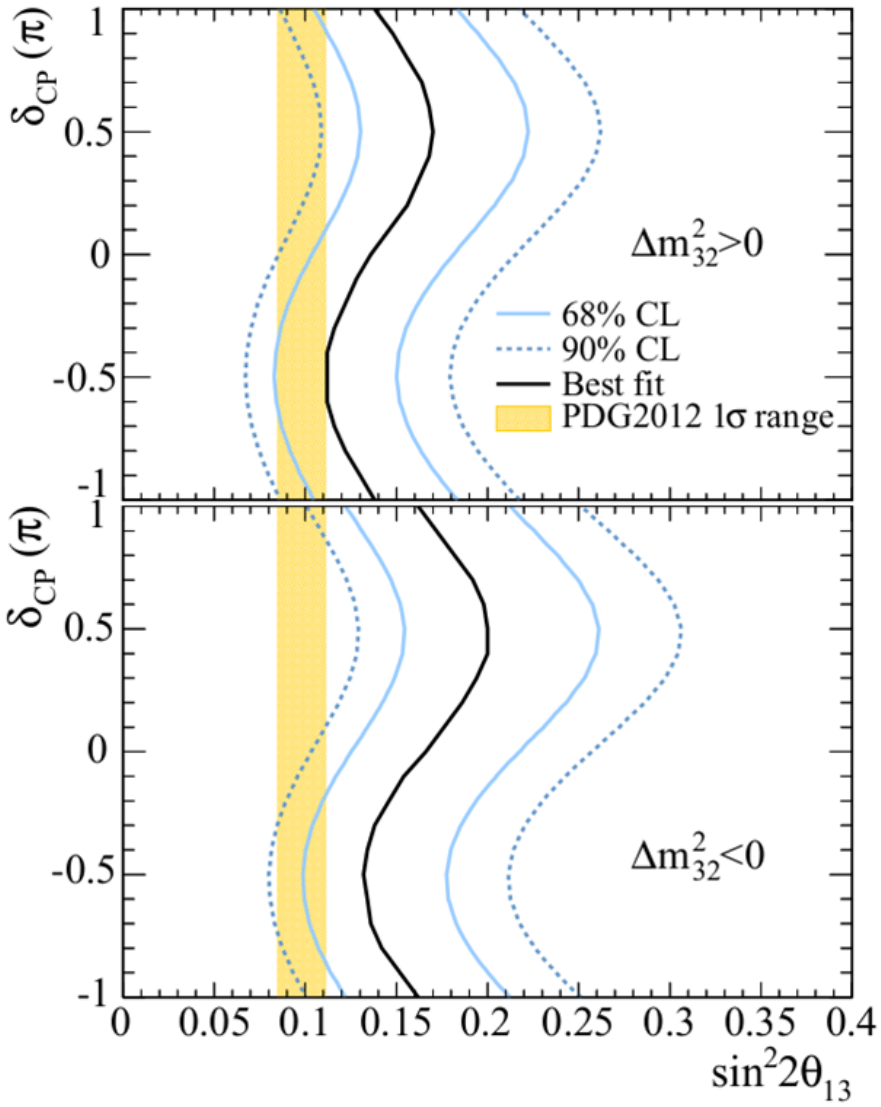

Figure 1.9: Constraints on the oscillation parameters $\sin^2\theta_{13}$ as a function of the δ phase in case of (top) normal hierarchy and (bottom) inverted hierarchy. The yellow band is from the reactor experiments. The solid black line shows the result of the T2K best fit, while the solid (dotted) blue lines give the allowed region at 68 % (90 %) CL [25].

order terms. The second one is to look for the disappearance of $\bar{\nu}_e$ produced in nuclear reactors. This gives a measurement of θ_{13} independent from δ. Such

measurements are performed by the Double Chooz experiment in France [26], the Daya Bay experiment in China [27], which provides the most precise determination, and the Reno experiment in Corea [28]. The world average of the reactor experiment is: $\sin^2 2\theta_{13} = 0.095 \pm 0.010$, corresponding to a value of θ_{13} around $9°$.

By detecting 28 ν_e candidates in the SuperKamiokande detector with an expected background smalller than 5, T2K observed for the first time electronic neutrino appearance in a muonic neutrino beam with a significance of 7.3 σ [25]. This corresponds to a value of:

- assuming $\delta = 0$ and normal hierarchy, $\sin^2 2\theta_{13} = 0.14 \pm 0.04$;
- assuming $\delta = 0$ and inverted hierarchy, $\sin^2 2\theta_{13} = 0.17 \pm 0.04$.

The best value of $\sin^2 2\theta_{13}$ is given in figure 1.9 as a function of δ both for normal hierarchy and inverted hierarchy.

1.2.2.4 Measurement of δ

As the result on $\sin^2 2\theta_{13}$ from the reactor experiments does not depend upon δ and the result from T2K does, combining them gives information on the phase δ. Furthermore, there is some tension between both results for some values of δ, especially in the case of inverted hierarchy, as shown in figure 1.9.

Consequently some ranges on the phase δ can already been excluded at the 90 % confidence level (CL):

- $[0.19\pi, 0.80\pi]$ for normal hierarchy,
- $[-0.04\pi, 1.03\pi]$ for inverted hierarchy.

This is illustrated in figure 1.10. So a negative value of δ is somewhat favoured by current data.

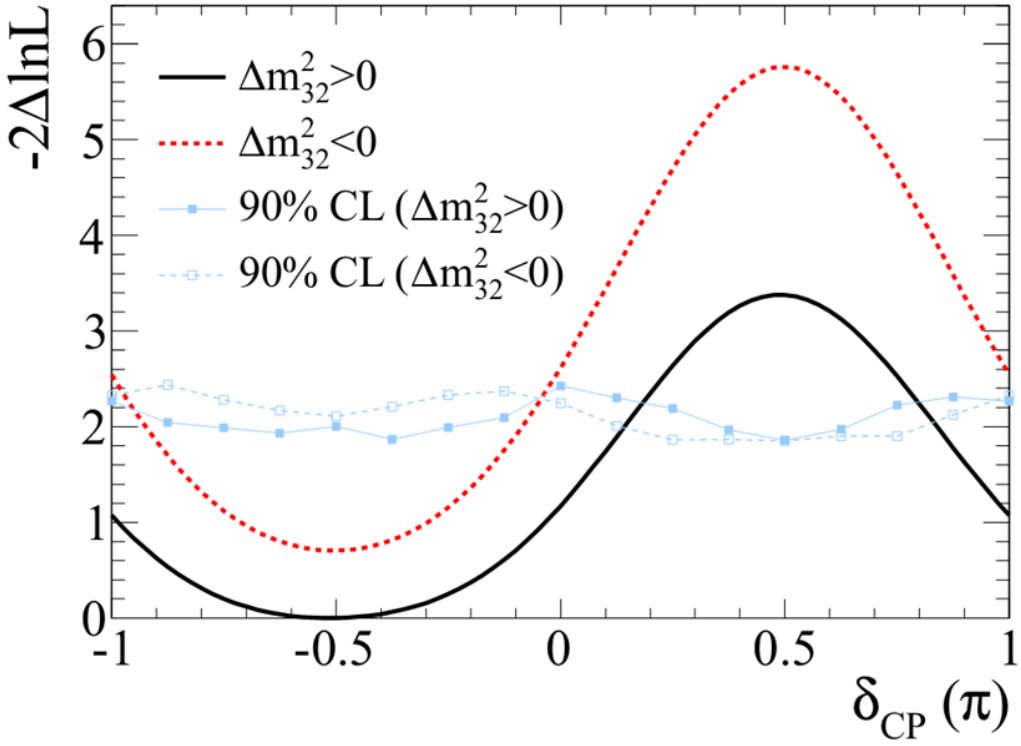

Figure 1.10: Constraints on the phase δ in case of normal (solid lines) or inverted (dotted lines) hierarchy. The regions excluded at 90 % CL are those where the curve showing the log likelihood difference with respect to the minimum is above the almost flat line indicating the 90 % CL limit.

1.3 Neutrino-nucleus interactions

Since the detection of neutrino is done through their interactions via the weak interaction with the nuclei present in the detector, experiments aiming for precision study of neutrino oscillations, such as T2K, require an accurate knowledge on neutrino-nucleus interaction cross sections. The models used in this field are introduced in subsection 1.3.1. Then subsection 1.3.2 focuses on charged current interactions, mediated by a $W^{\pm}$ boson, while subsection 1.3.3 mentions neutral current interactions, mediated by a Z^0 boson.

1.3.1 Models

As neutrinos interact with a quark inside a nucleon, itself part of a nucleus, a good knowledge of the nuclear environment has to be reached to understand the neutrino interaction cross sections. But the description of the nuclear structure and dynamics is complex because of the nature of strong interactions and also the complexity of the quantum mechanical many-body problem. Therefore the theoretical model chosen to describe the nucleus and the nucleon-nucleon interactions will have a great impact on both the predictions and the systematic errors, which limit the precision on any measurement involving the interaction with a nucleus.

However, it is possible to describe the most important features of nuclear dynamics using an independent particle model, where the nucleon-nucleon potential is replaced with a mean field. The simplest model which uses the independent particle approach is the relativistic Fermi gas model (RFG), in which the nucleus is seen as a degenerate Fermi gas of neutrons and protons, bound with a constant energy. This average binding energy and the Fermi momentum of the nucleus are specific to each nucleus. The model takes into account the fermionic nature of the nucleons by including Pauli blocking: two identical nucleons may not occupy the same quantum state simultaneously. The most commonly used version of this model is the Smith and Moniz model [29]. Although electron scattering experiments proved that this simple model did not describe electron-nucleus scattering well, previous neutrino scattering experiments have not yet demonstrated model deficiencies.

The NEUT neutrino Monte Carlo generator [30] used by the T2K experiment to predict the rates and kinematics of the various neutrino interaction modes is based on the Smith and Moniz prescription to model the nuclear environment. In this section, the choices made in NEUT are underlined for the most common neutrino-nucleus interaction channels, that will be used in the analyses described later on.

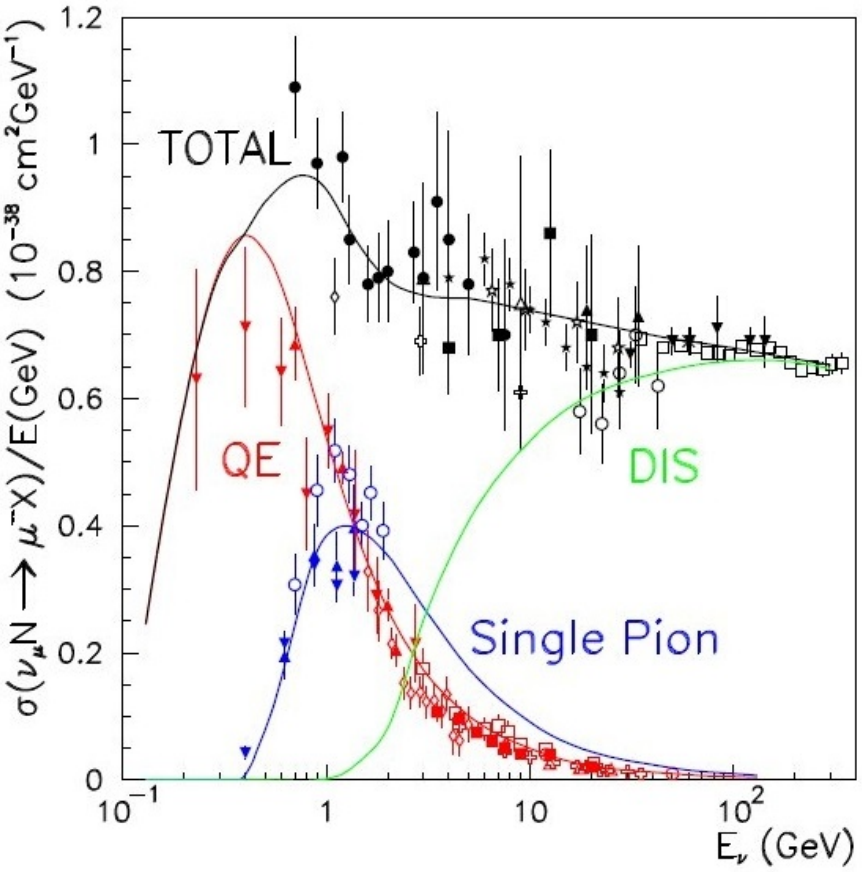

Figure 1.11: Charged current ν_μ cross sections measured by past experiments. The curves give the ratio of cross section per nucleon over neutrino energy as a function of neutrino energy. The total charged current cross section is shown in black, as well as its main components: quasi-elastic (QE) in red, single pion in blue, and deep inelastic scattering (DIS) in green [31].

1.3.2 Charged current interactions

Charged current interactions happen when the neutrino exchanges a $W^\pm$ boson with a nucleon and turns into its corresponding charged lepton partner after the interaction. At the lowest order of approximation, with the exchange of one intermediate boson and the assumption that the neutrino and outgoing charged lepton can be described as a plane wave free state (Born approximation), the cross section of the weak charged current process $\nu_l + A \rightarrow l^- + X$ can be written

as

$$\frac{d^2\sigma}{d\Omega_l dE_l} = \frac{G_F^2 V_{ud}^2}{16\pi^2} \frac{|\overrightarrow{k}_l|}{|\overrightarrow{k}|} L_{\mu\nu} W_A^{\mu\nu} \tag{1.8}$$

where the tensor $L_{\mu\nu}$ is specified by the measured lepton kinematical variables, the tensor $W^{\mu\nu}$ contains all the target structure information including the initial and final nuclear states, G_F is the Fermi constant, V_{ud} is the CKM matrix element coupling the up and down quarks, and $\overrightarrow{k}$ and $\overrightarrow{k}_l$ denote the momenta of the incoming neutrino and the outgoing charged lepton respectively [32].

The total charged current neutrino cross section increases with the neutrino energy. As shown in figure 1.11, the ratio of the total charged current cross section for ν_μ over the neutrino energy is below $10^{-38}\text{cm}^2/\text{GeV}$ for all the range in energy [31]. The quasi-elastic (QE) channel, described in subsection 1.3.2.1 is the most frequent below 1 GeV. The channels which lead to the production of a single pion in the final state, dealt with in subsection 1.3.2.2, are important in the region around 1 GeV. Finally the deep inelastic scattering (DIS) process, which produces several hadrons in the final state and is covered in subsection 1.3.2.3, is the most important at high energy. The measurement of the charged current deep inelastic scattering cross section is the goal of this thesis. Consequently this process is our signal and all other charged current interactions, as well as the neutral current interactions introduced in subsection 1.3.3, are background for our study.

Nevertheless, once the neutrino has interacted with the nucleon, the produced hadrons can be scattered and eventually re-absorbed by the nuclear medium. These secondary interactions are the final state interactions (FSI). As they might mask the true topology of the event, they add an extra level of complexity to the cross section study.

1.3.2.1 Charged current quasi-elastic interactions

The charged current quasi-elastic (CCQE) process, $\nu_\mu + n \rightarrow \mu^- + p$, is illustrated in figure 1.12. Its simple final state allows an accurate reconstruction of the neutrino energy using only the measured momentum and angle of the outgoing lepton with respect to the incoming neutrino. In this case, the neutrino energy

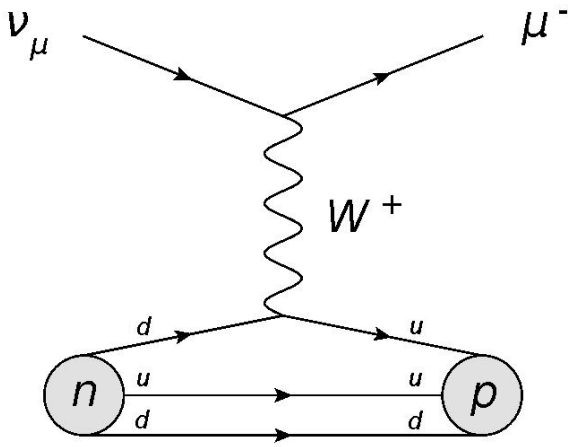

Figure 1.12: Charged current quasi-elastic Feynman diagram.

can be written as

$$E_\nu^{CCQE} = \frac{m_P^2 - m_\mu^2 - E_N^2 + 2E_\mu E_N - 2\boldsymbol{p}_\mu \cdot \boldsymbol{p}_N + |\boldsymbol{p}_N|^2}{2(E_N - E_\mu + |\boldsymbol{p}_\mu| \cos\theta_\mu - |\boldsymbol{p}_N| \cos\theta_N)} \tag{1.9}$$

where E_μ and $\boldsymbol{p}_\mu$ are the energy and momentum of the outgoing muon, θ_μ is the angle of the muon with respect to the incoming neutrino, m_P and m_μ denote the proton and muon mass, and $\boldsymbol{p}_N$ and E_N are the momentum and energy carried by the struck neutron. If we consider that the neutron is at rest, i.e. $|\boldsymbol{p}_N| = 0$, and that the neutron binding energy correction from the relativistic Fermi gas model used is a constant value ϵ, then $E_N = m_N - \epsilon$, where m_N is the neutron mass. The binding energy is $\epsilon = 25$ MeV for carbon nuclei [33], the most abundant nuclei in our case since the FGDs are mainly made of plastic scintillator bars. The equation 1.9 can therefore be reduced to:

$$E_\nu^{CCQE} \cong \frac{m_P^2 - m_\mu^2 - E_N^2 + 2E_N E_\mu}{2(E_N - E_\mu + \boldsymbol{p}_\mu \cos\theta_\mu)} \tag{1.10}$$

The neutrino-nucleon CCQE scattering cross section is very often written according to the Llewelyn-Smith formalism [34], which parametrises the cross section in terms of several Lorentz-invariant form factors which are functions of Q^2, the squared four-momentum transferred to the nuclear system. These form

factors can be divided into two types: the vector form factors and the axial form factor. While the vector form factors can be extracted from electron scattering measurements on proton and deuteron targets with great accuracy, the axial form factor must be measured by neutrino scattering experiments. This axial form factor is assumed to have a dipole form and can be written as

$$F_A(Q^2) = \frac{F_A(Q^2 = 0)}{[1 + Q^2/(M_A^{QE})^2]^2} \tag{1.11}$$

where M_A^{QE} is the axial mass parameter. The value for the axial mass can be extracted from reconstructed Q^2 distributions.

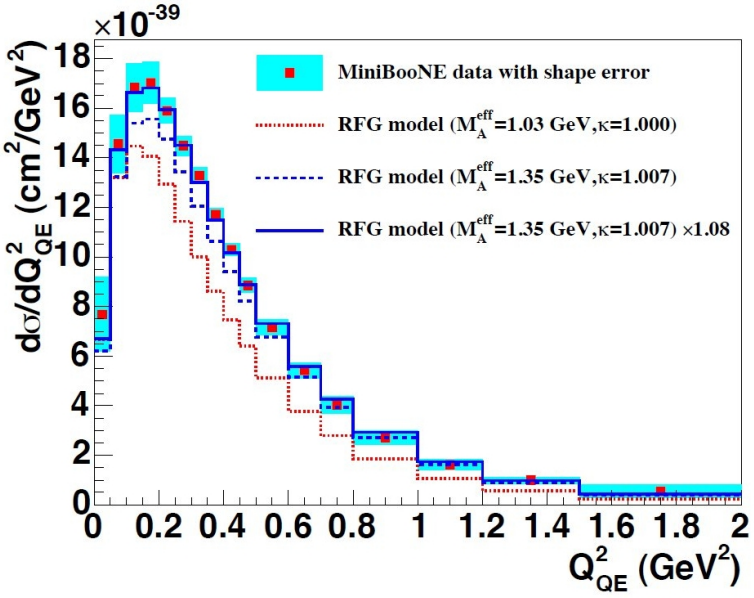

Figure 1.13: Flux integrated differential cross section per target neutron for the ν_μ CCQE process by the MiniBooNE experiment and comparison with the RFG model using different parameters. The data favour a high value of M_A^{QE} [35].

There are discrepancies between the various experimental measurements of the axial mass, a detailed review of which can be found in [36]. They range from $M_A^{QE} = 1.014 \pm 0.026\text{GeV/c}^2$ by old bubble chamber experiments [37] or $M_A^{QE} = 1.05 \pm 0.02(\text{stat}) \pm 0.06(\text{syst})\,\text{GeV/c}^2$ by the NOMAD experiment [38] to $M_A^{QE} = 1.35 \pm 0.17\,\text{GeV/c}^2$ by the MiniBooNE experiment [35]. MiniBooNE uses

the Fermilab ν_μ beam and a mineral oil Cerenkov detector. Its results are shown in figure 1.13. Given these discrepancies as well as the theoretical uncertainties, the NEUT generator chose to take a medium value $M_A^{QE} = 1.21 \pm 0.20\text{GeV/c}^2$.

1.3.2.2 Charged current single pion production

The charged current single pion (CC1π) production processes include

- $\nu_\mu + n \rightarrow \mu^- + n + \pi^+$,
- $\nu_\mu + p \rightarrow \mu^- + p + \pi^+$,
- $\nu_\mu + n \rightarrow \mu^- + p + \pi^0$.

The last two are illustrated in figure 1.14. Compared to CCQE, these interactions have only one additional particle in the final state. The interaction of the neutrino with a single nucleon proceeds through the creation of a Δ^{++} or Δ^+ resonance, decaying into a proton and a pion.

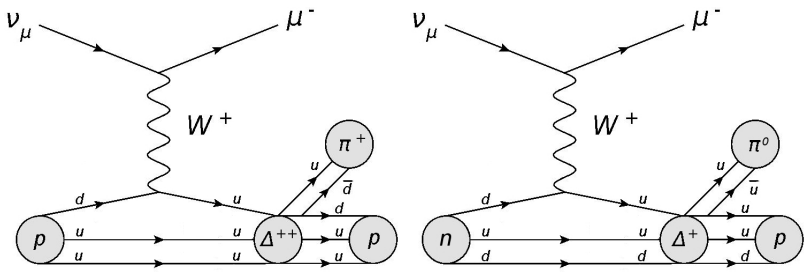

Figure 1.14: Single pion production Feynman diagrams: (a) π^+ production through Δ^{++} resonance (similar diagram for $\nu_\mu + n \rightarrow \mu^- + \Delta^+ \rightarrow \mu^- + n + \pi^+$), (b) π^0 production through Δ^+ resonance.

The most commonly used model for predicting the CC1π^+ cross section, rate, and kinematics of the final state particles, is the Rein and Sehgal (RS) model [39]. As in the CCQE cross section parametrisation, the RS model uses form factors which are assumed to have dipole forms dependent on mass parameters. So far, there are no direct measurements of the resonant axial mass M_A^{RES}. However, MiniBooNE measurements [40] favour once again a high M_A^{RES} value. That is why the NEUT generator chose to set $M_A^{RES} = 1.21 \pm 0.20\text{GeV/c}^2$.

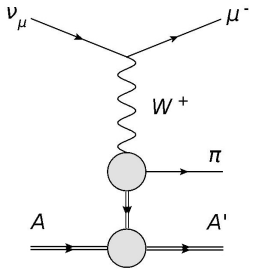

Figure 1.15: Coherent π production Feynman diagram.

Single pion production can also happen through coherent scattering. It means that the neutrino interacts with the nucleus as a whole, i.e. with all nucleons coherently, to produce a pion, as shown in figure 1.15. The nucleus is left in its ground state after the scattering, so the process has a low momentum transfer. The model used is still the Rein and Sehgal model. The M_A^{COH} parameter has a value of $1.0 \pm 0.5 \mathrm{GeV/c^2}$ in the NEUT generator, which is the default value recommended by the RS model. Coherent pion production has not been experimentally observed yet.

1.3.2.3 Deep inelastic scattering and multi-pion production

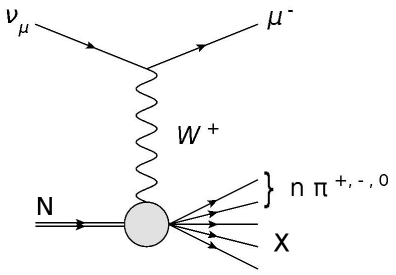

Figure 1.16: Charged current deep inelastic scattering Feynman diagram.

The deep inelastic scattering (DIS) process has been used for a long time to validate the Standard Model and to probe the insides of hadrons. With a perturbative QCD approach, the structure of the nucleons can be determined by measuring the structure functions (SF) $2xF_1(x,Q^2)$, $F_2(x,Q^2)$, and $xF_3(x,Q^2)$. The scattering particle, which can be an electron, a muon, or a neutrino, collides

onto the neutron or proton and shatters it producing several kaons, pions, and other particles. In our case, the scattering particle is a neutrino and the CCDIS process can be written as $\nu_\mu + N \rightarrow \mu^- + X$. It is illustrated in figure 1.16.

The kinematics of the DIS can be described by the Bjorken scaling variable x, the inelasticity y, and the squared four momentum transferred to the hadronic system Q^2. In terms of the laboratory frame variables, these Lorentz invariants can be expressed as:

$$x = \frac{4E_\nu E_\mu \sin^2 \frac{\theta_\mu}{2}}{2ME_{HAD}}, \;\; y = \frac{E_{HAD}}{E_\nu}, \;\; \text{and} \;\; Q^2 = 2MxyE_\nu \tag{1.12}$$

where E_ν is the incident neutrino energy, E_μ and θ_μ are the energy and the angle of the outgoing muon, E_{HAD} is the energy of the hadronic system, and M is the mass of the nucleon. With these variables, the neutrino CC double differential cross section can be written as a function of the nucleon SF:

$$\frac{d^2\sigma}{dxdy} = \frac{G_F^2 M E_\nu}{\pi \left(1 + \frac{Q^2}{M_{W,Z}^2}\right)^2} \left(\frac{y^2}{2} 2xF_1 + \left[1 - y - \frac{M_{xy}}{2E}\right] F_2 \pm \left[y - \frac{y^2}{2}\right] xF_3 \right) \tag{1.13}$$

where G_F is the Fermi weak coupling constant. A review of the theory and neutrino-nucleus DIS experimental results can be found in [41].

Deep inelastic scattering processes require a minimum energy. For example, the NEUT generator requires the hadronic invariant mass W to be larger than 1.3 GeV/c^2. The multiplicity of pions is restricted to be larger than or equal to two for 1.3 < W <2.0 GeV/c^2, since single pion production is already covered by the RS model as described in the previous section.

1.3.3 Neutral current interactions

Neutral current interactions happen when the neutrino exchanges a Z^0 with a nucleon. In this case there is no outgoing charged lepton, but an outgoing neutrino, which escapes from the detector. A single hadron or multiple hadrons may be produced. Neutral current interactions can be divided into various types, similarly to the charged current intearctions.

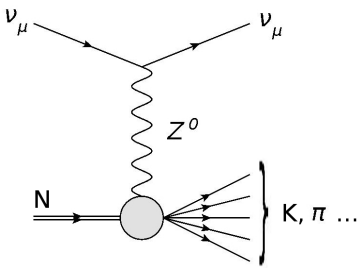

Figure 1.17: Neutral current deep inelastic scattering Feynman diagram.

- The neutral current elastic scattering involves the process $\nu_\mu N \rightarrow \nu_\mu N$, where the nucleon N can be a proton or a neutron.
- The neutral current π^0 production, $\nu_\mu + N \rightarrow \nu_\mu + N + \pi^0$, is one of the main sources of background in the ν_e appearance analysis for experiments searching for the $\nu_\mu \rightarrow \nu_e$ oscillation. This process is also usually described with the RS model.
- The neutral current deep inelastic scattering is illustrated in figure 1.17. It produces, in addition to the neutrino, several hadrons in the final state.

Experimental results for neutral current cross section measurements are usually presented as a ratio to the charged current cross sections. They are also parametrised in this way in the NEUT generator. More details can be found in [36].

Chapter 2

The T2K experiment

2.1 Principle

T2K [42] stands for Tokai to Kamioka. It is a long baseline neutrino oscillation experiment, taking place in Japan. The principle of the experiment is illustrated in figure 2.1. A muonic neutrino beam is produced at J-PARC in Tokai on the east coast of Japan, as described in subsection 2.2. It first goes through a near detector, also situated at J-PARC, which is detailed in subsection 2.3. It then goes through the earth crust to reach the far detector, located at Kamioka 295 km away. The far detector, Super-Kamiokande, is described in subsection 2.4. Finally information on the data taking of the experiment can be found in subsection 2.5.

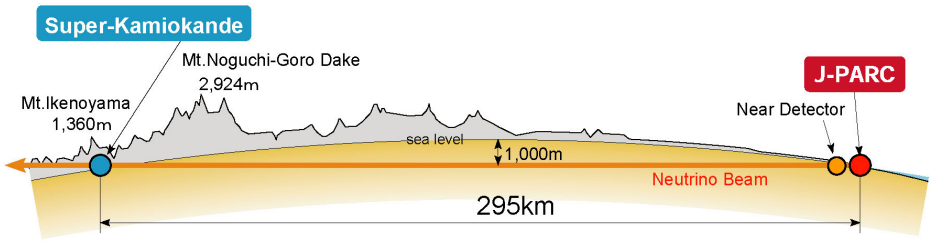

Figure 2.1: Schematic view of the T2K experiment.

The aim of T2K is to study neutrino oscillations. The experiment pursues two main goals:

- observe the appearance of electronic neutrinos in the beam of muonic neutrinos. This allows the measurement of the θ_{13} mixing angle, which was unknown at the start of the experiment.

- study the disappearance muonic neutrinos. This gives a precise measurement of the θ_{23} mixing angle and the Δm^2_{32} square mass difference.

2.2 The neutrino beam

2.2.1 The proton beam

A 30 GeV proton beam is produced on the site of J-PARC (Japan Proton Accelerator Research Complex), using three successive accelerators, shown in figure 2.2. They were built starting in 2004 and commissionned in 2009. The first one is a linear accelerator (Linac) giving the protons an energy of 181 MeV. The energy of the protons is brought up to 3 GeV in the second accelerator, a rapid cycle synchrotron (RCS). The final 30 GeV energy is reached in the third accelerator, the main ring (MR), whose circumference is 1,567 m.

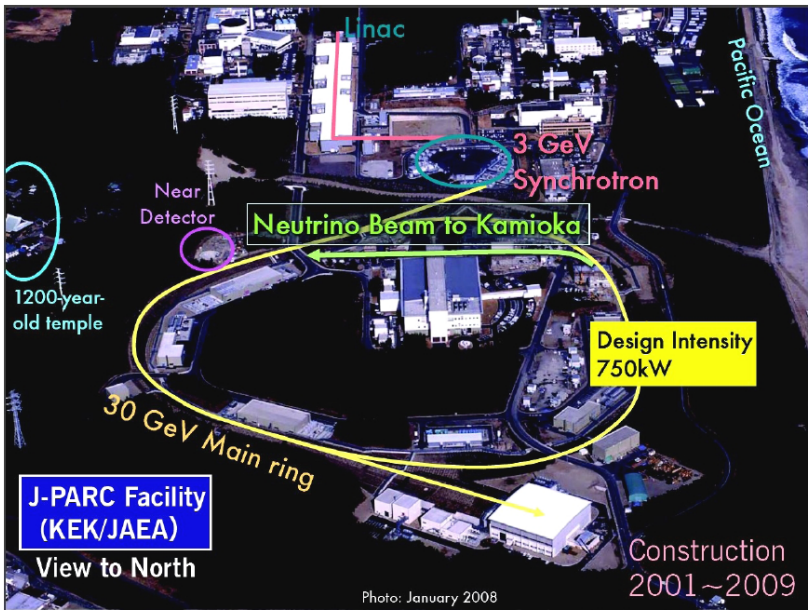

Figure 2.2: The accelerator complex at J-PARC.

The nominal power of the accelerator is 750 kW. So far a power of 200 kW has been reached. The accelerator provides about 10^{14} protons per pulse in eight bunches (only six bunches for the first run until June 2010) with a repetition rate of 0.31 Hz.

2.2.2 Production and focalisation of hadrons

The proton beam is extracted from the main ring by a set of kicker magnets and sent to a graphite target. The 91.4 cm long cylindrical target with a diameter of 2.6 cm corresponds to 1.9 interaction lengths. Graphite was chosen for its high fusion temperature and good thermic properties, as the temperature can reach 700°C at its center during operation, even though it is cooled down with helium. The number of protons on target (POT) is the main unit to measure the accumulated statistics of the experiment.

The path leading from the proton beam to the neutrino beam is illustrated in figure 2.3. Many hadrons are produced in the interactions of protons with the target, mainly pions and also kaons. The decay of these hadrons will later produce neutrinos. While we have no ways to change the direction of neutrinos, charged hadrons can be deviated with magnetic fields. In T2K, the charged hadrons are focused with three successive magnetic horns, powered with an electric current of intensity 250 kA. The polarity of the horn is chosen to focus positively charged hadrons in the direction of the original proton beam and defocus negatively charged hadrons. However inverting the polarity is foreseen in the future in order to do the opposite and consequently produce an antineutrino beam instead of a neutrino beam.

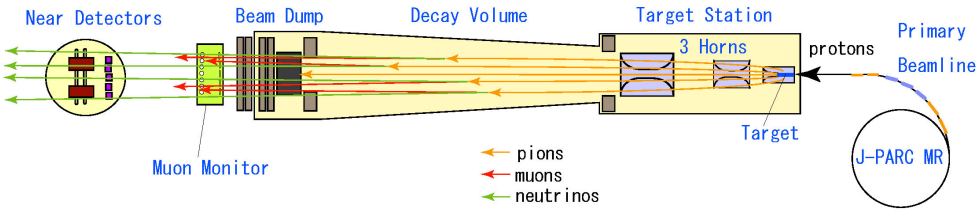

Figure 2.3: Production of the neutrino beam.

In the simulation of the beam used to predict the neutrino flux, proton interactions in the target are simulated with the FLUKA package. To reduce the large systematics uncertainties (up to 30 %) in the hadroproduction model, T2K uses the measurements of the SHINE (NA61) experiment [43]. This experiment uses the proton beam from the SPS at CERN and a graphite target similar to the T2K target. Its spectrometer measures the rates and properties of the charged hadrons produced in the collisions.

2.2.3 Production of neutrinos

Downstream the target and magnetic horns, there is a 96 m long decay tunnel, where the hadrons can decay, producing neutrinos. The positively charged pions decay almost exclusively (in 99.9877 % of the cases) to positively charged muons and muonic neutrinos ($\pi^+ \rightarrow \mu^+\nu_\mu$). The positively charged kaons decay mainly (in 63.55 % of the cases) also to positively charged muons and muonic neutrinos ($K^+ \rightarrow \mu^+\nu_\mu$). A block of graphite with a mass of 75 tons is used as beam dump at the end of the tunnel to stop all particles other than neutrinos. In fact muons with an energy higher than 5 GeV can also go through and they are useful as they are detected in a muon monitor, which is used to check the beam direction within 0.25 mrad and the beam intensity within 3%.

The beam of neutrinos emerging from the beam dump has a wide energy spectrum. However, as the neutrino energy spectrum varies with the angle of the neutrino momentum with respect to the proton beam axis, neutrinos in a rather narrow energy band can be selected by placing the detector off-axis, as illustrated in figure 2.4. The value of the off-axis angle is chosen so that the peak of the energy spectrum corresponds to the value where the neutrino oscillation is maximum, thus improving the sensitivity of the experiment to the parameters governing the oscillation.

The neutrino beam is essentially made of ν_μ, but has also a small fraction of $\bar{\nu}_\mu$, ν_e, and $\bar{\nu}_e$, as shown by the flux prediction in figure 2.5. The ν_μ component, coming from π^+ and K^+ decays as explained above, is enhanced by the off-axis configuration. The $\bar{\nu}_\mu$ component comes mainly from decays of negatively charged

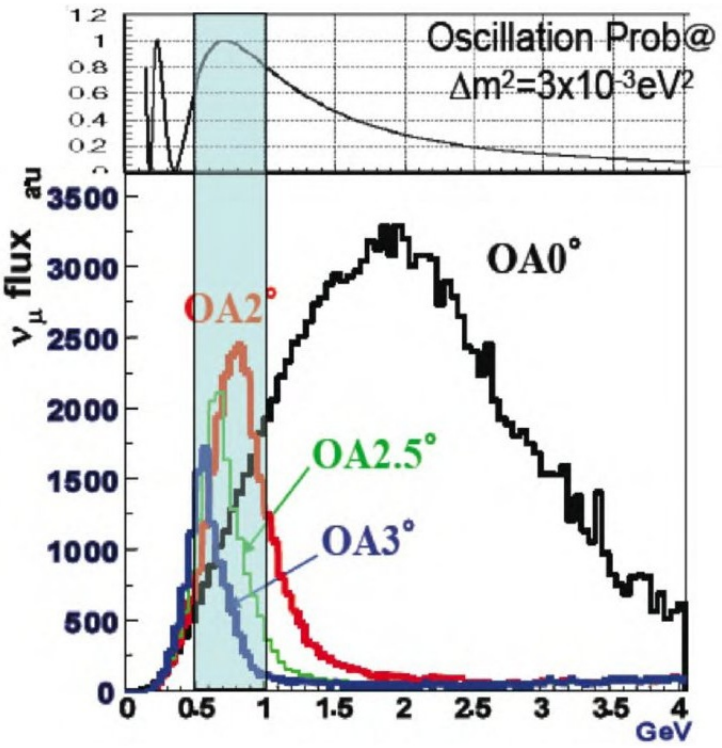

Figure 2.4: Effect of the choice of the off-axis angle on the neutrino energy spectrum. The energy spectrum is shown in black for the on-axis beam, while those for an off-axis angle of 2°, 2.5°, and 3°, are shown in red, green, and blue, respectively. With an off-axis angle of 2.5°, the peak of the energy spectrum is around 600 MeV, at the value where the oscillation probability (see top figure) is maximum.

hadrons, that reach the decay tunnel, such as $\pi^- \to \mu^- \bar{\nu}_\mu$, and also from anti-muon decays: $\mu^+ \to e^+ \nu_e \bar{\nu}_\mu$. The ν_e component comes from these same decays of μ^+ and also from three-body kaon deacays: $K^+ \to \pi^0 e^+ \nu_e$. It is an intrinsic background for the ν_e appearance analysis. The $\bar{\nu}_e$ component, due to the same processes as for ν_e, but with opposite charge, is tiny.

Note that the off-axis configuration also reduces the fraction of ν_e from three-body decays. This reduction of one of the main background for the ν_e appearance analysis is another advantage of the off-axis configuration.

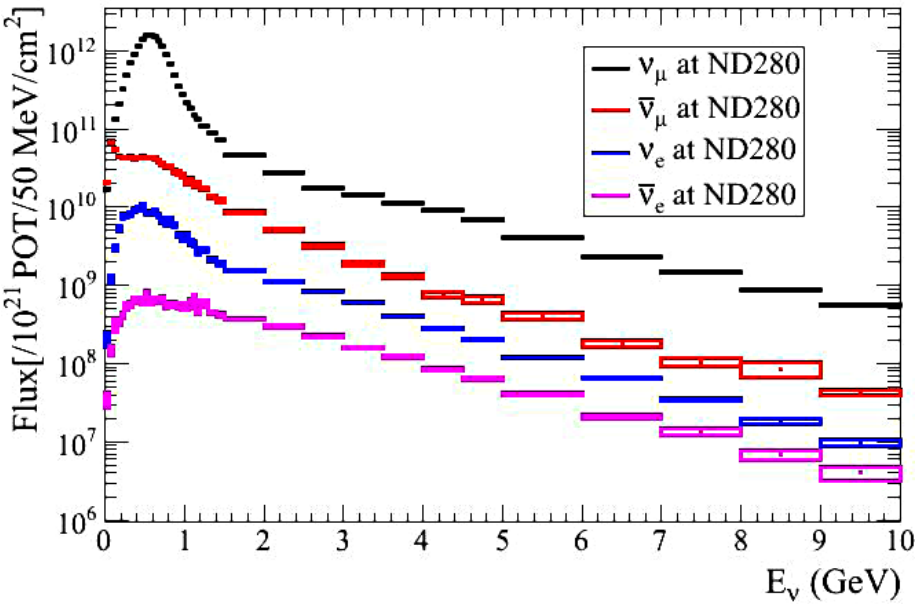

Figure 2.5: Neutrino flux to the near detector as a function of neutrino energy for the various species: ν_μ (in black), $\bar{\nu}_\mu$ (in red), ν_e (in blue), and $\bar{\nu}_e$ (in pink).

2.3 The near detector

The near detector is located in J-PARC, 280 m downstream of the target. It has two parts: an on-axis detector, INGRID, and an off-axis detector, ND280. Both are located in a 37 m deep pit with a diameter of 19 m, INGRID being below ND280. Both near detectors were commissioned in 2009.

2.3.1 INGRID

The INGRID (Interactive Neutrino GRID) on-axis detector [44] measures the direction and intensity of the neutrino beam. It is made of 16 identical modules, as shown in figure 2.6. Seven modules are in a vertical arm, about 10 m long. Seven modules are in an horizontal arm with the same length. These two arms are arranged as a cross, whose center corresponds to the center of the neutrino beam. Finally two modules are outside the cross to check for asymmetries.

Each module is made out of nine iron planes, providing a total mass of 7.1 tons as target for the neutrino interactions, sandwiched with eleven tracking planes

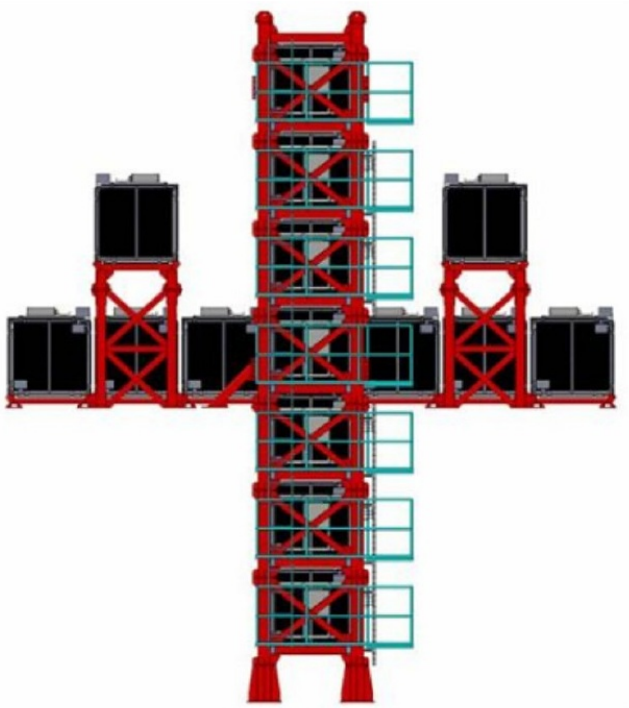

Figure 2.6: View of the INGRID detector.

(there is no iron plane between the last two tracking planes), consisting of one layer of 24 horizontal scintillator bars and one layer of 24 vertical scintillator bars.

INGRID detects several thousands neutrino interactions per day. It allows the measurement of the position of the beam center within 10 cm in both transverse directions, corresponding to an angular precision of 0.4 mrad.

2.3.2 ND280

The goal of ND280 (near detector 280 m from the target) is to characterise the neutrino beam going to the far detector before oscillation: its initial composition, its flux, and its energy spectrum. It has also the aim to measure various cross sections of neutrino interactions. The measurement of the charged current deep inelastic scattering cross section performed in this thesis belongs to this programme.

ND280 is set with an off-axis angle of $(2.515 \pm 0.04)^\circ$ with respect to the neutrino beam direction, defined as the primary proton beam direction. As illustrated in figure 2.7, ND280 consists of a π^0 detector (P0D), a tracker made with two fine grain detectors (FGD) and three time projection chambers (TPC), and several electromagnetic calorimeters (ECAL): the downstream ECAL along the beam line, the P0D ECAL surrounding the P0D, and the barrel ECAL surrounding the tracker. All these detectors are inside a magnet yoke, containing a set of side muon range detectors (SMRD), which completes the detector. All these parts are described briefly below, while the TPC will be described in detail in the next chapter.

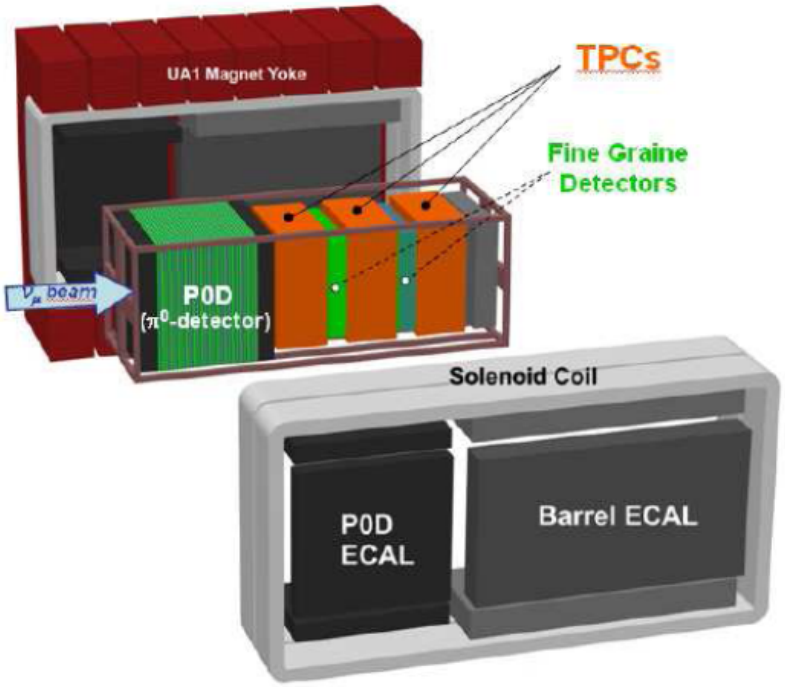

Figure 2.7: Schematic view of the ND280 offaxis detector.

The magnet was initially used by the UA1 experiment at CERN. The coils, made out of aluminium, carry an electric current of 2,900 A in order to create a uniform magnetic field of 0.2 T, transversely to the neutrino beam line. This

magnetic field allows the determination of the momentum of charged particles through the measurement of the curvature of their trajectories. The magnet is made of two parts, that can be separated in order to give access to the detectors inside, as illustrated in figure 2.8. This is usually done during shutdown periods.

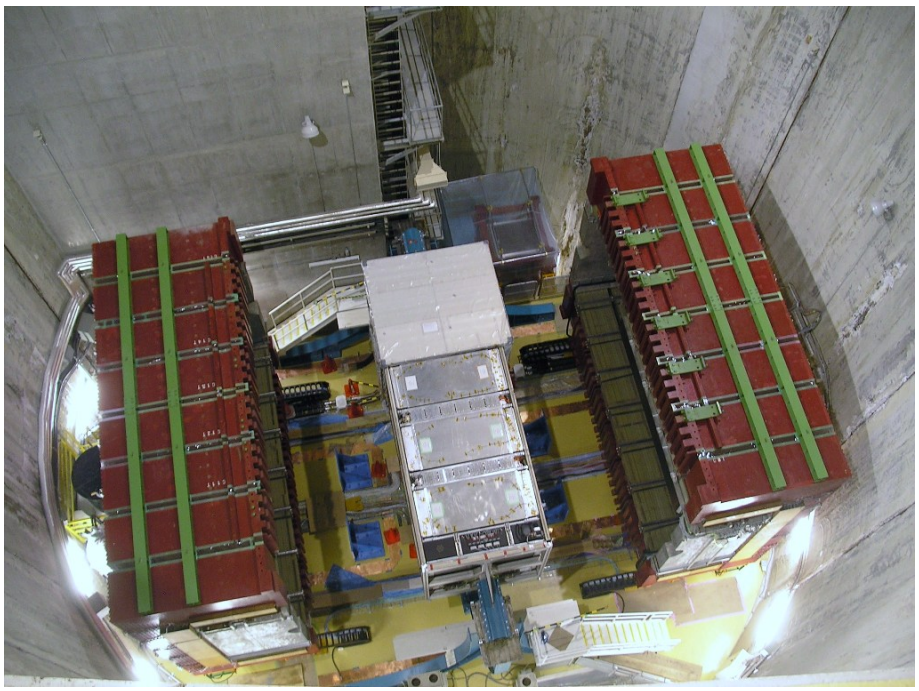

Figure 2.8: Picture from the top of the pit of the ND280 detector, with the magnet open.

Upstream along the neutrino beam direction inside the magnet is the P0D [45], to study neutrino interactions producing neutral pions, in particular neutral currents $\nu_\mu\, n \rightarrow \nu_\mu\, n\, \pi^0(X)$. It consists of 76 planes of horizontal or vertical scintillator bars, sandwiched in lead or brass sheets and bags filled with water, giving a total target mass of 17.6 tons.

The FGD is the active target of the tracker [46]. Its goal is to reconstruct the vertex of the neutrino interactions. It is composed of two detectors, FGD1 between the first two TPCs, and FGD2 between the last two TPCs, with a mass of 1.1 tons each. While FGD1 is made of 30 planes of 192 scintillator bars, alternatively horizontal and vertical, FGD2 has six passive water planes and seven

double planes (one horizontal and one vertical) of scintillator bars, as illustrated schematically in figure 2.9. The comparison of the neutrino interaction rates in the two FGDs should measure the neutrino cross-section in water (as in the far detector) compared to the neutrino cross-section in scintillator. Each scintillator bar has a length of 1864 mm and a section of 9.6×9.6 mm^2. The efficiency of the scintillator bars, measured on cosmic muons, is higher than 99 %.

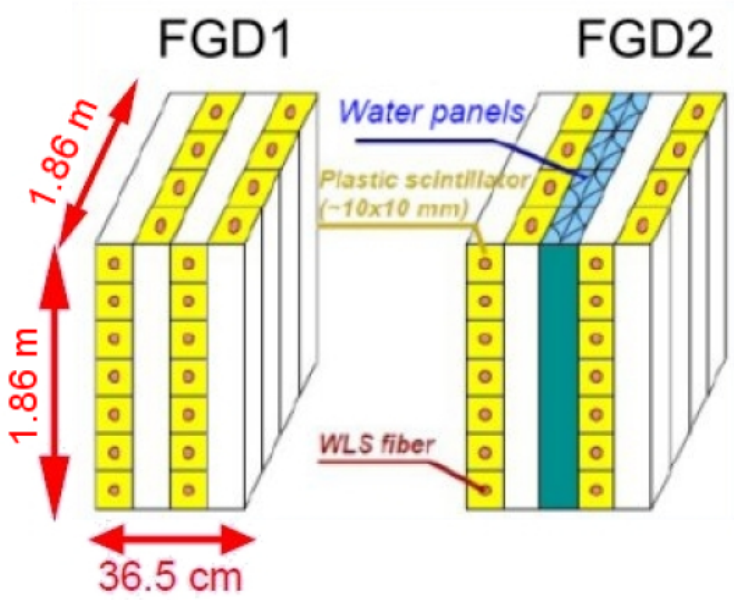

Figure 2.9: Schematic view of the two FGDs.

The ECAL [47] consists of 13 modules in total, to be as hermetic as possible: six modules around the P0D (P0D ECAL), six modules around the tracker (barrel ECAL), and one module downstream the tracker (downstream ECAL). It is made of plastic scintillator bars interleaved with lead absorber sheets.

The SMRD [48] consists of 440 scintillator modules placed in the gaps within the magnet yoke. Its main goal is to detect muons either escaping the detector or entering the detector from the side, and measure their momentum.

For all the detectors based on plastic scintillator bars, i.e. INGRID, P0D, FGD, ECAL, and SMRD, the scintillation light is collected at the end of each bar by a wavelength shifting fiber. The other end of the fiber is connected to a readout device: a multi-pixel photon counter, whose electronics is based on the

Trip-T ASIC. This counter was developed for T2K and over 50,000 such counters were produced for the experiment.

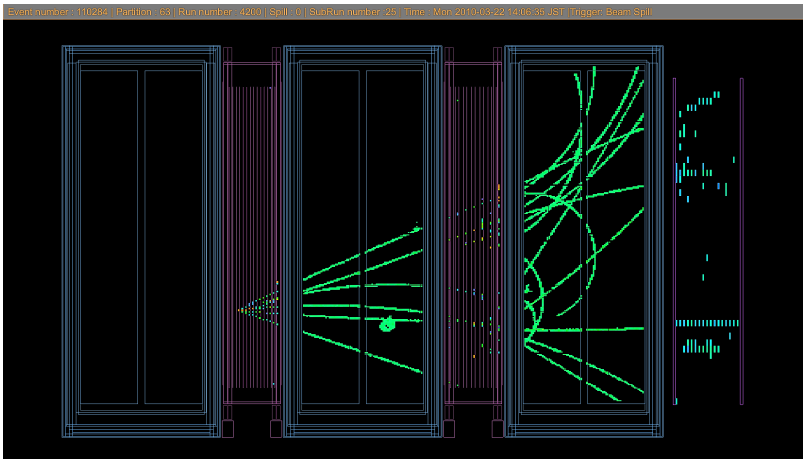

Figure 2.10: An event display in the tracker of the ND280 offaxis detector. The event with a lot of tracks is probably a DIS event.

Figure 2.10 displays an event recorded by ND280: it is a neutrino interaction in FGD1, giving tracks in TPC2 and TPC3 and hits in FGD2 and downstream ECAL.

2.4 The far detector

The far detector is the Super-Kamiokande (SK) detector [49], commissionned first in 1996. It has been used to study atmospheric and solar neutrinos, as mentioned in chapter 1. It was upgraded several times and its current phase, SK-IV, started in 2008. It is situated 295 km away from J-PARC at Kamioka, with exactly the same off-axis angle as ND280. SK is under 1 km of rock (2.7 km of water equivalent). Thus the cosmic ray flux is reduced by a factor 10^5 compared to what it is on surface.

Super-Kamiokande shown in figure 2.11 is a huge water Cherenkov detector, the largest detector of this type in the world. It is a cylinder of 39.3 m height and 41.4 m diameter, whose wall is made out of steel. It is filled with 50 kt of purifed water. The detector has two parts:

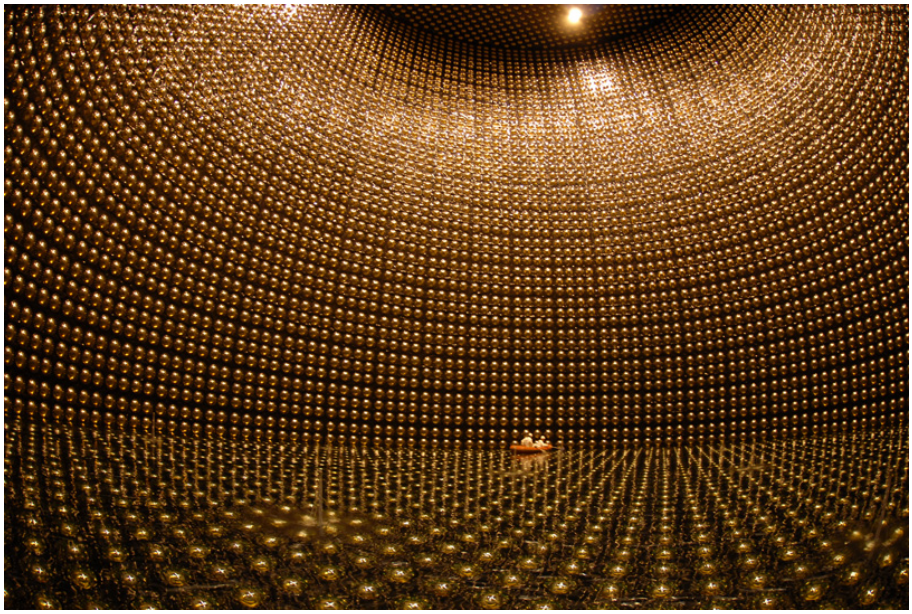

Figure 2.11: View from the inside of the Super-Kamiokande detector, half-filled with water, and its photomultipliers.

- the inner detector (ID), 36.2 m in height and 33.8 m in diameter. The Cherenkov light is detected by 11,146 photomultipliers tubes, 20 inches in diameter, looking inwards.
- the outer detector (OD), surrounding the ID. It is equipped with 185 photomultipliers tubes, 8 inches in diameter, looking outwards. It is used to reduce backgrounds, such as cosmic muons or radioactivity in the neighbouring rocks.

When crossing the water, relativistic charged particles, with a velocity higher than the velocity of light in water, emit photons, the so-called Cerenkov light [50], along a cone whose opening angle is characteristic of the charged particle velocity. Furthermore, the Cerenkov ring created by an electron, with blurry edges because of the electron scattering in water, can be distinguished from the ring created by a muon, which has neat edges. Consequently a water Cerenkov detector is well suited to recognise electronic neutrino interactions, producing an electron, from muonic neutrino interactions, producing a muon.

2.5 Data taking

ND280 was commissioned in December 2009. The first physics run started in January 2010 and was completed in June 2010. The second physics run, started in October 2010, was stopped by the dramatic earthquake in Japan on March 11, 2011. After less than one year off to recover from the earthquake, J-PARC was able to restart the beam. The third physics run lasted from February 2012 to June 2012. Finally a fourth physics run was taken from October 2012 to May 2013. These data taking periods are illustrated in figure 2.12. The team working on the beam managed to increase the number of protons per pulse for each physics run.

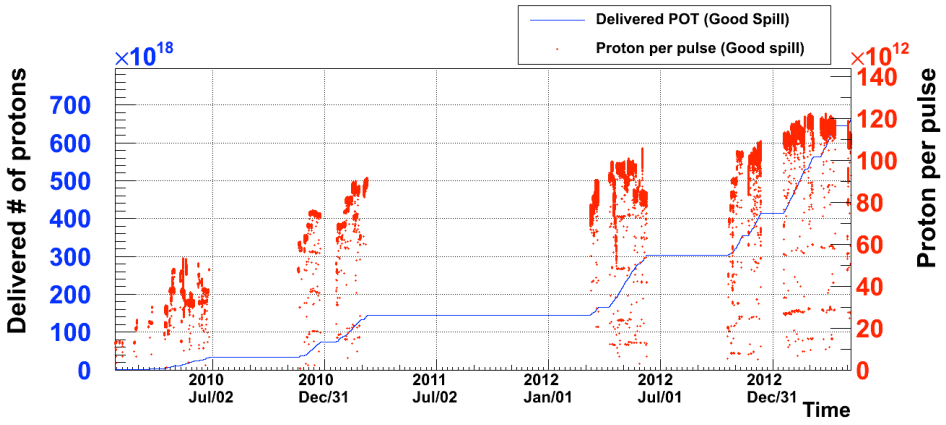

Figure 2.12: T2K data taking. The blue curve gives the cumulative number of delivered protons on target, while the number of protons per pulse is shown in red.

In total, T2K has accumulated 6.4×10^{20} POT until May 2013, which provide the data sample used in this thesis. This is less than 10 % of the total statistics (7.8×10^{21} POT) foreseen at the end of the experiment near the end of the decade. Data taking has restarted in May 2014.

Chapter 3

The TPC

In this chapter, we first introduce the basic concepts of gaseous detectors in section 3.1, time projection chambers in section 3.2, and MicroMegas detectors in section 3.3. Then the TPC of T2K is described in section 3.4. Its calibration is seen in section 3.5 and its main performances are given in section 3.6.

3.1 Principles of gaseous detectors

When a charged particle crosses a gaseous detector, it initiates a process in the gas volume with different steps starting from the primary ionisation of the gas molecules, then the drift and the multiplication of the primary electrons, and finally the detection of the amplified signal.

Primary ionisation

Crossing the gas volume, a relativistic charged particle loses energy. This energy loss is the result of exchanging virtual photons between the charged particle and the electrons from the molecules of the gas. Depending on the scale of the gas ionisation potential, these photons excite the molecule or ionise the molecule, with the emission of an electron. The emitted electron issued from the primary ionisation may excite or ionise other molecules producing secondary electrons. Along the trajectory of the track a certain number of electrons are produced.

Motion of the charge carriers in the gas: Drift

The electrons and ions created during the ionisation process drift through the gas volume due to the presence of electric and magnetic fields. The average motion depends on the orientation of the electric and magnetic fields. The drift speed depends on the magnitude of the electric field, it is unaffected by the magnetic field if it is oriented parallel to the electric field. To minimise the sensitivity of the drift velocity to field inhomogeneities, the drift chambers are operated at the electric field where the maximum of the electron drift velocity is reached. While drifting, the behavior of electrons and ions is different. In contrast with the randomly distributed direction of the electrons after a scattering with the gas molecules, the ions experience smaller changes in their direction. In addition, being much heavier than the electrons, the ions lose most of their energy in collisions. Because of the limited mobility of the ions, these are the electrons which are collected and detected in the detector.

Electrons issued from the gas ionisation can be captured by the gas molecules. The loss of primary electrons will degrade the performance of the detector and should be avoided. The probability of the attachment process is related to the electron affinity of the gas. For that reason, the gaseous detectors use the noble gases which have a low electron affinity. But if gas impurities such as oxygen are present in the gas, the electron affinity will increase.

Amplification

An electron accelerated by an electric field of a few 10^4 V/cm can start an avalanche. The gain coefficient which is referred as the amplification factor is a function of the electric field and of the gas type and density. The gaseous detectors are usually operated in the proportional mode. This means that the signal produced is proportional to the number of primary electrons.

3.2 The Time Projection Chamber

The Time Projection Chamber (TPC) is a gaseous detector for tracking the charged particles. The concept of the TPC was invented in the late 1970's by David Nygren [51]. It is based on the principle of determining the three dimensional track positions, by measuring the time of drift of the primary electrons along the field directions, as shown in figure 3.1.

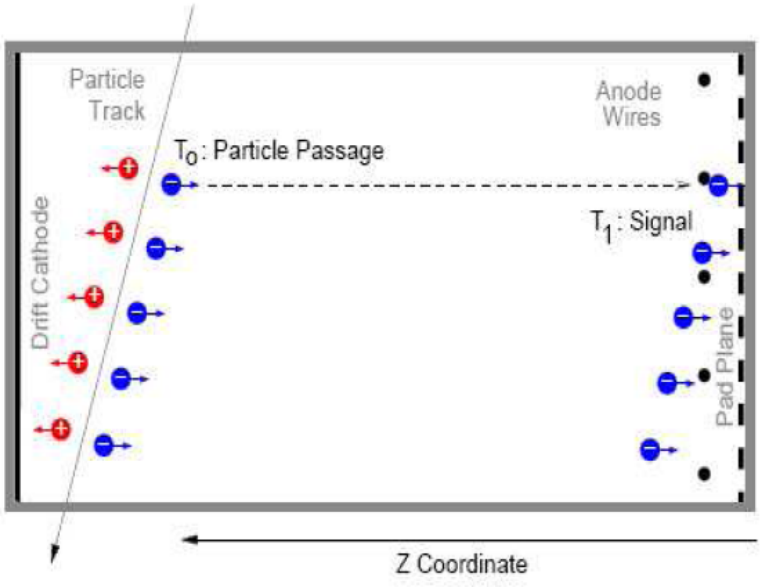

Figure 3.1: Working principle of a TPC. The charge detected on the segmented anode gives a 2D projection of the particle track. Combined with a measurement of the drift time, the track can be reconstructed in all three dimensions.

When passing through the active volume of a TPC, which is generally made up of a cylindrical or parallelepipedic gas volume, with an homogeneous electric drift field applied between the endplates, a charged particle creates primary ionisation. The produced ions drift to the cathode and the electrons drift to the anode. Before reaching the anode the electrons have to be amplified to produce a detectable signal: this is obtained using wires in a Multi-Wire Proportional Chamber (MWPC) or an amplification region in Micro-Pattern Gaseous Detector (MPGD) to detect the drift electrons providing a two dimensional projection

of the track on the readout plane (transverse to the drift direction). The third coordinate of the hits is determined from the arrival time of the signals on the readout plane. It is reconstructed as a function of the drifting time which requires knowing well the drift velocity which is constant for a uniform field in the drift region and the time T0 at which the particle crossed the detector. The T0 is generally provided by an external trigger, such as a scintillator based detector which has a fast response time.

In TPCs operated with MPWC amplification, the thin wires enable electrons to multiply. The ions produced together with the electrons near the wire drift back towards the cathode, distorting the electric field. A solution to avoid this problem is to use Micro-Pattern Gaseous Detectors. These readout systems are wireless and consist in a device where a high electric field is applied in a region with a width of the order of 100 μm, producing the multiplication of the electrons.

On the segmented readout plane, the measurement of track points is realised not only by weighting the deposited charge on the pads but also by a careful choice of the pad pitch which allows a precise measurement of the avalanche average position. The resolution in the drift direction depends mainly on the longitudinal diffusion in the gas.

The TPCs cover large volumes thus providing a large number of measurements along the track. The TPCs introduce little material along the particle trajectories thus keep minimum scattering and give the possibility to measure other characteristics of the event in outer detectors.

Measurement of the momentum

A TPC is intended to measure the momentum of charged particles. For this reason it is placed within a uniform magnetic field. The trajectory of the charged particle is a helix. For a magnetic field which is parallel to the direction of the electric field (reducing in this way the electron transverse diffusion coefficient by large factors), and thus orthogonal to the readout plane, the projection of the track on the readout plane is an arc of a circle of radius

$$R = p_t/eB \tag{3.1}$$

where $p_t = (p_x^2 + p_y^2)^{1/2}$ is the particle transverse momentum. The transverse momentum of the charged particle can be obtained through the simple equation

$$p_t = 0.3 \times B \times R \tag{3.2}$$

where the transverse momentum p_t is in GeV/c, the magnetic field B in Tesla and the radius of curvature R in meters. The 0.3 factor is a unit conversion term. The total momentum p is then given by

$$p = p_t / \sin\phi \tag{3.3}$$

where ϕ is the angle between the track and the direction of the magnetic field.

3.3 The Micro-Mesh Gaseous Detector

The Micro-Mesh Gaseous Detector also called the MicroMegas (MM) is a Micro-Pattern Gaseous Detector used for the T2K TPCs. It will be described here. This Micro-Pattern Gaseous Detector is fabricated by means of printed-circuit-boards (PCB) techniques. The MicroMegas principle is shown in figure 3.2. A micro-mesh divides the gas volume into two regions: a conversion and drift region, and an amplification stage with an inter-electrode distance of the order of 100 μm.

When a charged particle crosses the TPC volume, in the drift region, the electrons produced by the gas ionisation drift towards the MicroMegas mesh, which plays the role of the anode with respect to the central cathode. In the conversion stage, the thin woven mesh plays the role of the cathode, and the anode can be segmented into strips or pads.

In the amplification region, a very high field (20 to 70 kV/cm) is created by applying voltages of few hundred volts between the mesh (cathode) and the anode plane. In T2K's case the electric field in the gap between the mesh and the pads is typically 25 kV/cm. If the field ratio between the drift and the amplification regions is large enough and the mesh thin enough, the ionisation electrons are multiplied in an avalanche, and collected by the anode with an electron collection efficiency close to 100 %. The ions produced by the gas ionisation are collected

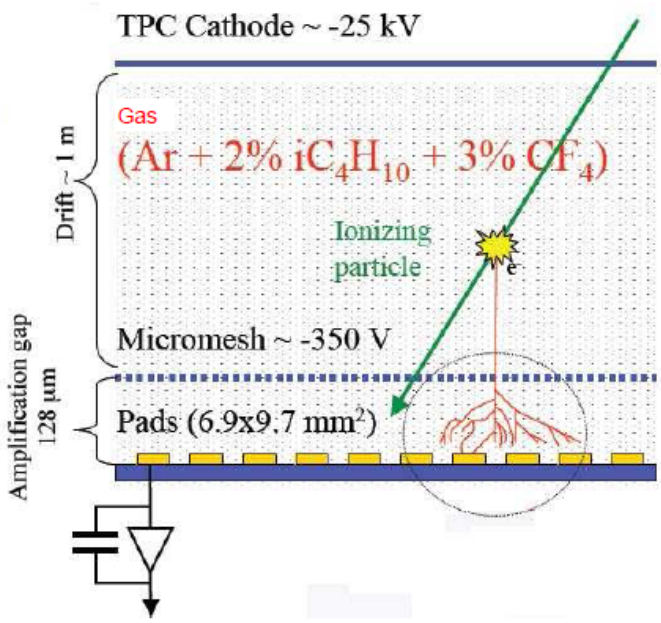

Figure 3.2: Schematic view of the MicroMegas detector used in T2K. The ionisation electrons drift towards the micro-mesh that is placed 128 μm above the anode. The micro-mesh is supported by short cylindrical pillars. Between the mesh and the anode, segmented to form pads, an avalanche is produced.

by the mesh. These two signals, the electron signal and the ion signal which is delayed with respect to the electron one, allow the detection of the charged particles. The typical signal shape can be observed in figure 3.3.

The grid has a hole pitch of 20 - 50 μm and is maintained above the anode plane by means of insulating pillars. The smallness of the gap leads to an avalanche with small size, therefore the signal rise time is short. In absence of longitudinal diffusion this would lead to an electron signal of a few nanoseconds and an ion signal usually less than 50-100 ns. This detector type is characterised by its uniform gain on all of its active surface, guaranteed by the uniformity of the amplification gap.

To produce the MicroMegas modules, used in T2K TPCs, a new production method, called bulk MicroMegas, developed by a CERN-Saclay collaboration [52], is used. In this case, both the mesh and the pads are kept together by a thin

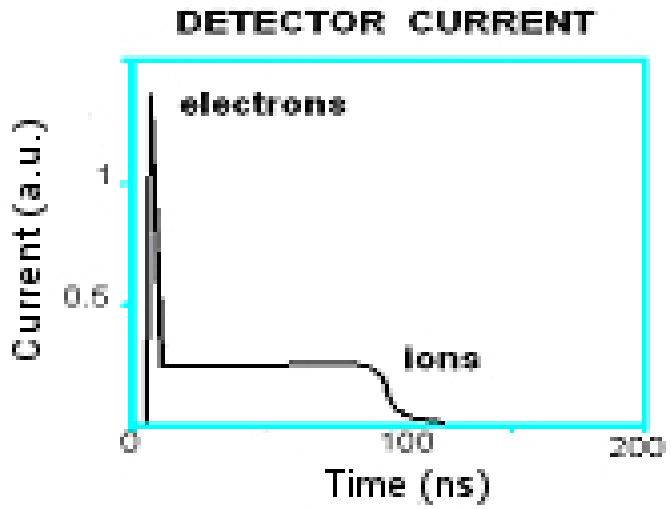

Figure 3.3: The typical signal shape of the electrons and ions.

photo-imaged layer forming one unique robust structure. This robustness is one of the main advantages of this type of MPGD, since it allows the instrumentation of large areas made in one piece, with minimal dead zones in between the modules. Moreover, the technique used to produce them is suited for industrialisation and mass production, thereby being a cheap alternative to wire chambers, with advantages with respect to the latter such as the uniform electric field mentioned above and its robustness.

3.4 The T2K TPCs

Three identical TPCs [53] are installed in the ND280 facility, the first one is downstream the P0D, the second one is between the two FGDs and the third one is between the second FGD and the Ecal. In figure 3.4, a view of the main components of the TPC is shown.

The outer dimensions of each TPC are 0.9 m along the beam direction and 2.5 m $\times$ 2.5 m in the plane perpendicular to the neutrino beam. The TPC is composed of two boxes. The inner box forms the field cage and the drift volume.

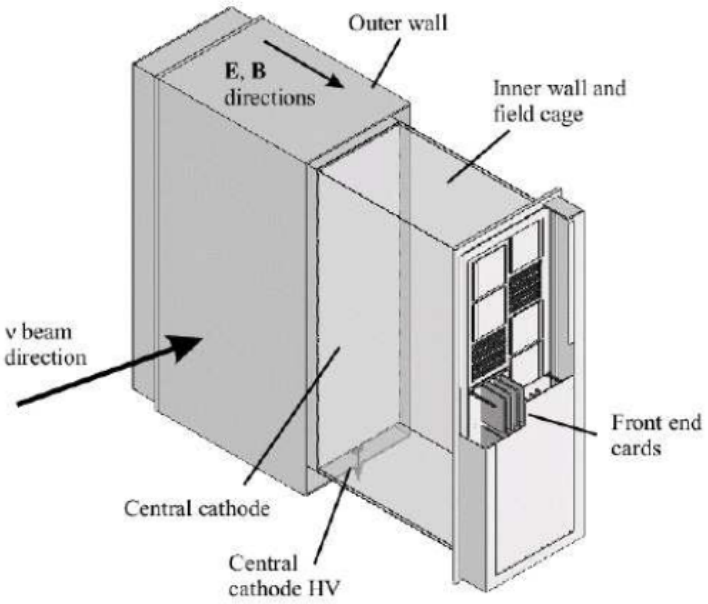

Figure 3.4: Schematic view of the T2K TPC detector.

The outer box, surrounding the inner box, forms a CO_2 volume that provides electrical insulation. The TPC works at atmospheric pressure.

In table 3.1, a summary of the TPC characteristics is shown. The meaning of the different parameters will be made clear in the following of this chapter.

3.4.1 The TPC physics goals: requirements

The Time Projection Chambers serve three main purposes.

- Their first goal is to measure the momentum of the charged particles that cross the TPCs volume, through the measurement of the track's curvature induced by the 0.2 T magnetic field produced by the surrounding magnet. A transverse momentum resolution of 10 % at 1 GeV is recommended. Given the low operating magnetic field this will require good space point resolution, that is obtained using a segmented readout plane. The TPCs provide a space point resolution of about 0.7 mm. The momentum measurement

Outer dimension	$2.5 \times 2.5 \times 1\text{m}^3$
Maximum drift distance	90 cm
Gas mixture	$Ar : CF_4 : iC_4H_{10}(95 : 3 : 2)$
Cathode high voltage	-25 kV $\rightarrow E \sim 280$ V/m
Drift speed	7.9 cm/μs
Tranverse diffusion coefficient	$237\mu\text{m}/\sqrt{\text{cm}}$
Total number of readout channels	124272
Pad dimensions	$6.9 \times 9.7\text{mm}^2$
MicroMegas high voltage	-350 V $\rightarrow E \sim 27$ kV/m
MicroMegas gain	~ 1500 (at 350 V)
ASIC sampling time	40 ns
ASIC peaking time	200 ns

Table 3.1: TPC parameters in the default running conditions with a magnetic field of 0.2 T.

is needed for the determination of the neutrino energy, crucial both in the neutrino oscillation analysis and in the neutrino cross section measurement.

- The second goal, required to reach T2K physics goals on the atmospheric parameters measurements, is to know the absolute momentum scale at the level of 2 %. This goal can be met by controlling the electric field distortions, mapping the magnetic field and using an absolute momentum calibration physical signal (for example the invariant mass of the K^0 produced by neutrino interactions [36]).

- Lastly, the TPCs can perform particle identification using the energy deposited (dE/dx) by each particle. It is crucial to distinguish muons from electrons and protons from pions. This allows the measurement of the beam ν_e intrinsic contamination, which needs to be known as precisely as possible to reduce the uncertainties on the search for ν_e appearance at the far detector. The resolution on the measurement of the deposited energy, which is based on a truncated mean method, must be better than 10 %.

3.4.2 The mechanical structure

The TPCs have a double box design to allow better isolation and field homogeneity. The inner walls of the inner box are covered with copper strips to form the field cage, which, together with the central cathode that divides the TPC in two identical drift volumes, produce the required uniform electric drift field. The strip width is 10 mm with a 1.5 mm gap between the strips. The strips are connected to a resistor chain ($R = 20M\Omega$) electrically connected to the central cathode to provide the uniform electric field inside the inner volume. The drift field currently used is about 200 V/cm.

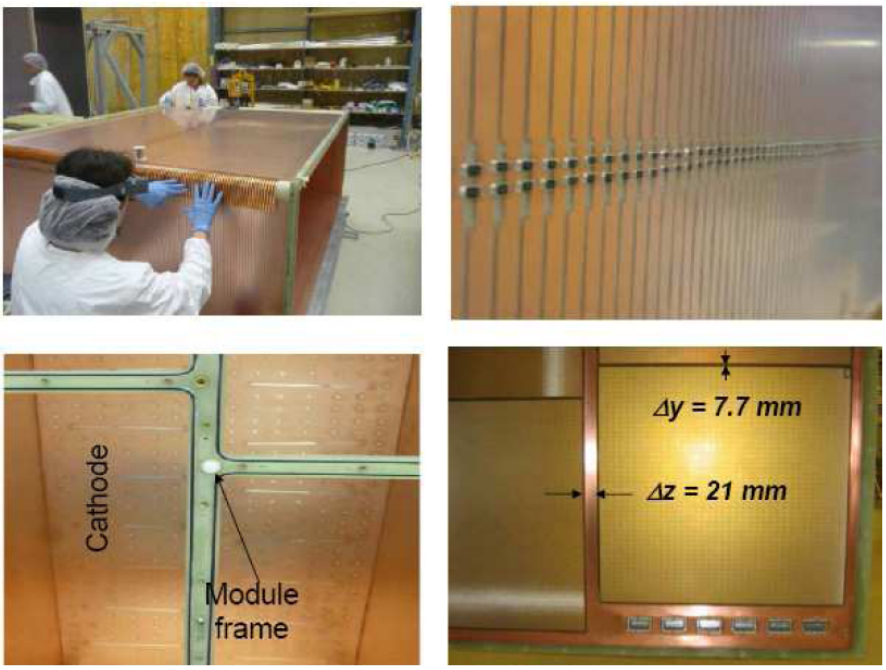

Figure 3.5: Assembly of the first TPC. The inner box is shown (upper left) with its field cage strips used to provide the electric field (upper right). The cathode is seen from the endplate (bottom left) and of one the MicroMegas modules installed on the endplate is shown (bottom right).

The outer box, whose walls are at ground potential, contains CO_2 which is used as an insulating gas. The outer box consists of four walls and two endplates. In figure 3.5 some pictures of the first T2K TPC, taken at the time of the con-

struction, are shown. In these pictures it is possible to see the different parts of the TPC.

3.4.3 Gas System

The gas is chosen to obtain the best possible determination of the momentum and energy loss of charged particles in the TPC. For these purposes the important parameters are the transverse diffusion coefficient (which affects the momentum resolution) and the achievable gain. Other conditions are set by cost and safety issues and by the requirement of a mixture as stable as possible against contaminations, mixing inaccuracies and density changes. The mixture chosen for the TPC inner box is a mixture of Argon, CF_4 and iC_4H_{10} (95:3:2).

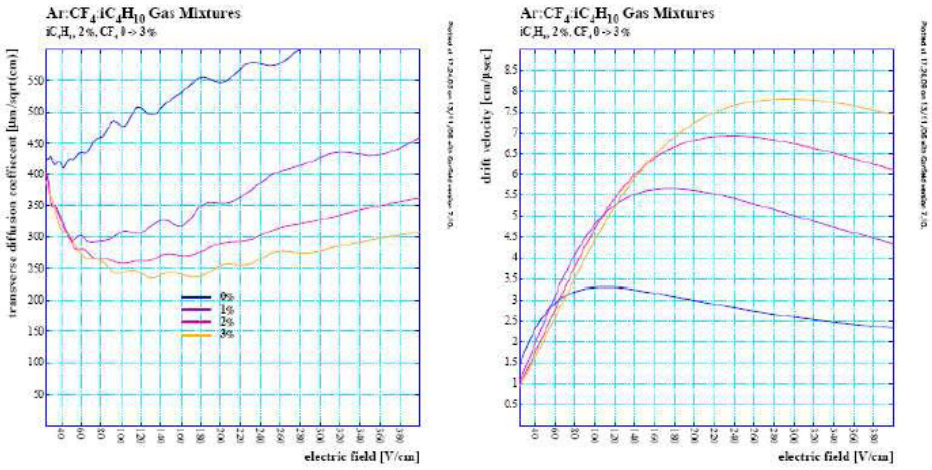

Figure 3.6: Expected transverse diffusion coefficient (left) and drift velocity (right) as function of the applied drift field for fractions of CF_4 between 0 % (blue) and 3 % (yellow) according to the Magboltz simulation. The iC_4H_{10} is kept constant at 2 %.

For an electric field of 290 V/cm (corresponding to the maximum of the drift velocity) and a magnetic field of 0.2 T, this gas has a small expected transverse diffusion coefficient, 237 $\mu m/\sqrt{cm}$, small e^- attachment, high gain, good point resolution and good performance with Micromegas detectors. In figure 3.6 the

expected transverse diffusion coefficient and drift velocity for the Ar : CF_4 : iC_4H_{10} mixture, as a function of the electric field are shown. These plots are obtained using the Magboltz simulation program.

The Argon molecules are the main target for the ionisation, the CF_4 is important to increase the drift velocity in the drift region and the iC_4H_{10} is used as a quencher to absorb the photons, mainly emitted in the amplification region, that, if not absorbed, can start other avalanches, bringing the MicroMegas out of the proportional region. An important task for the gas system is to maintain the oxygen contamination in the inner volume at the level of 10 ppm. In fact a larger contamination would cause the phenomenon of attachment in the TPC gas and consequently a dependence of the signal on the drift distance. To keep under control the oxygen contamination one gas volume is changed every six hours. In addition, the inner volume is kept at a small overpressure of 4.5 mbar. The region between the inner and the outer box is filled with CO_2: this gas has been chosen for its good dielectric rigidity necessary because the inner box in the center of the TPC is at a potential of 25 kV while the outer box is at ground.

3.4.4 The MicroMegas modules

One T2K TPC is instrumented with 24 bulk MicroMegas modules, 12 on each readout plane, disposed in two columns of six modules each, as illustrated in figure 3.7. The dead zone between two modules of the same column is 7.7 mm. To prevent as much as possible horizontal tracks to entirely cross the dead zone between two modules, the two columns are misaligned one with respect to the other by 5 cm. Each module is divided into 48 rows and 36 columns. There are 1726 active pads and 2 pads located in one corner used for the mesh high voltage delivery, with a pad pitch of $7.0 \times 9.8\,mm^2$ for a total active area of $\sim 3m^2$ for each TPC. The total number of channels for the 3 TPCs is of the order of 124,000. The total thickness of a bulk MicroMegas module, shown in figure 3.8, is 19.5 mm.

A high average gain of 1600 is obtained at the operating high voltage of -350 V. At this voltage, the measured number of sparks, electric discharges between the mesh and the pads, is 0.1 spark per module per hour. This low rate explains that the detectors are operated with low-noise electronics and are stable.

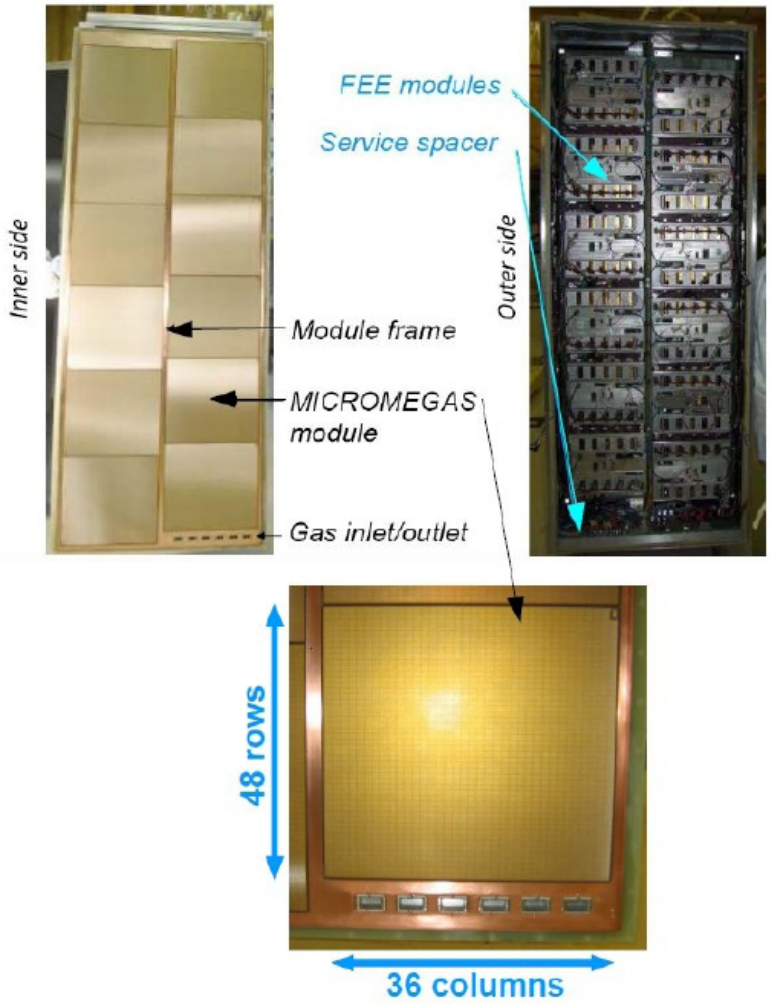

Figure 3.7: A TPC readout plane. The inner side which shows the 12 MicroMegas modules can be seen in the top left picture. The top right picture shows the mounted front-end electronics. The bottom picture shows a zoom on a MicroMegas module.

One advantage of the T2K MicroMegas modules is that they are completely independent and they can be mounted and dismounted from the outside of the TPC field cage, without any internal connections. In case of failure, this makes the detector replacement easier, and prevent as much as possible dust from entering the field cage.

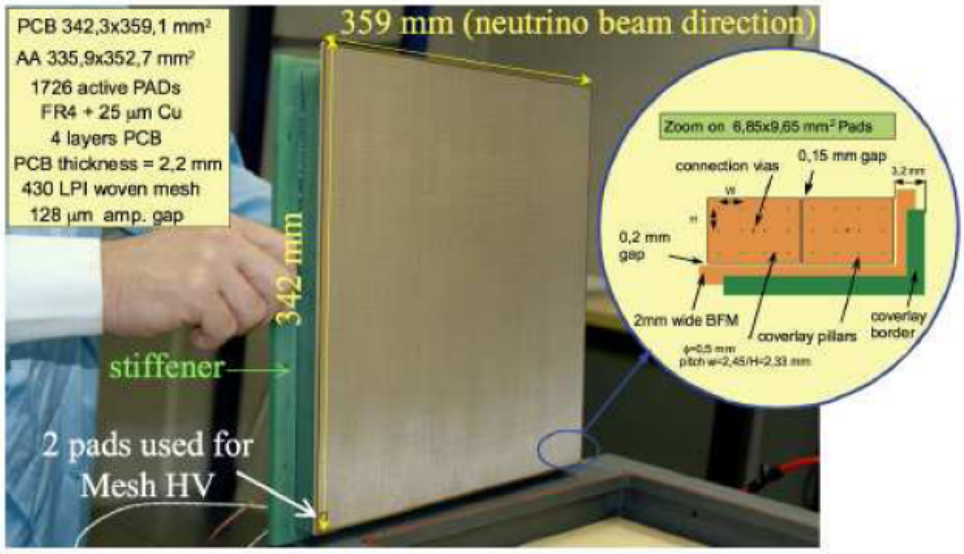

Figure 3.8: A 34 × 36 cm^2 T2K bulk MicroMegas module glued on the stiffener. In the zoom we can see two pads on the corner of the detector with the relative structures.

3.4.5 The Front-End electronic

The requirement for the TPC electronic system is to be able to record all the beam events. The nominal T2K event rate is 0.3 Hz (corresponding to the frequency of extraction of the protons from the JPARC Main Ring) and the electronics is designed to read at a rate up to 20 Hz, providing a comfortable bandwidth to record cosmic rays triggers, pedestals and laser calibration events. The readout consists of two main parts: on-detector electronics, directly mounted on the MicroMegas module and off-detector electronics, housed in a standard rack. Each of the 72 Micromegas modules is readout by six Front-End Cards (FECs) and one Front-End Mezzanine (FEM) card as shown in figure 3.9. Each FEC reads out an area of 48 × 6 pads (288 channels). On each FEC four custom-made front-end ASIC AFTER (Asic For Tpc Electronic Readout) chips are mounted. The AFTER ASIC, developed at Saclay, reads out an area of 12 × 6 pads (72 channels). The AFTER ASICs are characterised mainly by their low electronic noise (600 e^-). Their features include a sampling frequency that can go up to 50

MHz, adjustable gain, and a programmable peaking time.

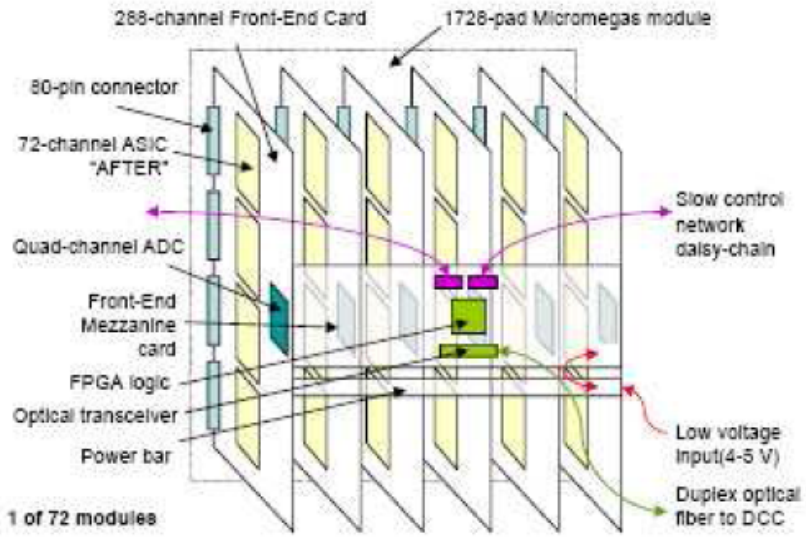

Figure 3.9: Scheme of the readout architecture of a detector module.

A front-end mezzanine card gathers the information collected by the FECs. The FEM communicates via an optical link with the off-detector Data Concentrator Card (DCCs). Each DCC communicates with four MicroMegas modules (three DCCs to readout one endplate) and a total of 18 DCCs are used in the T2K TPCs.

AFTER ASIC chips

The purpose of this device is to shape and sample the signals coming from the MicroMegas pads. The large drift length of the TPC requires an accurate method to obtain the coordinate informations by continuously sampling pad signals in analog memory arrays.

The AFTER chip samples detector pad signals at a user defined frequency (up to 50 MHz). In the case of the T2K TPCs the maximum drift distance is 90 cm. Given the electron drift velocity in the Ar:CF_4:iC_4H_{10} gas mixture (7.8 cm/μs) this distance is covered in approximately 12 μs. If we add the width of the T2K

neutrino beam (3 μs) we obtain an acquisition window of approximately 15 μs. To cover this window with enough safety we decided to set the sampling time to 40 ns that corresponds to an acquisition window of 20 μs.

Other important parameters of the AFTER chips are the charge range and the shaping time. The charge range establishes how many electrons correspond to one ADC count. We decided to set this parameter to 120 fC that corresponds to 183 electrons per ADC count.

The last parameter, the shaping time, describes the time that the electronics will wait to collect the incoming electrons and produce the signals. This parameter is set to 200 ns and this means that all the electrons that arrive in the 200 ns time window will be properly collected and contribute to the electric signal.

Front-End Cards

The Front-End Card performs three main functions: the digital conversion of 288 analog signals coming from a MicroMegas detector, the calibration of the conversion function, and the monitoring of the board, checking the board power supply and temperature. The calibration is performed generating a signal through a capacitance in series to simulate an analog signal of a precisely known amplitude. The digital conversion of the 288 analog signal is performed in several stages that can be summarised as follows:

- amplification and shaping, analog storage and signal multiplexing: these tasks are performed by the AFTER chips, that store the information in the Switch Capacitor Array;
- conversion of the analog signals to digital values performed by a commercial device.

Another important tasks of the FECs is to protect circuits from accidental over voltage due to spark in the detector: this is done using, for each pad, protection diodes connected to the ground.

Front-End Mezzanine

The Front-End Mezzanine is connected to 6 FECs and its main tasks are: to receive clock, trigger and synchronisation information from its DCC; to duplicate the signals to the six FECs; to receive event data digitised by the ADCs of the FECs and to deliver event fragments to its DCC. The required input bandwidth is one of the challenging aspects of the FEM: given a 20 MHz conversion rate for the quad-channel 12-bit ADC of each FEC, the FEM has to receive and store an aggregate data flow of 5.76 Gbit/s. Transmission to and reception from the DCC occurs at $\sim$ 2 Gbit/s each way. The core of the FEM is a large FPGA (field-programmable gate array) device that has to provide a few million gates, a couple of hundred I/O pins with an aggregate bandwidth of $\sim$ 20 Gbit/s.

Data Concentrator Cards

The signals coming from the FEMs are collected by the Data Concentrator Cards (DCC). Each of these cards is connected to four FEMs, so 18 DCCs are needed to readout the three TPCs. The DCCs are designed to distribute a reference clock to the front-end electronics and aggregate events from the 72 2 Gbps optical links: the events are then sent via a standard PC to the global data acquisition system of the experiment. An optical extension card has been designed to be able to connect four FEMs to each DCC. At the inter DCC level a Slave Clock Module (SCM) is used to fanout the global clock and the trigger information to the DCCs: each DCC is connected to the SCM . The central software element of the DCC is a command server program which receives orders from the TPC data acquisition PC over an Ethernet connection, decodes, translates and posts the corresponding commands to the front-end electronics over its optical communication links, receives the responses from the front-end, encapsulates them in Ethernet frames, and returns this information to the client PC. The requested acquisition rate is 20 Hz.

3.5 The TPCs calibration

One important task during the TPC operations is to assure that the data are taken in stable conditions for what concerns the gas properties, the electric and magnetic fields, the MicroMegas gain, and the front-end electronics. To monitor the TPCs during the runs two different systems are used: a laser calibration system, described in subsection 3.5.1, and gas monitoring chambers, introduced in subsection 3.5.2.

3.5.1 Laser Calibration system

To calibrate the TPCs, a UV-laser based calibration system is used. In this way, during the data taking, it is possible to provide a real time calibration of each TPC. This system is used to measure:

- Absolute electric field distortions,
- Absolute magnetic field distortions,
- Relative gain of the system (to correct for the temperature and pressure effects),
- Drift velocity.

A diagram of the laser setup is shown in figure 3.10: the laser used is a Nd:Yag UV laser that emits light at a wavelength of 266 nm. The light is then transported to the TPC readout plane with an optical fiber and is injected, from three different locations per endplate, into the TPC drift region arriving on the central cathode where a pattern of aluminum strips and dots is mounted. When they are illuminated by the UV laser flash the strips and the dots release electrons via the photoelectric effect. These electrons drift towards the pad plane where they are amplified and detected by the MicroMegas modules producing an image of the strips and of the dots (see figure 3.11). Any distortion in the electron drift, due to inhomogeneous electric or magnetic field, leads to a relative displacement of the expected pattern, and has an impact on the momentum measurement. Therefore, it is important to measure and take into account the field distortions since the TPCs aim to have an absolute momentum scale known at the 2 % level.

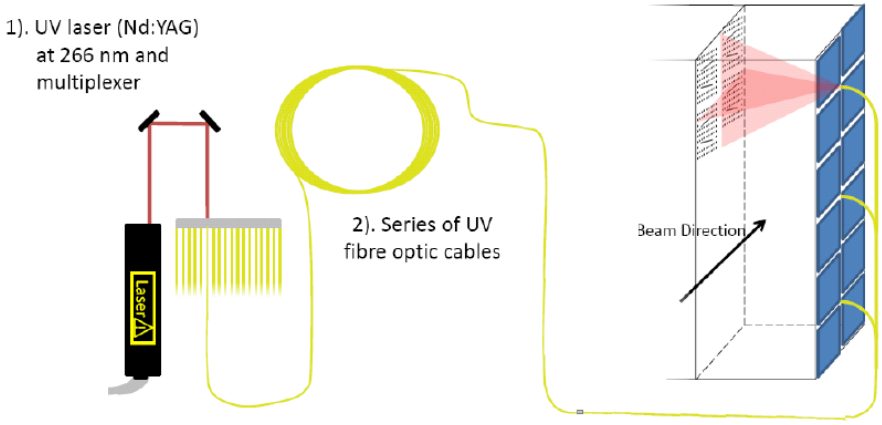

Figure 3.10: The laser system of the TPCs.

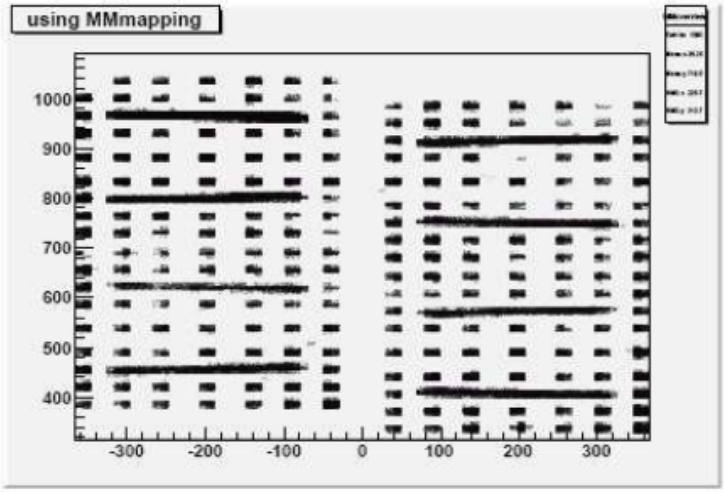

Figure 3.11: Laser event taken during the test with the first TPC in the M11 beam test area at TRIUMF. During the tests four MicroMegas modules were read and we can see the signal coming from the aluminium strips and dots.

3.5.2 Gas monitoring chamber

The gas monitoring chambers work using the same principle as the TPC in terms of gas ionisation, electron drift under a static electrical field and electron gas amplification. Their main task is to monitor the properties of the gas that is cir-

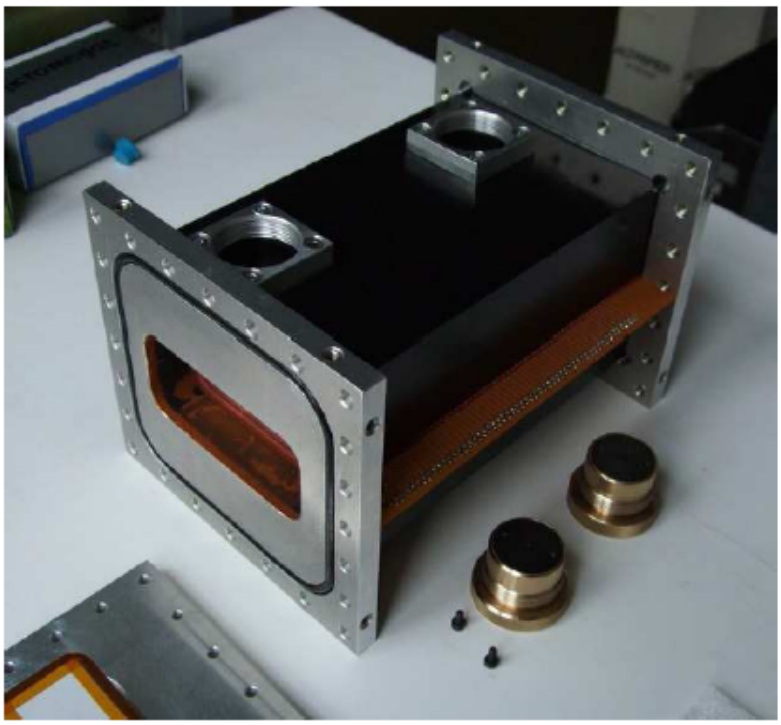

Figure 3.12: Picture of one of the monitor chambers.

culated in the large volume TPC. There are two monitoring chambers composed of a simple field cage (see figure 3.12) with a small sample gas volume where the same gas line that feeds the three TPCs is flowing and a MicroMegas readout module smaller than the ones used for the TPCs. One of the two chambers receives the gas at the beginning of the gas circuit, before entering the TPCs, while the second one receive the gas that is exiting from the TPCs.

On the cathode side an ^{55}Fe source and two ^{90}So sources are installed (see figure 3.13) that emit respectively 5.9 keV γ rays and β-decay electrons. The signals produced by these events are then amplified and detected on the anode by the MicroMegas module and their analysis allows the extraction of two important gas parameters: the drift velocity and the gain of the gas amplification. As the gas used in the monitor chambers and in the TPCs comes from the same gas line, the drift velocity and the gain are the same in both detectors.

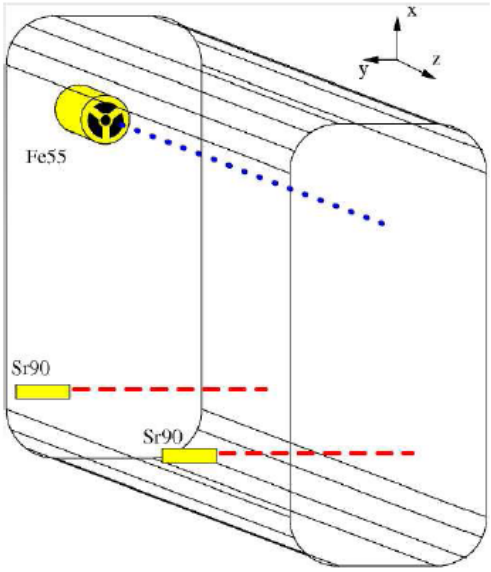

Figure 3.13: Layout of the monitor chamber.

3.6 The TPC performance

3.6.1 Tests of the TPC

The MicroMegas modules and electronics went through extensive test in 2006 and 2007 which validated the physics performance that could be reached with such detectors. In the following section we will give more recent performance results. Each of the MicroMegas modules was tested prior to its installation on a test bench at CERN (Figure 3.14). The validation tests, which provided measurements of the gain and resolution uniformity, edge effects, and count of the number of faulty pads. The energy resolution was measured with a 5.9 keV ^{55}Fe X-ray source illuminating single pads. The obtained spectrum (Figure 3.15) has a resolution of about 8 % at 5.9 keV. The typical r.m.s. (root mean square) dispersion or response uniformity of collected charge is better than 3 %, and only about 10 faulty pads were found out of more than 120 000 channels (<0.01 %).

The mechanical frame of the TPCs was built at TRIUMF (Canada) while the electronics and MicroMegas bulks were produced by a collaboration between the CEA of Saclay and CERN. Once the detectors and electronics were ready

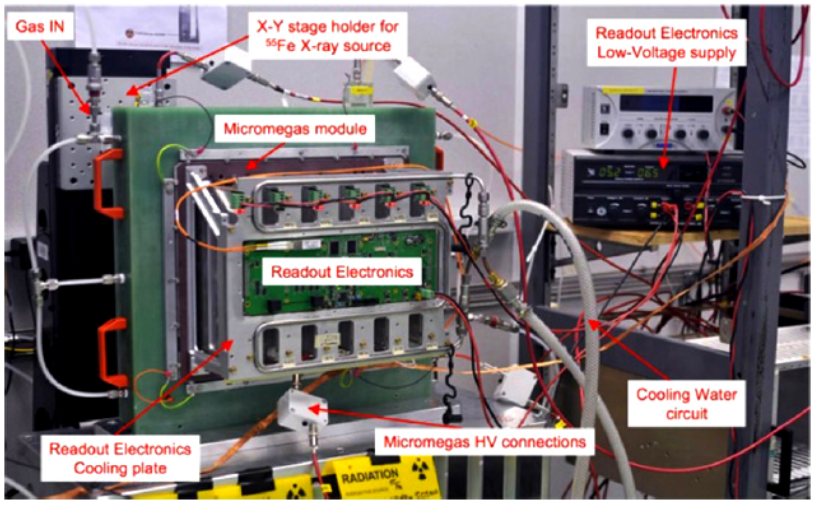

Figure 3.14: The MicroMegas module test bench at CERN. The mechanical arm containing the calibration ^{55}Fe X-ray source used to scan the module surface can be seen.

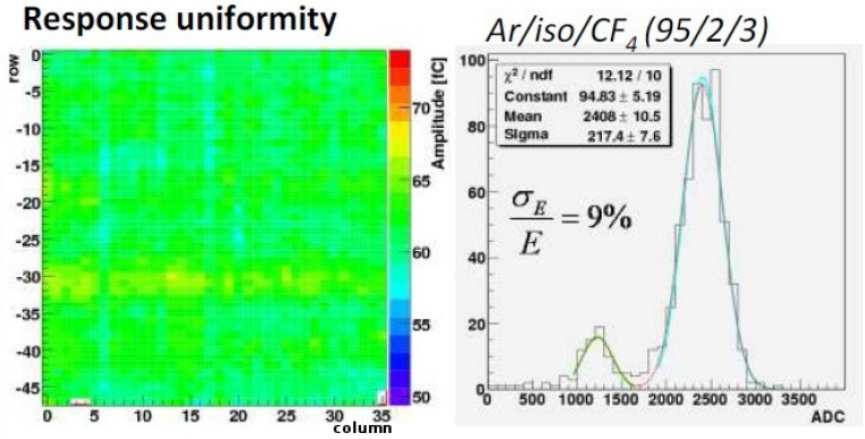

Figure 3.15: The left plot shows the uniformity of the pad per pad gain in arbitrary units. The right plot shows the energy spectrum of the ^{55}Fe source used for calibration and test purposes.

and tested in Europe, they were sent to TRIUMF to be mounted and tested once again, with the M11 beam which provided pions, electrons, and muons (Figure 3.16). The FGDs were also tested with this beam prior to their installation

in Japan.

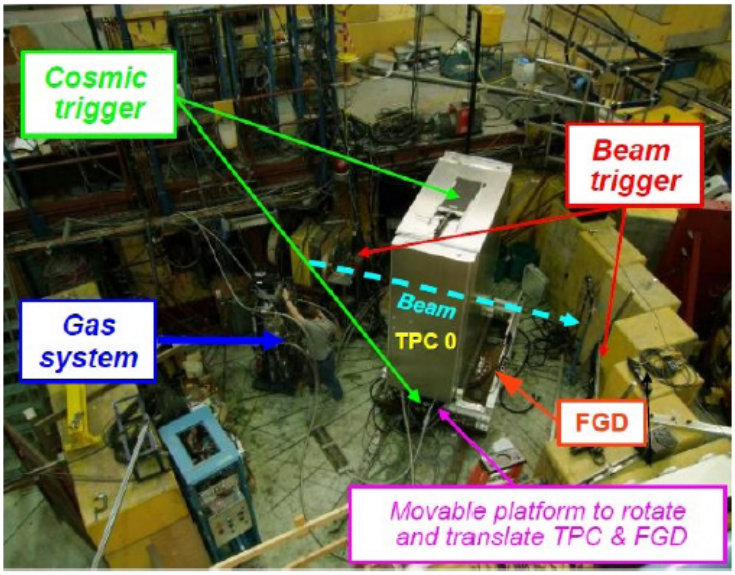

Figure 3.16: Layout of the test area at TRIUMF (Canada).

3.6.2 Spatial resolution

As we mentioned before, when a charged particle crosses a TPC, the deposited charge can be spread over a few pads. This neighboring pads are grouped into clusters, which are fitted to reconstruct the projection of the track on the readout plane. The spatial resolution is obtained through the comparison of the transverse coordinate computed by the global fit to the one resulting from a single cluster fit while fixing the other track parameters (angles and curvature). The residual distribution measured at TRIUMF is shown in figure 3.17 and the resulting spatial resolution is 650 μm at a 75 cm drift distance, which is good enough to obtain the required transverse momentum resolution of 10 % at 1 GeV.

Figures 3.18 and 3.19 show the spatial resolution as a function of the drift distance for all clusters and only for clusters consisting of two pads respectively, obtained with the T2K data. The resolution is degraded at short drift distance since the electron transverse diffusion is low and most of the clusters are just

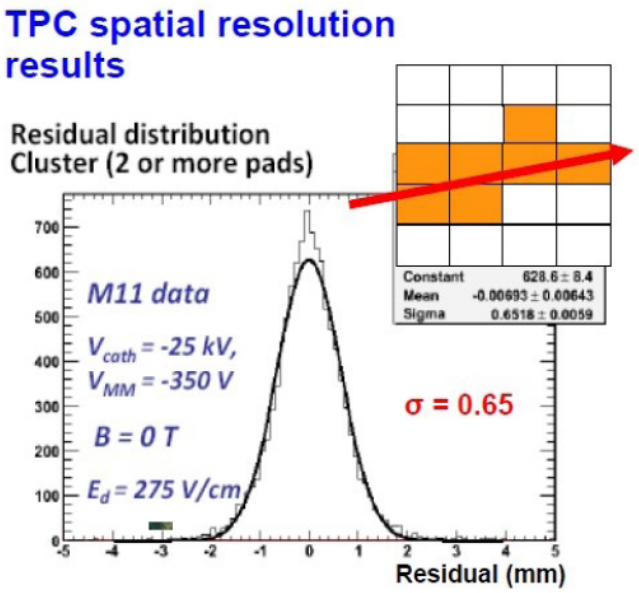

Figure 3.17: Spatial resolution measurement done at TRIUMF with beam data.

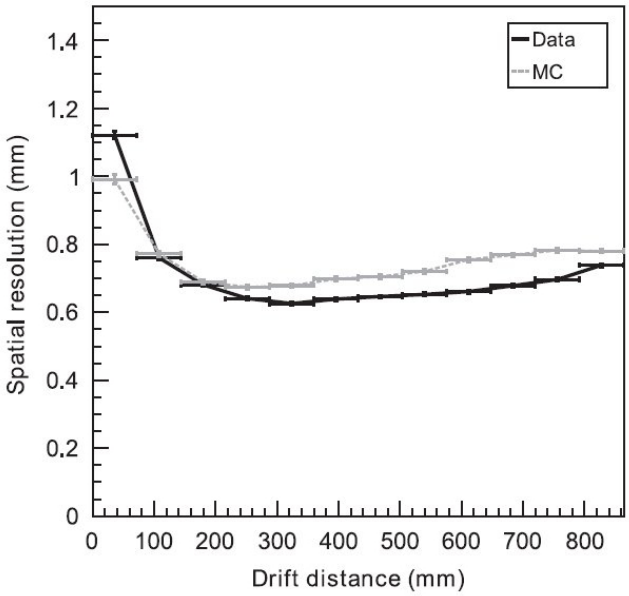

Figure 3.18: Spatial resolution per cluster as a function of the drift distance.

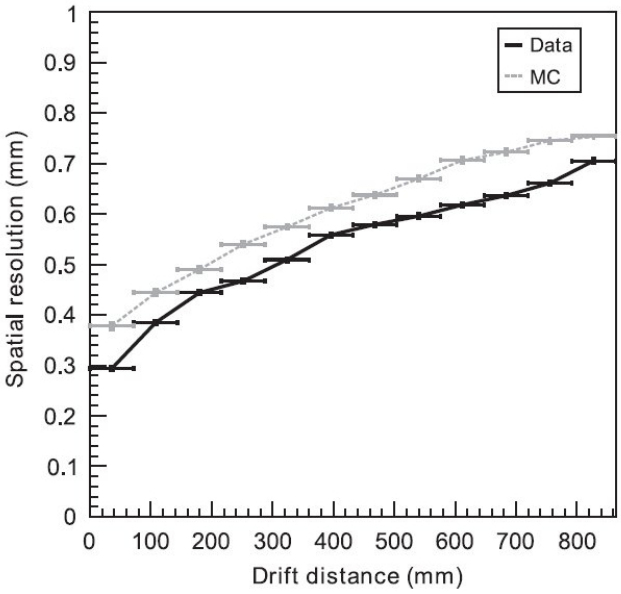

Figure 3.19: Spatial resolution as function of the drift distance for clusters made of two pads.

single pads, thus the resolution is limited by the pad size. The best resolution is obtained with clusters with two pads since the deposited charge per pad can be weighted to estimate better the true position of the point. Figure 3.19 also shows the dependence of the spatial resolution on diffusion, since for longer drifting distance, there is more diffusion and the resolution degrades. The results are compatible with those obtained at the TRIUMF beam tests: for a 75 cm drift distance the resolution is about 650 μm.

3.6.3 Particle identification

The particle identification (PID) in the TPC is based on the measurement of the truncated mean of the energy loss from ionisation by the charged particles crossing the TPC when interacting with the gas molecules. The method used consists in computing the mean value over the MicroMegas columns of the deposited charge by a charged particle crossing the TPC. This distribution is affected by the Landau tails produced by the ionisation processes in the gas and to remove

these tails we consider the mean value only of the 70 % of the MicroMegas columns with less charge.

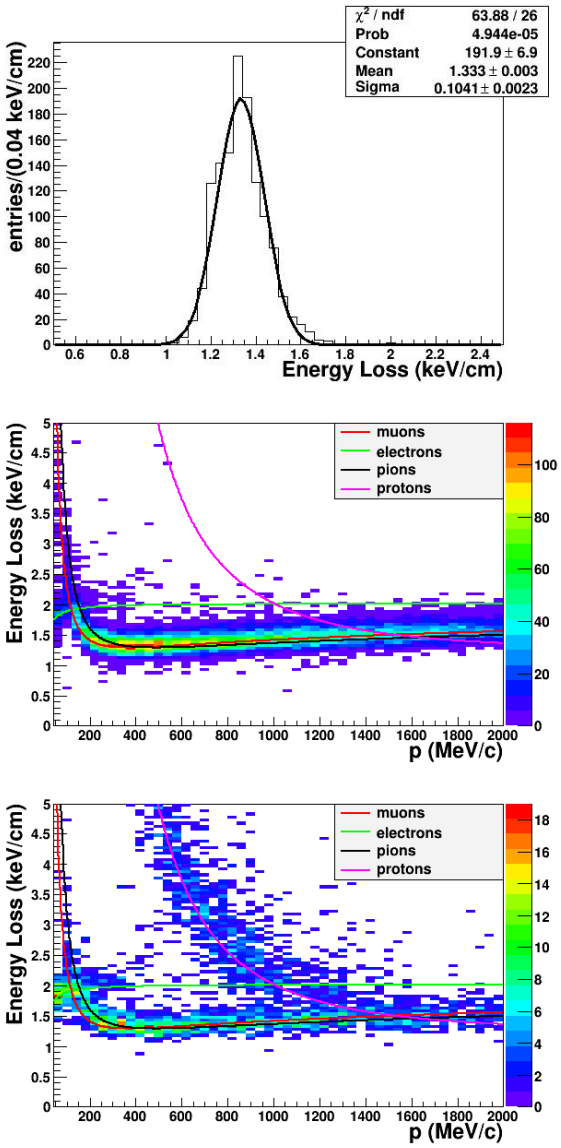

Figure 3.20: Deposited energy resolution (top) and deposited energy versus momentum for (middle) negative particles and (bottom) positive particles.

As the particle identification, which is one of the main goals of the TPCs, relies on the deposited energy (dE/dx), the measurement of the dE/dx resolution is also very important. The measured resolution on the energy loss is 7.8 ± 0.2 %

for minimum ionising particles (figure 3.20 top), which is better than the 10 % requirement for the T2K physics program. With this resolution, the probability to misidentify a muon as an electron is 0.2 % for tracks with a momentum below 1 GeV/c. The distributions of the energy loss as a function of the momentum for data taken during the first T2K physics run are shown in figures 3.20. The data is compared to the expected curves for muons, pions, protons, and electrons, and is in good agreement with the expected values. The studied sample contained mainly negatively charged muons (Figure 3.20 middle), positively charged pions and protons (Figure 3.20 bottom).

Chapter 4

Data quality

For one year and a half during run 3 and run 4, I have been in charge of the data quality of the TPC. After an overview of data quality in section 4.1, the checks to verify the data quality for the TPC are described in section 4.2. Section 4.3 gives a summary of the data quality results.

4.1 Overview

4.1.1 Aim of data quality

The aim of the data quality is to assess and control the quality of the data, both beam and cosmics, collected by ND280. This is used to define the set of data available for the analyses and to obtain the corresponding number of POT for normalisation.

There are several criteria that are used by the sub-detectors to assess the quality of the data, starting from the hardware status of the detector and using also some reconstructed variables.

4.1.2 Organisation of data taking

When taking data, there is always a team of three physicists taking care of the near detector, including ND280 and INGRID. They stay in the counting room at

J-PARC for eight consecutive hours. They perform the first checks on the quality of the data being registered. They are:

- the shift leader, in charge of the shift. In particular he should call the relevant experts, if needed, in case of problems.
- the DAQ (data acquisition) shifter, responsible for the data acquisition of the experiment, who does also a lot of data quality checks.
- the safety shifter, monitoring various quantities and plots, related to the detector safety or data quality, and making a tour of the facility twice per shift.

In addition, there is one on-call expert per sub-detector, in charge for at least one week. For TPC, the most complex sub-detector, there used to be two experts in the early period of data taking. There is still a second expert at the start of each new running periods.

Finally, there is a more permanent data quality expert for each sub-detector. Unlike the shifters and on-call experts, the data quality expert does not need to be at or near J-PARC, or even in Japan. While being data quality expert for the TPC for the physics runs 3 and 4, I was based at Saclay.

The data quality experts for all sub-detectors meet every week during data taking periods, usually on Wednesday, through a virtual conference using the EVO network service. The goal is to assess the quality of the data registered during the previous week. A week of data is defined here as data taken between Sunday at 00:00 (i.e. at midnight in the night from Saturday to Sunday, japanese time) to the next Sunday at 00:00. Automatic jobs are submitted in batch on Sundays on the semi-offine cluster at J-PARC to perform various data quality tasks. The code is put together in the soffTasks (for semi-offline tasks) package. The jobs are usually completed on Mondays, which leaves enough time to the data quality experts to exploit the results and report about them at the data quality meeting on Wednesdays.

4.2 TPC data quality

We review in this section the criteria used to check the basic performance of the detector in the case of the TPC.

4.2.1 Pedestals

For each electronic channel, the pedestal measures the response of the electronic channel in the absence of physics signal. The TPC has got more than 120,000 electronic channels, with a pedestal RMS around 4 ADC counts. However, a few channels, flagged as bad channels, have a much larger RMS. In order to minimise the event size during data taking, only hits above a threshold defined as the pedestal mean value plus 4.5 times the pedestal RMS are recorded. Thus it is very important to have correct pedestal values, neither to lose valuable information, nor to record useless information.

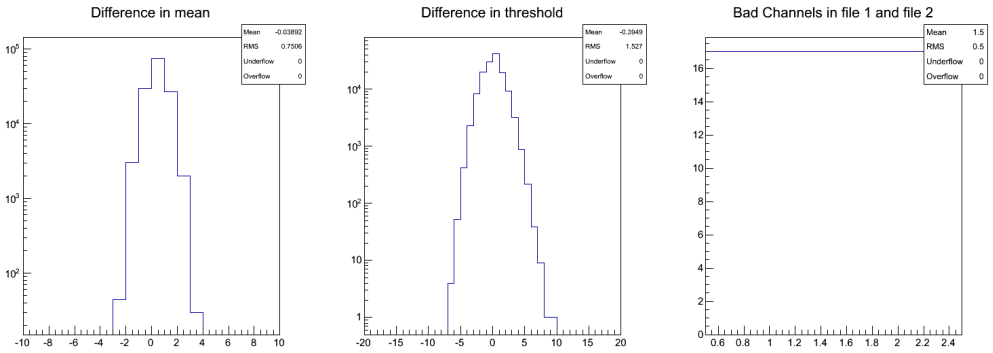

Figure 4.1: Comparison of two pedestal runs: (left) difference in pedestal mean values, (middle) difference in thresholds, both as a function of number of ADC counts, and (right) number of bad channels in two bins: old pedestal run (bin 1) and new pedestal run (bin 2).

The pedestals can be determined either in local DAQ or global DAQ. In the first case, a special standalone run of the TPC is performed. In the second case, random pedestal triggers are recorded during normal data taking, outside the beam time windows in order not to create deadtime for beam triggers.

Pedestals are regularly (weekly or after a restart) checked by comparing two different pedestal runs, as shown in figure 4.1. The differences in mean values and in thresholds are sharply peaked at zero, which illustrates the fact the pedestals are very stable. Similarly, the number of bad channels with very large pedestal RMS was constant during data taking. There were 17 such bad channels.

4.2.2 Sparks

MicroMegas modules do spark occasionally, i.e. electric discharges between the mesh and the pads can happen. The spark rate for each MicroMegas module is monitored to check its stability over time, as a reduced or increased spark rate could indicate a problem with this module. This is done each week by the TPC data quality expert (by running the toolSparkChecker.exe executable in the oaSlowControlDatabase package). An average spark rate of two sparks per day is observed in average for each MicroMegas module.

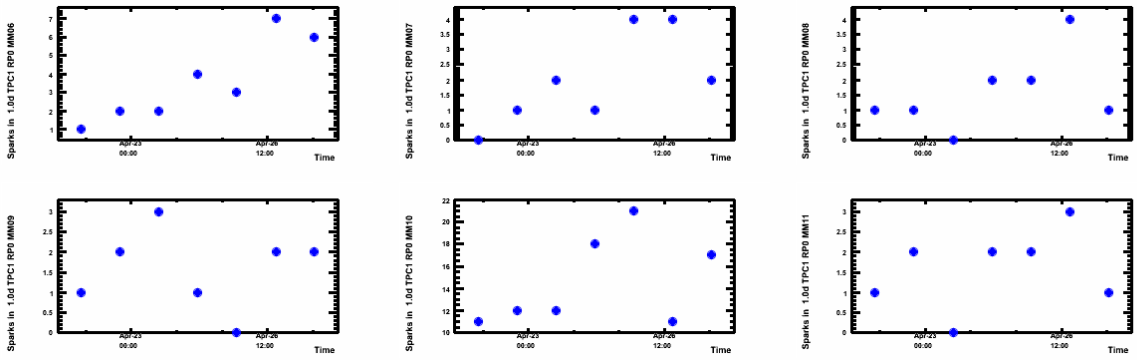

Figure 4.2: Evolution with time over one week of the number of sparks for six MicroMegas modules of TPC1. While almost all of them have an average spark rate around two per day, module MM10 (bottom middle) has a rate almost ten times higher.

However there is one MicroMegas module in TPC 1, RP0 MM10 (module number 10 in readout plan 0), which is known to have a higher spark rate up to 20 per day, as shown in figure 4.2. In fact, starting in November 2010, this module could not be powered to the nominal high voltage, as it continuously

tripped. The problem was fixed by disconnecting one twelfth of the pads of this module. Although we lost all information on these pads, we regain the remaining eleven twelfths of the module. However, since then, its spark rate has been higher than the usual value.

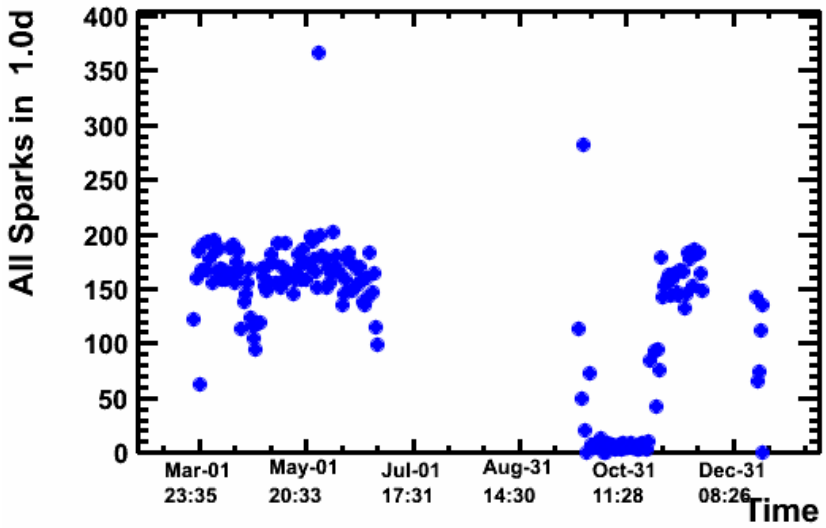

Figure 4.3: Evolution with time of the total number of sparks for all MicroMegas modules in the three TPCs during 2012.

The spark rate is fairly stable, as shown in figure 4.3 for the whole year 2012. The period in October when the spark rate seems very low, is due to the fact that, after a software upgrade, the spark definition was incorrectly set in the code. When the correct parameters, especially the duration required for the spark, were entered to properly define sparks, the spark rate went back to its usual value.

4.2.3 Latency

The TPC latency measures the time taken by the TPC to read out an event. If it is too long, the data acquisition will not be ready for the next trigger. This will lead to some deadtime and loss of useful events. This effect is very small. However it is monitored and a weekly check of the latency is performed. This is illustrated

in figure 4.4, where the latency is shown as a function of the event size for the different type of triggers. Beam and cosmics triggers have a similar behaviour, with a latency around 32 ms, rather independent from the event size. However, when the event size is higher than 12 kB, the latency starts to rise. Laser triggers (see section 3.5.1) illuminate a large fraction of the TPC, and have a high latency around 56 ms and event size around 14 kB. Finally pedestal triggers are small, around 2 kB, but have a large latency, which was substantially reduced by an improvement introduced in the data acquisition code on February 27, 2013.

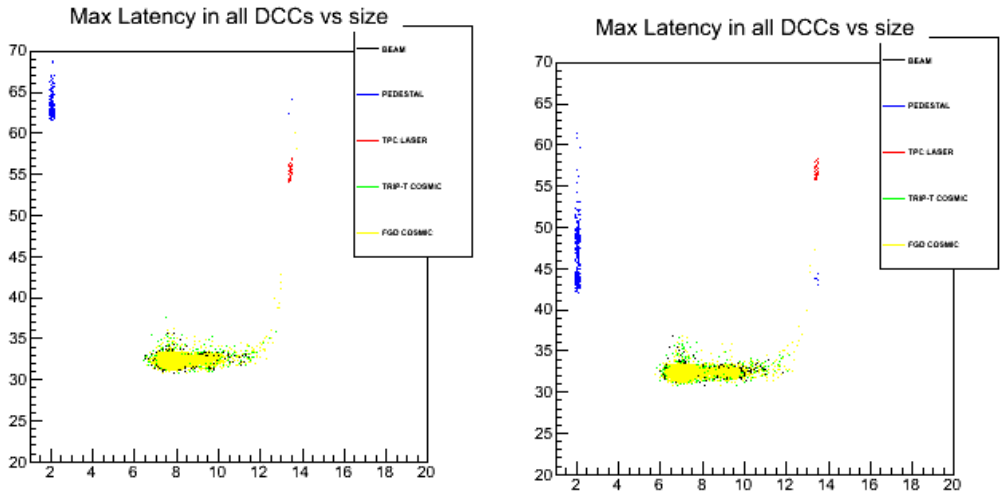

Figure 4.4: Maximum latency (in ms) in all DCCs as a function of event size (in kB) for the various triggers: beam in black, pedestal in blue, laser in red, cosmics triggered in Trip-T detectors in green, and cosmics triggered with the FGD in yellow. The left plot is for data taken before February 27, 2013, while the right plot shows data taken after that date, when the data acquisition code was improved to reduce the pedestal trigger latency.

4.2.4 Number of nodes

The weekly data quality jobs running on the semi-offline cluster do reconstruction of the data. An important quantity to check is the number of nodes for the reconstructed tracks, illustrated in figure 4.5. It has a smaller peak at 36 nodes

for tracks crossing one MicroMegas module and a bigger peak at 72 nodes for tracks crossing two MicroMegas modules.

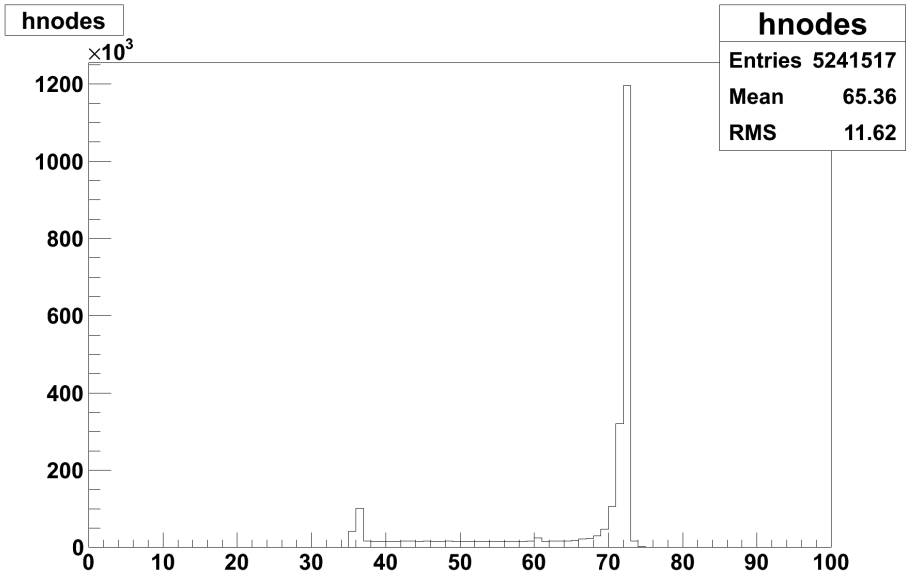

Figure 4.5: Number of nodes on reconstructed TPC tracks.

4.2.5 Ionisation

Other reconstructed quantities, such as the energy loss dE/dx, are produced by the soffTasks runs. To monitor this quantity, the TPC expert makes plots of dE/dx mean value and RMS over time, in 12 bins of muon momentum for cosmic triggers. The momentum bins, expressed in GeV/c, are: [0.0,0.2], [0.2,0.3], [0.3,0.4], [0.4,0.5], [0.5,0.6], [0.6,0.7], [0.7,0.8], [0.8,0.9], [0.9,1.0], [1.0,1.2], [1.2,1.5], and [1.5,2.0].

Such plots are shown in figure 4.6 for the mean value and in figure 4.7 for the RMS for one week in 2013. The same plots are shown in figure 4.8 for the mean value and in figure 4.9 for the RMS over the whole year 2012. They show rather stable values.

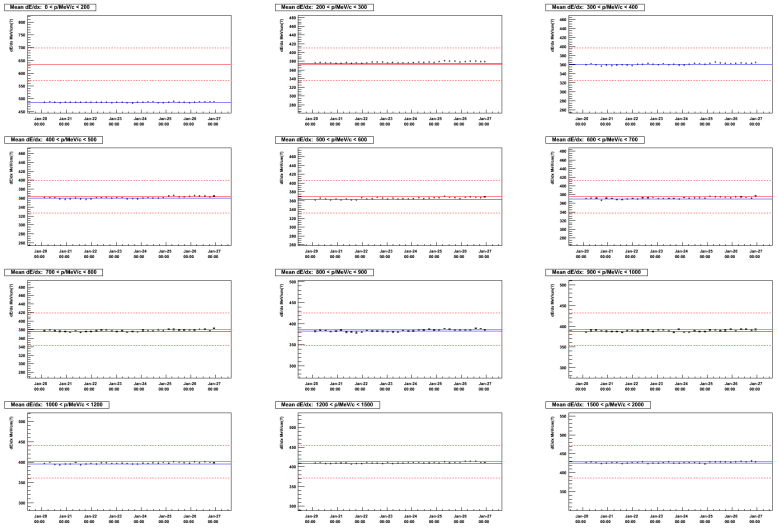

Figure 4.6: Mean value of dE/dx over time in 12 bins of momentum. The points correspond to cosmic triggers, sampled every 10 subruns. The solid red line shows the expected dE/dx value (which is not correct for the first momentum bin). The dashed red line shows this expectation $\pm 10\%$.

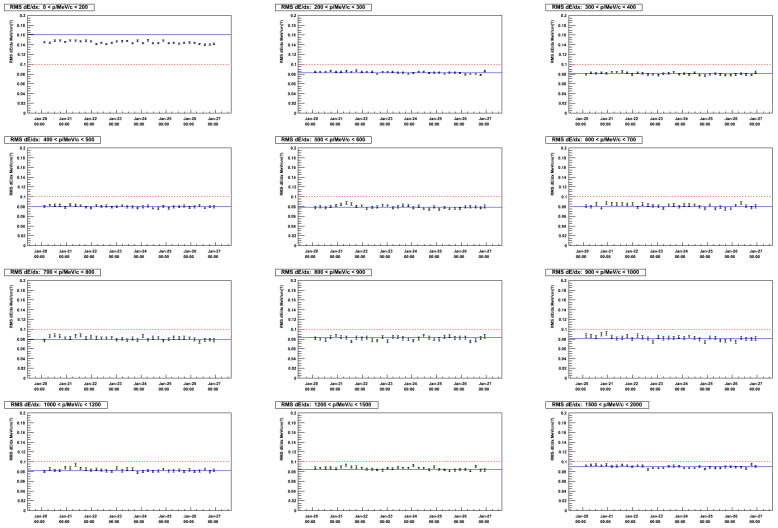

Figure 4.7: RMS of dE/dx over time in 12 bins of momentum. The points correspond to cosmic triggers, sampled every 10 subruns. The dashed red line is at 10 %. The blue line correnponds to the RMS of dE/dx of the previous week.

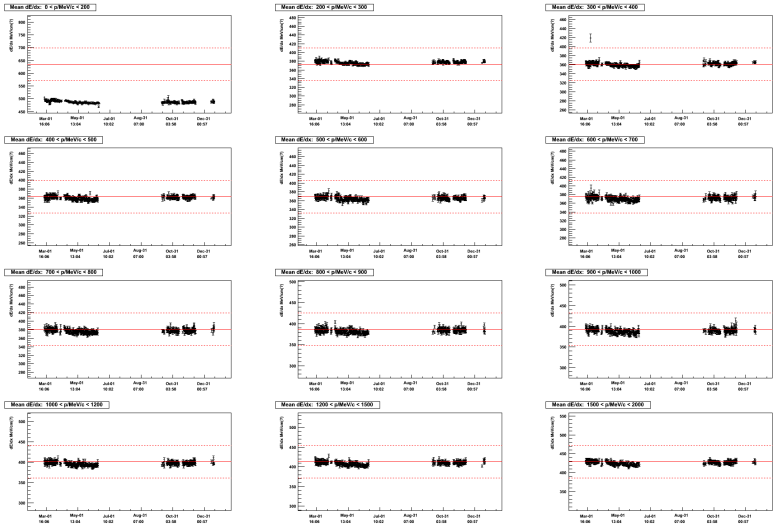

Figure 4.8: Mean value of dE/dx over time in 12 bins of momentum for 2012. The points correspond to cosmic triggers, sampled every 10 subruns. The solid red line shows a first estimate of the expected dE/dx value (which is not correct for the first momentum bin). The dashed red line shows this expectation $\pm 10\%$.

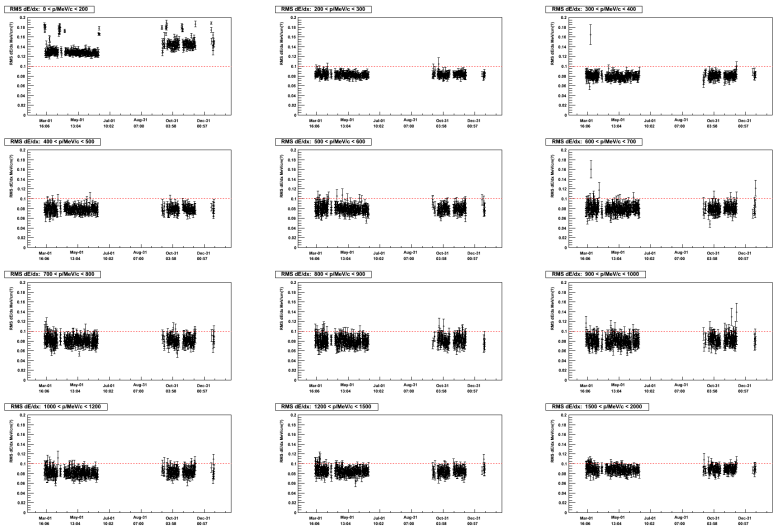

Figure 4.9: RMS of dE/dx over time in 12 bins of momentum for 2012. The points correspond to cosmic triggers, sampled every 10 subruns. The dashed red line is at 10 %.

4.2.6 Transverse diffusion

The transverse diffusion of the drifting electrons is also monitored during data taking.

The coefficient measuring the transverse diffusion mainly depends on:

- the value of the magnetic field, as illustrated in figure 4.10. It is smaller, with a value around 237 $\mu\text{m}/\sqrt{\text{cm}}$, when the magnetic field is switched on, while its value is around 280 $\mu\text{m}/\sqrt{\text{cm}}$ with no magnetic field.
- the value of the gas density (which varies according to the atmospheric pressure), as illustrated in figure 4.11. There is a clear anticorrelation between these two quantities.

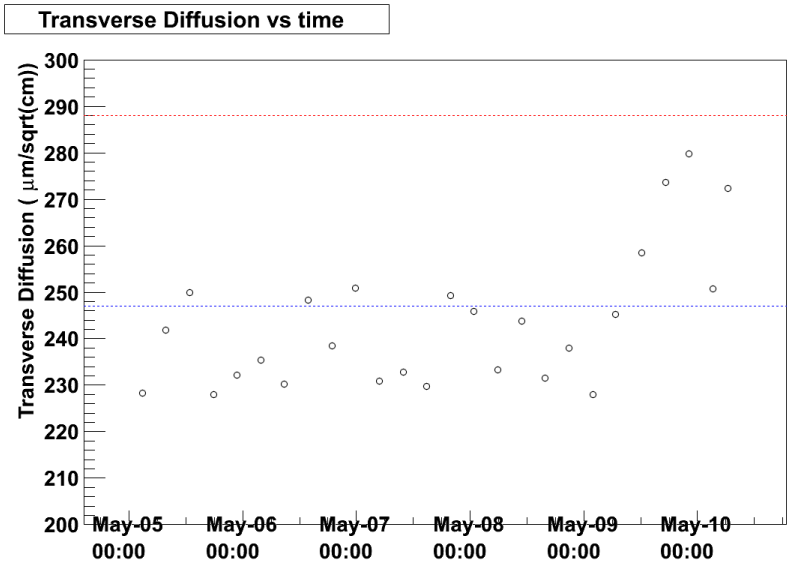

Figure 4.10: Time evolution of the transverse diffusion coefficient over one week. The effect of the magnet switch off on May 9, 2013 is clearly visible by the increase of the transverse diffusion coefficient from around the blue line (prediction with magnet on) towards the red line (prediction with magnet off).

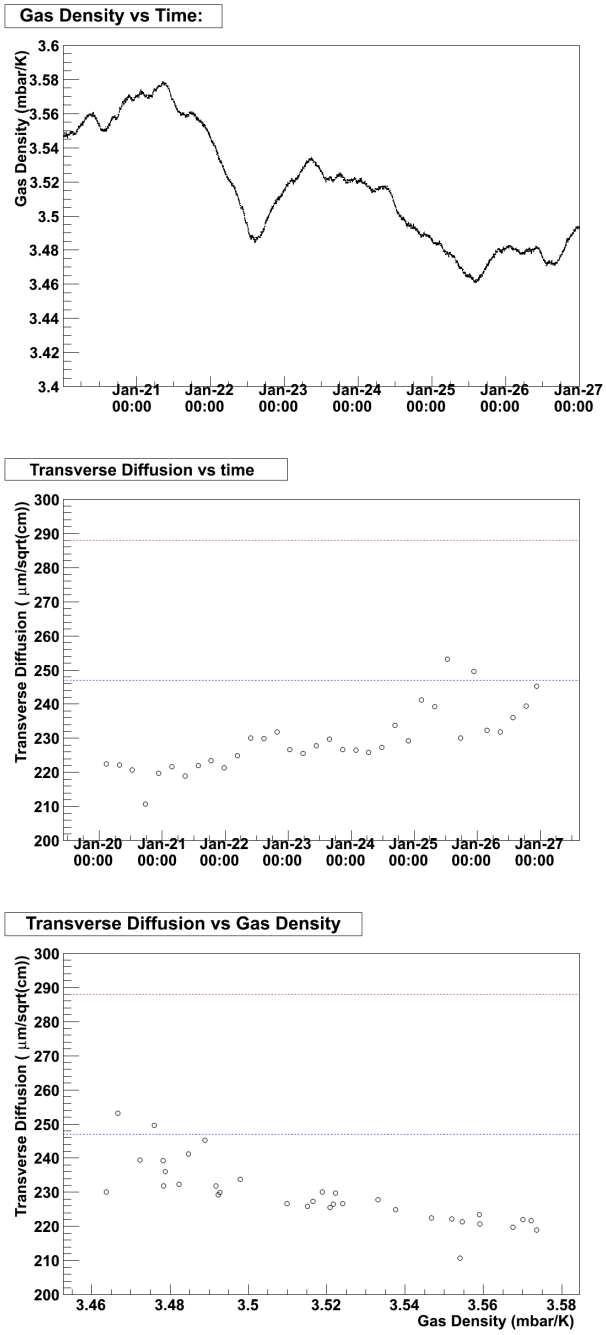

Figure 4.11: Evolution over time of (top) the gas density and (middle) the transverse diffusion coefficient and (bottom) correlation between these two quantities.

4.2.7 TPC status and livetime

The status of each sub-detector is expressed as the value of a flag. A value of zero is given if the data quality is good. A bad status (non zero value) is given when the detector is not in normal conditions. For the TPC, table 4.1 summarises the meaning of the non null values for the data quality flag. Each bad condition is expressed by a bit, coded as a power of 2, up to $2^7 = 128$ in the initial schema (used for runs 1 and 2) when all three TPCs were considered together, and up to $2^{31} = 2147483648$ in the final schema (used for runs 3 and 4), when TPC1, TPC2, and TPC3 are treated separately. To ensure the compatibility of both schemas, the new one starts at $2^8 = 256$. The total flag is the sum of the flags of all bad conditions being present at a given time. For example, a flag of $525312 = 1024 + 524288$ would mean that there is a MicroMegas problem in TPC1 and a DCC problem in TPC2.

	Initial Schema	TPC 1	TPC 2	TPC 3
LV problem	1	256	65536	16777216
FEM problem	2	512	131072	33554432
MM problem	4	1024	262144	67108864
DCC problem	8	2048	524288	134217728
CC problem	16	4096	1048576	268435456
No GSC data	32	8192	2097152	536870912
Bad gas	64	16384	4194304	1073741824
ODB	128	32768	8388608	2147483648

Table 4.1: Meaning of each bit in the TPC data quality flag.

The generation of the TPC flag is a responsability of the TPC data quality expert. (The flag is created by running a script, ToolTPCStatus.exe, in the oaSlowControlDatabase package.) The ouput plots over a period of one week, between February 24 and March 6, 2013 as an example, are illustrated in figure 4.12 for the TPC flag and in figure 4.13 for the TPC lifetime, defined as the fraction of time when the TPC takes data in nominal conditions. During that week, there was a period with no beam of one hour and a half, when the TPC was taken out of global DAQ, to perform local tests. Thus, the value of the TPC flag ($32768 + 8388608 + 2147483648$) during that short period corresponds to the

ODB bits set on for TPC1, TPC2, and TPC3. Otherwise the flag value is zero, is the TPC was fully on. Similarly the lifetime equals 1, except for the time bin that includes the short period when the TPC was not in the global DAQ.

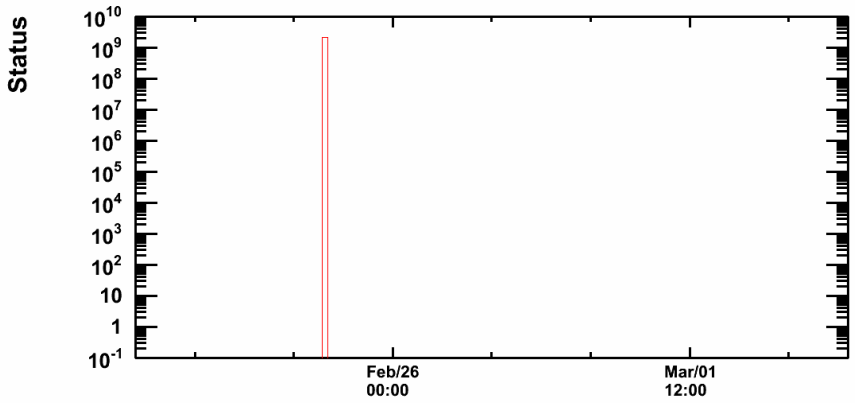

Figure 4.12: Evolution of the flag giving the TPC data quality status over one week.

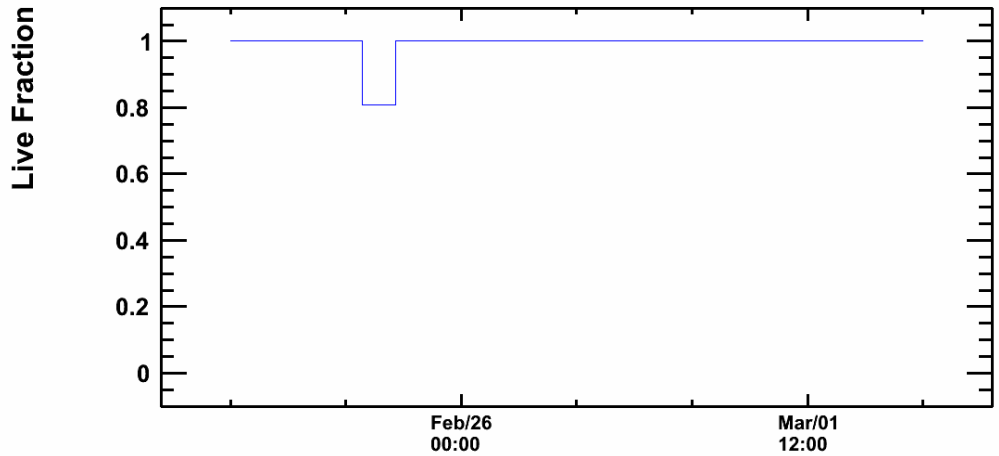

Figure 4.13: Evolution of the TPC livetime over one week.

The script queries the Global Slow Control (GSC) database, which keeps track of alarms and warnings on the detector, to check the following bad conditions:

- the low voltage power for the front-end electronics is off.
- at least one FEM is powered off.
- at least one MicroMegas module has its high voltage off.
- at least one DCC is powered off.
- the central cathode is powered off.
- there is no GSC data.
- the gas mixture is not the right one.
- TPC is not in global data acquisition, in which case the ODB flag is set.

During some periods of data taking, there was a problem with the optical link between the front-end electronics and the slow control system, that checks various quantities, such as the voltages, currents, and temperatures. One or two FEMs, or for some time, all the FEMs of TPC3, did not respond. Though they were powered up and otherwise working perfectly, it was not possible for the slow control to check their status. So the TPC flag would have been non zero in this case, with the 'FEM powered off' bits on, although there was no real issue with data quality. In order to avoid changing the flag value by hand, the possibility to disable the checking of the FEMS was introduced, FEM by FEM. The same was done for the DCCs. Masking one or several FEMs or DCCs can be done by modifying a simple text datacard, before running the ToolTPCStatus.exe script.

The script produces a text file containing the values of the TPC flag, as well as the start time and end time of the validity period (coded in unix time). The file is first uploaded in a test database. After the flags are approved at the Wednesday weekly meeting, the file is uploaded in the calibration data base. Afterwards, the values of the data quality flags are available for all physicists in T2K, when reading the data. Therefore, they can select the data with all detectors working fine or, according to their analysis, some explicit detectors working fine.

Figure 4.14 illustrates the TPC lifetime during all run4. There were several beam shutdowns during that period, shown on the plot with a lifetime value at zero. But when the beam was on, the TPC status was almost always good.

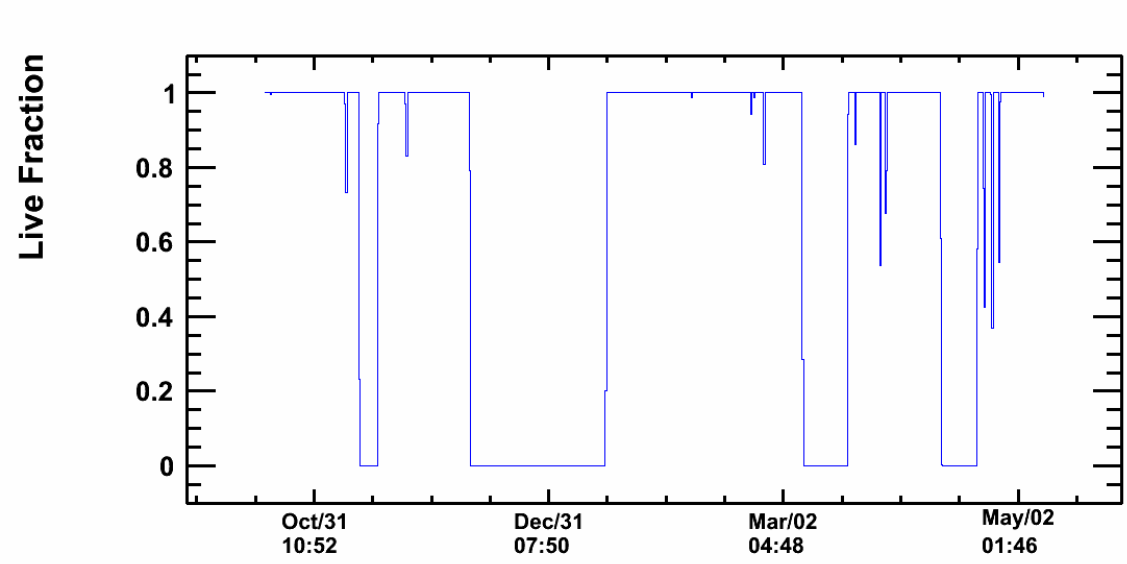

Figure 4.14: Evolution of the TPC lifetime over all run4. The long periods with lifetime at zero correspond to beam shutdowns between different main ring runs.

4.3 Summary

Figure 4.15 illustrates the efficiencies of the ND280 detector and of the data quality requirements on the number of POT collected during the four running periods, which are given in table 4.2.

	Run 1	Run 2	Run 3	Run 4	Total
Delivered POT (10^{20})	0.311	1.120	1.592	3.373	6.397
Recorded POT (10^{20})	0.299	1.085	1.580	3.337	6.301
DQ good POT (10^{20})	0.165	0.789	1.570	3.245	5.769
ND280 efficiency (%)	95.9	96.9	99.3	98.9	98.5
DQ efficiency (%)	55.2	72.7	99.4	97.2	91.6
ND280+DQ efficiency (%)	53.0	70.4	98.6	96.2	90.2

Table 4.2: Efficiencies of the ND280 detector and of the data quality requirements for all ND280 detectors.

There were two major periods, when a large fraction of data had to be rejected by the data quality group. The first one was at the end of run 1 in May and June

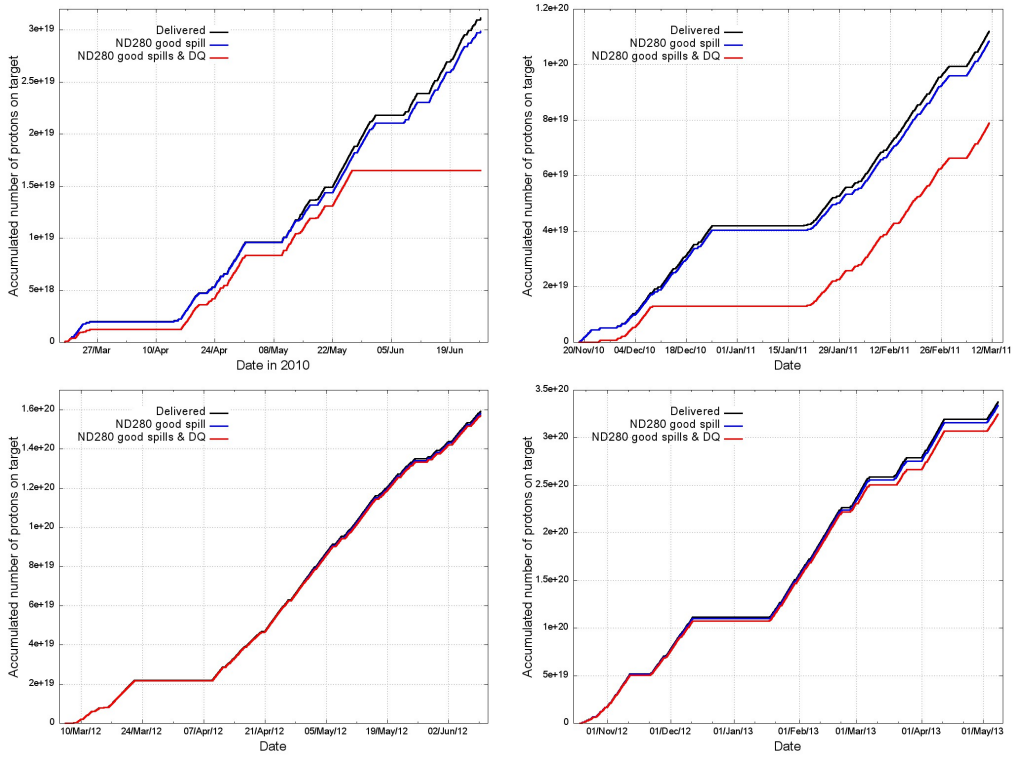

Figure 4.15: Accumulated number of protons on target for (top left) run 1, (top right) run 2, (bottom left) run 3, and (bottom right) run 4. The black line shows the number of POT delivered by the accelerator, the blue line the number of POT recorded by ND280, and the red line the number of POTs after the ND280 data quality requirements for all ND280 detectors.

2010 and was due to problems in FGD. The second one was at the beginning of run 2 in December 2010 and was due to TPC: one FEM in TPC3 died on December 9. So TPC ran without one MicroMegas module until the Christmas shutdown. During runs 3 and 4, all ND280 detectors have been essentially fine with a data quality efficiency greater than 97 %.

This is the data sample which will be used in the analysis described in the next chapters.

Chapter 5

The event selection

In this chapter, the event selection is described. The data sample used in the analysis is first defined in section 5.1. Section 5.2 deals with the muon selection used for the inclusive charged current ν_μ interaction analysis, which will be presented in the chapters 6 and 7. Section 5.3 presents a selection of events with one muon and one electron or positron, which could be used in a future measurement of cross sections of neutrino interactions producing at least one neutral pion.

5.1 Data sample

The analysis is based on the full data sample of the T2K experiment, taken until May 2013, which includes runs 1, 2, 3, and 4, after requiring a good global TPC data quality flag (see section 4.3). The number of corresponding POTs is given in table 5.1. The amount of POTs of the total data sample is 5.86×10^{20}.

Two samples of simulated data are also used in the analysis. The first and main one is created with the NEUT generator [30] for the ν interaction, while the second one is produced with the GENIE generator [54]. Both use the GEANT4 package [55] for detector simulation. The simulation is done run by run, with similar conditions as in real data. The total number of POTs is 38.95×10^{20} for the NEUT sample and 37.66×10^{20} for the GENIE sample. This is between six and seven times the statistics of real data for each Monte Carlo (MC) sample.

Note that, as it will be explained in more details in subsection 6.2.1, the Monte Carlo samples were not generated with the most up to date neutrino flux. The

Number of POT (10^{20})					
	Run 1	Run 2	Run 3	Run 4	Runs 1-4
Data	0.299	0.786	1.564	3.212	5.860
MC NEUT	2.00	5.875	11.495	19.58	38.95
MC GENIE	1.995	5.70	9.98	19.985	37.66

Table 5.1: Numbers of POT for data and Monte Carlo samples.

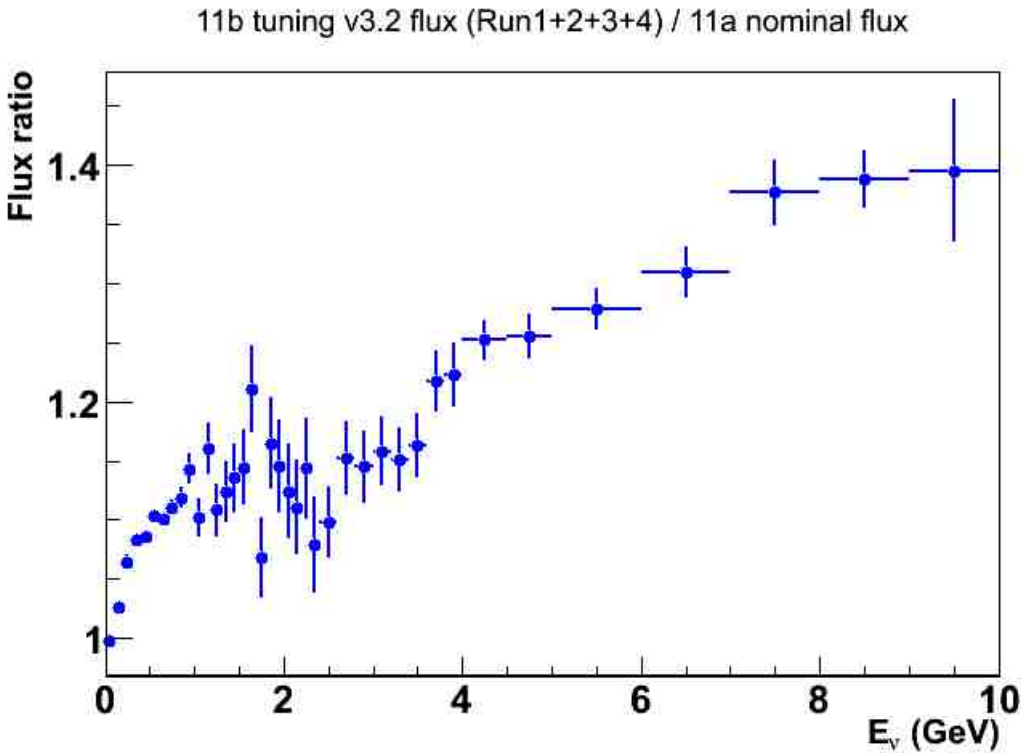

Figure 5.1: Flux ratio of the up to date flux prediction over the flux used for the Monte Carlo generation for ν_μ.

MC generation used the neutrino flux release 11a, while our best knowledge of the neutrino flux is contained in release 11b v3.2. Consequently, in order to do a meaningfull comparison between data and Monte Carlo, the simulated neutrino events have to be reweigthed as a function of the neutrino true nature and true energy. In this thesis, all the plots comparing data and Monte Carlo use the reweighted Monte Carlo (but the tables giving numbers of events in the Monte Carlo don't). The weight is the ratio of the last flux prediction over the flux prediction used for the generation at a given value of the neutrino true energy. This flux ratio is shown in figure 5.1 for ν_μ. It is greater than 1, since the latest measurements from SHINE give a higher rate of hadron production, in particular for kaons, and thus predict a higher neutrino flux, especially at high energy. Similar flux ratios exist also for ν_e, $\bar{\nu}_\mu$, and $\bar{\nu}_e$.

The real data, as well as the simulated data, are reconstructed using the official packages of the experiment. In a first step, the reconstruction is done for each subdetector individually, for example with the *tpcrecon* package for the reconstruction in the TPC. Then in a second step, the results are put together to create global tracks, which may have several segments in various subdetectors. The analysis described below uses these global tracks.

5.2 Inclusive charged current selection

The selection of inclusive charged current muonic neutrino interaction is based on the selection of a muon candidate. The criteria used in this selection are reviewed in subsection 5.2.1. The selected sample is described in subsection 5.2.2. The division of the sample in two subsamples according to the event topology is introduced in subsection 5.2.3, in order to have one subsample enriched and the other depleted in deep inelastic scattering events.

5.2.1 The different steps in the muon selection

We are interested in charged current (CC) neutrino interactions. The main product of this interaction is the negatively charged lepton. In our case, the ν_μ CC

interactions are tagged by the negatively charged muon. Figure 5.2 shows a display of such an event, where a ν_μ CC interaction in the FGD produces a muon. The muon track is most of the time the most energetic track among all the tracks corresponding to negatively charged particles in the event and consequently is selected as such.

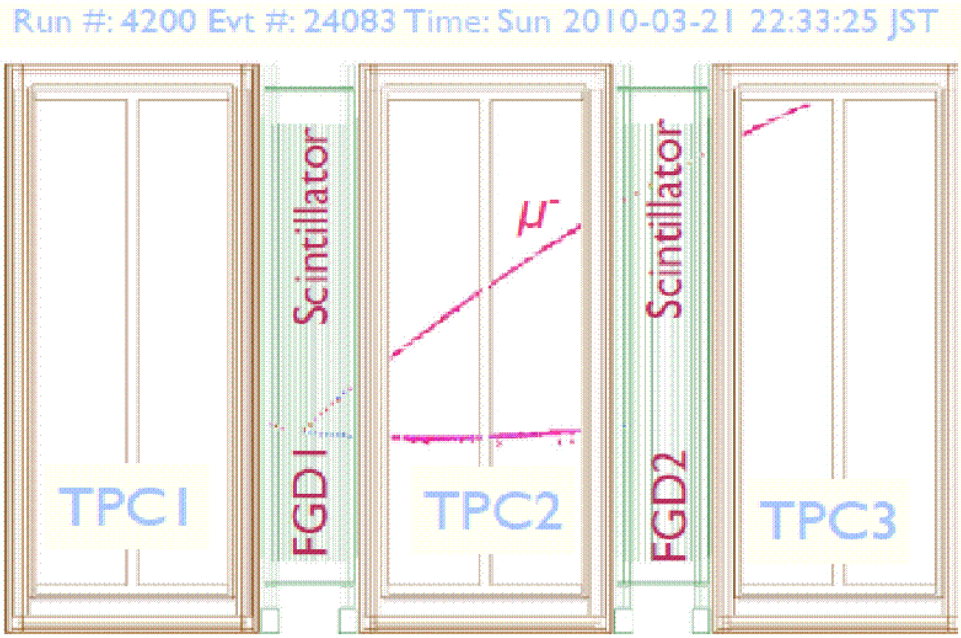

Figure 5.2: Side view of a charged current ν_μ interaction candidate in the tracker region of the near detector, which shows the bending due to the magnetic field. The muon candidate is recontructed with an angle of 40° and a momentum of 566 MeV/c.

The aim of the present inclusive ν_μ CC interaction analysis is to measure the cross section of Charged Current Deep Inelastic Scattering (CCDIS), including CC multi-pions interactions, using the interactions that take place in the FGD fiducial volume (FV). Thus, the exact definition of the FGD FV target is important. Besides, the cross section depends on the number and the type of the nuclei of the FGD which the neutrino interacts with.

In this section, we will explain in order each of the cuts designed for the inclusive CC selection. Firstly, to avoid pile-up and cosmics events, the timing bunch conditions are applied for each global track in the events (subsection 5.2.1.1). Secondly, the highest momentum track corresponding to a negatively charged particle is chosen (subsection 5.2.1.2). Thirdly, the track start position has to be be contained in the FGD FV (subsection 5.2.1.3). Fourthly, to insure a good quality of the track, we cut on the track length (subsection 5.2.1.4). Then, in order to keep only the neutrino interactions inside the FGD FV, we remove the backward tracks and we put a veto on the upstream TPC (subsection 5.2.1.5). Finally, the selection of the muon particle is based on the particle identification (PID) cuts (subsection 5.2.1.6): the track has to be compatible with the muon hypothesis.

5.2.1.1 Bunching

The neutrino beam is delivered in spills, containing six bunches during run 1, and then eight bunches in runs 2, 3, and 4. Thanks to the precise timing reconstruction in the FGD, the tracks are grouped together into these time bunches. The position of the bunches for different run periods is shown in figure 5.3. The inter-bunch time was 581 ns. The bunch width was about 7 ns in Monte Carlo and 15 ns in data.

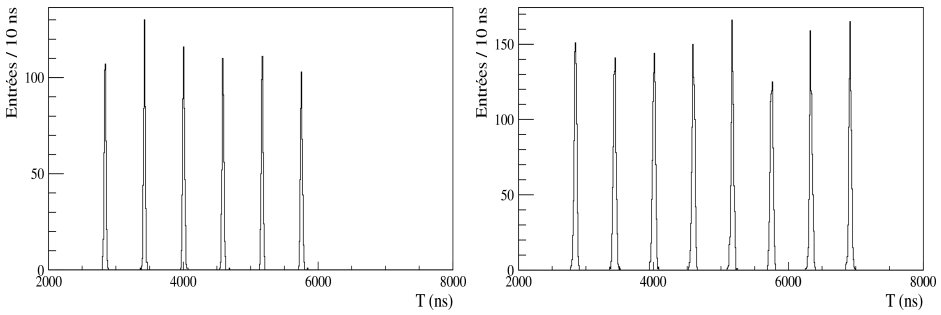

Figure 5.3: Timing position of the tracks with the structure in bunches clearly visible. The left plot shows data from run 1 with six bunches and the right one shows data from a later period with eight bunches.

The tracks whose timing position are less than 60 ns away from the mean bunch position (i.e. 4 times the bunch width in data) are classed together in the

same bunch. An event is defined as the set of tracks belonging to a single time bunch. The aim of this cut is first to supress accidental pile-up of interactions, as the neutrino interactions in two different bunches within the same beam spill are treated as separate events. The remaining probability to have at least two ν interactions in a single bunch is less than 1 %. The second purpose of the bunching cut is to remove external not beam-produced tracks, tracks coming from the interactions of neutrinos elsewhere or cosmics tracks.

5.2.1.2 Highest momentum negative track

The outgoing negatively charged muon, in true ν_μ charged current interactions, is most of the time the particle with the highest momentum among the negatively charged particles. So, we require at least one global track, with FGD and TPC components, corresponding to a negatively charged particle. Then we select the one that has the highest momentum among them. We call this track the lepton candidate.

It was checked whether the most energetic track in every event was a negative track. The answer is no. 73% of the most energetic tracks are negative tracks while 27% are positive tracks. That is why it is better to select the muon candidate not only as the highest momentum track but also as a track which corresponds to a negatively charged particle.

Charge misidentification can happen, as the charge is determined from the sign of the track curvature. Due to a failure in the reconstruction, a forward-going negative track is sometimes considered as a backward-going positive track and vice-versa (see subsection 5.2.1.5).

5.2.1.3 FGD fiducial volume

The vertex of neutrino interaction is defined as the begining of the selected track. We check if the start position of this track is inside the FGD fiducial volume(FGD FV) or not. In other words, we keep only the events where the the most energetic negative track starts in the FGD FV, in order to select the events where the neutrino interactions are inside the FGD FV.

The definition of the fiducial volume is carefully determined. The T2K Barcelona, Geneva and Valencia groups yielded the best values to define the fiducial volume, based on efficiency and purity optimisations. The optimisation study shows that the best fiducial volume cuts consist in excluding the first X-Y module of each FGD (the upstream z position cut, where the Z axis is defined to be parallel to the beam axis) and removing five bars on either end of each layer in the FGD in the transverse plane (x and y positions, where X is the drift axis and Y the vertical axis).

The fiducial volume contains therefore 14 XY modules in FGD1 and 6 XY modules in FGD2, in which the X and Y layers contain 182 scintillators bars. The fiducial volume cut in the FGD is given as:

- $|x(\text{cm})| < 88.0$ and $|y(\text{cm}) - 5.5| < 88.0$;
- $13.7 < z(\text{cm}) < 44.7$ (FGD1), $148.1 < z(\text{cm}) < 181.0$ (FGD2).

Requiring the fiducial volume cut allows to reduce substantially the background contributions. Emblematic backgrounds excluded by this cut are sand muons (muons which come from the natural radioactivity or from neutrino interactions with the surrounding rocks and sand) which cross the detectors, neutrino interactions in the detector walls, magnet, or other detectors, and cosmic rays.

5.2.1.4 TPC track length

The selection of an event in our case requires at least one reconstructed global track crossing the TPC, i.e. with at least one TPC segment. Typically, we will have a segment in TPC2 (and maybe in TPC3 also) for interactions in FGD1 and in TPC3 for interactions in FGD2. From the TPC segment of the track, all the information needed for a proper selection are available such as the momentum of the particle, the deposited energy per unit of length, and the result of the particle identification algorithms.

However, any simple TPC segment is not enough to ensure the quality of the track in order to determine with reliablity the reconstructed momentum and particle identification of the track. To achieve this purpose, we require a good

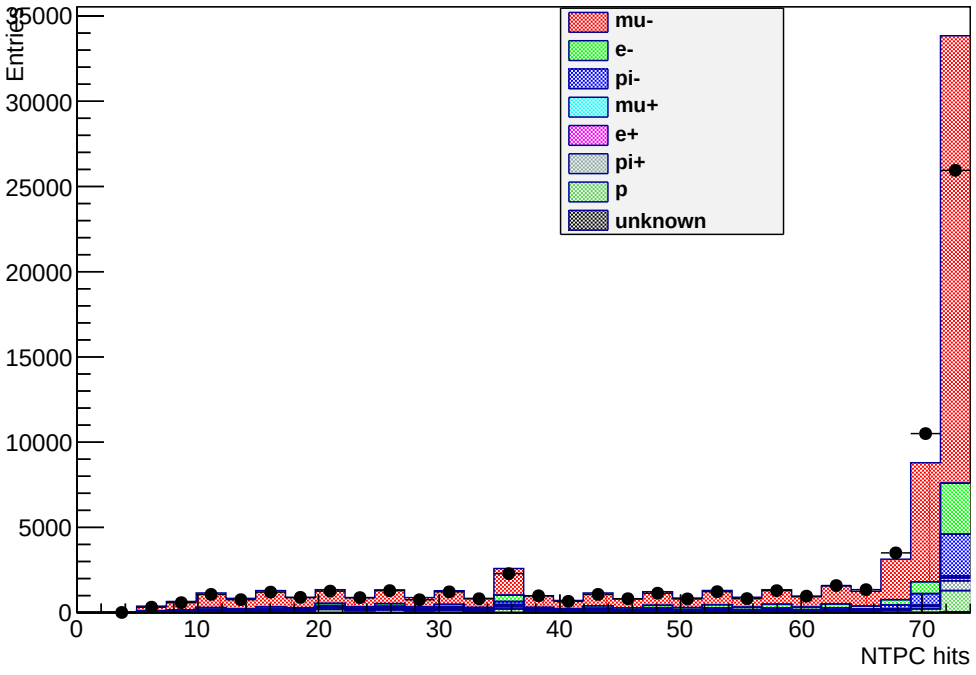

Figure 5.4: Distribution of the number of nodes for the muon candidate TPC segment. The points show the data while the colored histograms show the reweighted simulated data according to the true particle type of the μ candidate.

TPC segment, i.e a long enough TPC segment. For that, the track has to satisfy a requirement on the minimum number of points, knowing that each point corresponds to a cluster of Micromegas pads in the same column.

A single TPC has 72 pad columns, so a straight track crossing a single TPC should have at most 72 points, while a spiral one may have more. Figure 5.4 shows the track length distribution before cuting on it (according to the true particle type of the μ candidate for the NEUT simulated data), where two peaks can be observed: one at 72 points, which is the full TPC, and one at 36 points, which corresponds to one Micromegas module width, half of the TPC. In our selection, we keep only tracks that have more than 18 hits (one quarter of a TPC) and we reject short tracks. This cut is called the TPC track quality cut.

The choice of this particular value of the quality cut is based on studies of the kinematic bias for tracks of different length [56]. The track with 18 nodes or less are mostly low momentum tracks. About 93.4 % of the selected tracks have more than 18 nodes, so we don't lose too many events from this cut.

5.2.1.5 Backwards-going tracks and TPC veto

The goal of these cuts are to remove events with tracks entering the FGD fiducial volume from the upstream edge of the detector, for example events with an interaction taking place in the P0D or in the magnet coils with a secondary interaction in the FGD. These events produced outside the FGD are considered as a background to our selection.

First, we consider the difference on the z coordinate between the start and the end position of the muon candidates (highest-energetic negative tracks starting in the FGD fiducial volume). The event is rejected if the muon track candidate is backward-going, i.e. the end position is upstream of the start position. As we can observe in figure 5.5 showing this variable, the majority of muon candidates are forward-going tracks. By using this cut, we reject only 0.4 % of events.

Second, we check the events with more than one reconstructed track. We select the highest-energetic track with a TPC segment which is in the same time bunch and different from the muon candidate. We reject the event if the start position of the second track is more than 150 mm upstream from the starting

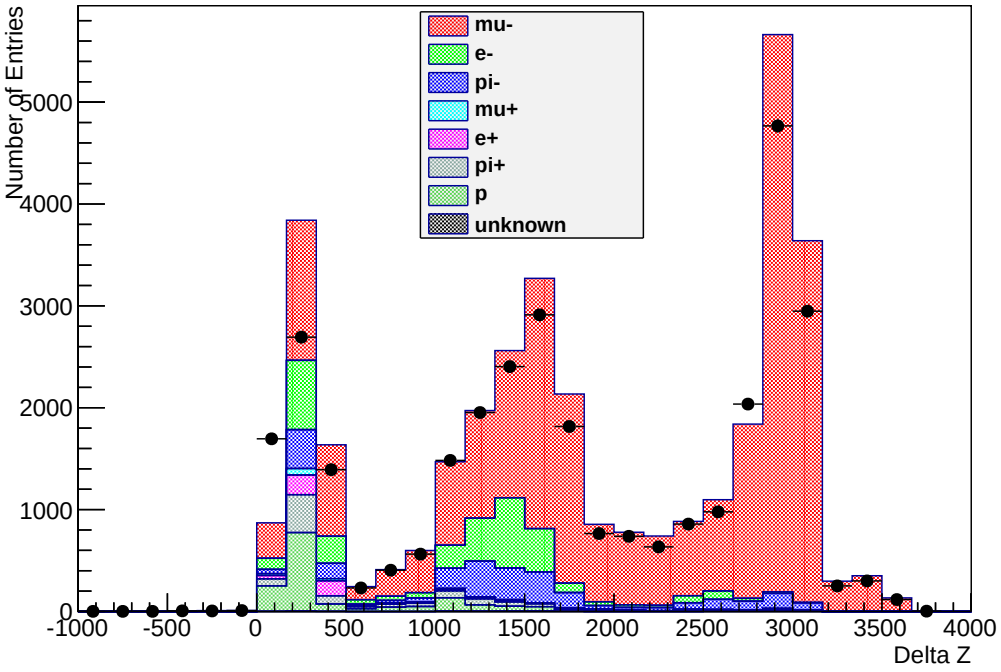

Figure 5.5: The delta z difference between the start and the end position of the muon candidate track. The points show the data while the colored histograms show the reweighted simulated data according to the true particle type of the μ candidate.

position of the muon track. This case means that there is a track in the event other than the muon track that probably entered the detector from the P0D or magnet region. Figure 5.6 shows the distribution of this variable (TPC Veto Delta Z).

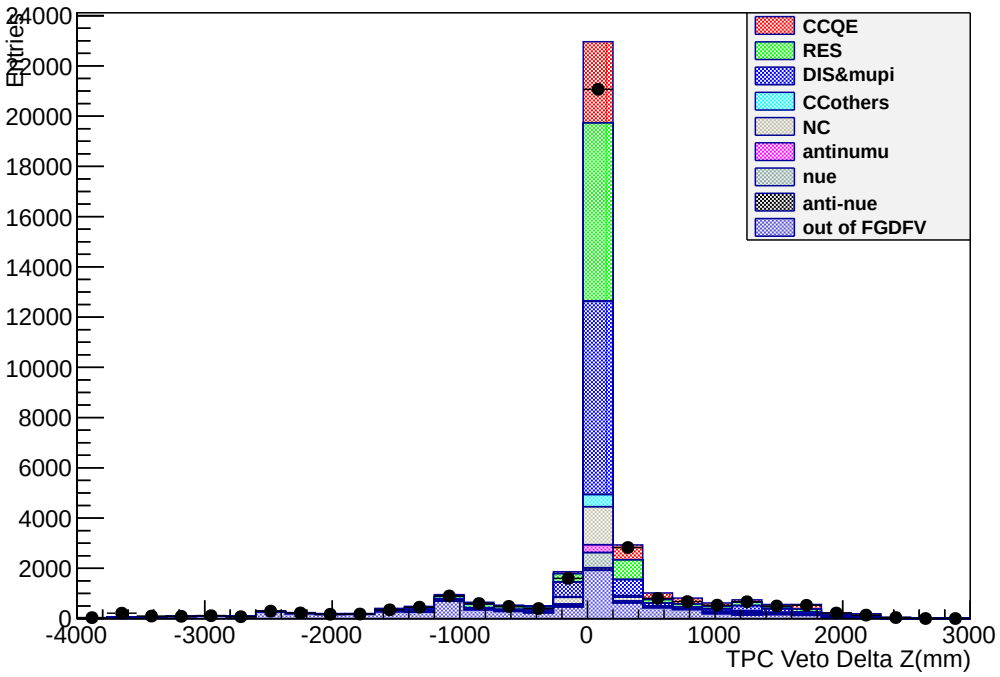

Figure 5.6: The delta z difference between the start of the muon track and the start of the highest-energetic track other than the muon candidate. The points show the data while the colored histograms show the reweighted simulated data according to the true neutrino interaction type.

5.2.1.6 TPC particle identification

An important element in the selection of a muon candidate is the particle identification (PID) with which we need to reject at best as possible electrons and protons. Our PID selection is based on the information coming from the TPC.

The distribution of the energy loss by ionisation as a function of the reconstructed momentum for the lepton candidate track is shown in figure 5.7. As we

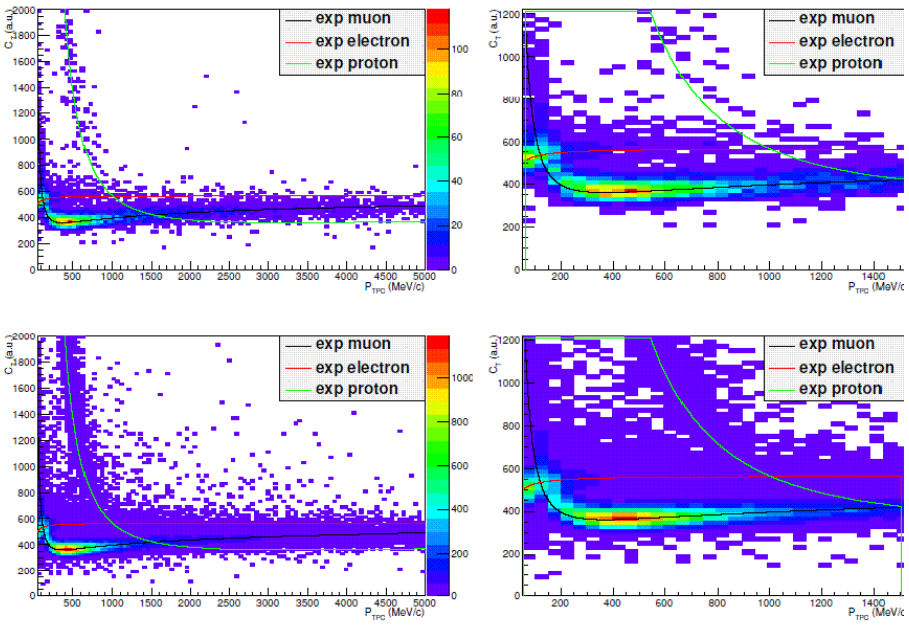

Figure 5.7: Distribution of the energy loss by ionisation in the TPC as a function of the TPC momentum for the lepton track starting in the FGD FV, with superimposed the expected curves for muons, electrons and protons in data (top) and MC (bottom) before the PID selection. The plots on the left show the full momentum range, while the plots on the right show a zoom for momenta smaller than 1.5 GeV/c (which corresponds to the energy range for the oscillation analysis).

can see from this figure, the majority of the tracks are compatible with a muon but we also see some electrons and some protons. Pions are too similar to muons to be separated from them. We use the pulls δ^i of the energy loss in the TPCs for each charged particle hypothesis i, where i can be a muon, proton, pion, kaon, or electron. The PID pull variable is defined as follows:

$$\delta^i = \frac{C_{meas} - C^i_{exp}}{\sigma_{meas}} \tag{5.1}$$

and represents the difference between the expected C^i_{exp} and measured C_{meas} truncated mean values of the deposited charge divided by the deposited energy resolution σ_{meas} for the different hypotheses on the particle type i. Further details can be found in [56]. Using the pull variables, we can enhance a given particle type, e.g. muon or electron.

In figure 5.8, we show the pull in the muon hypothesis before the PID selection cut is applied. Most of the selected tracks are compatible with the muon pull hypothesis. It can also be seen from these plots that the agreement between data and MC is fairly good.

In order to obtain a reasonable purity of muons candidates, we use the TPC pulls in two different hypotheses. First of all, the absolute value of the muon pull is used to make sure that our candidate track is compatible with the muon hypothesis. When requiring $\mid \delta^\mu \mid$ to be smaller than 2.5, the amount of tracks which are electrons or protons is greatly reduced by the muon pull cut, while the efficiency on muon tracks is higher than 97 %.

Figure 5.9 shows the pull in the electron hypothesis before and after a muon pull selection cut ($\mid \delta^\mu \mid < 2.5$) is applied. Many electrons have already been rejected by this cut, but a background of electron tracks still remains. Tracks that are consistent with the electron hypothesis can be rejected. For this we require the absolute value of the electron pull to be greater than two ($\mid \delta^e \mid > 2$). The electron pull cut further improves the low momentum electron rejection.

Combining the TPC muon and electron pull cuts, the selection corresponds to a 87.0 % efficiency in selecting muons and a 88.2 % efficiency in selecting muons from ν_μ interactions. However, for high momentum tracks, the efficiency decreases significantly, as shown in figure 5.10, separately for charged current deep inelastic

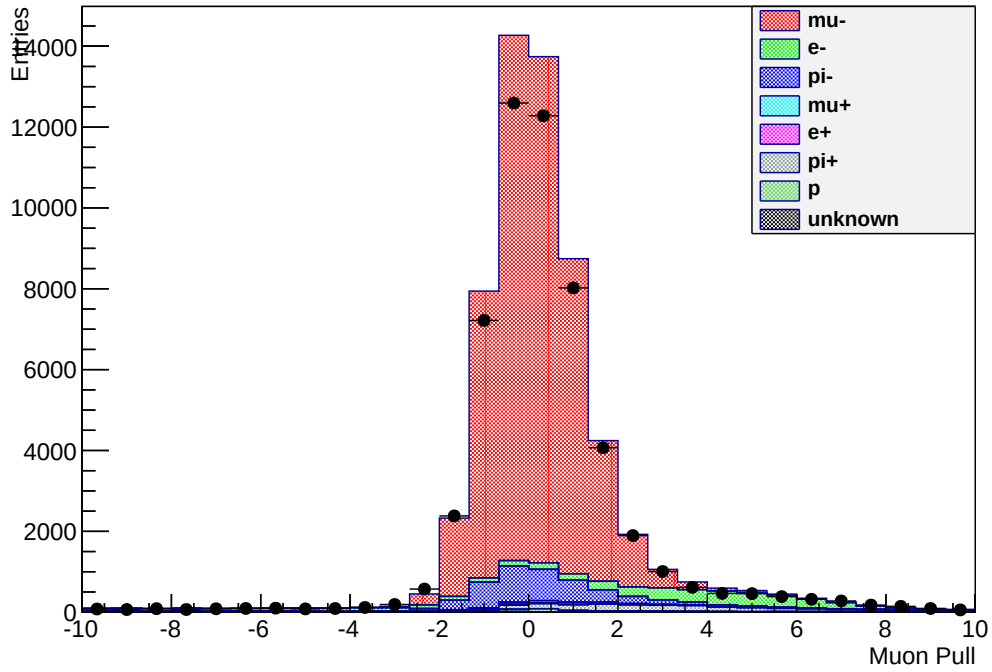

Figure 5.8: PID pull for the muon hypothesis for negative tracks starting in the FGD FV before PID selection. The points show the data while the colored histograms show the reweighted simulated data according to the true particle type of the μ candidate.

$\mid \delta^{\mu} \mid < 2.5$ or $\mid \delta^{e} \mid > 2$					
	Before cut		After cut		Efficiency
particle type	number	fraction (%)	number	fraction (%)	(%)
μ^-	276795	78.27	273838	83.80	98.93
e^-	24759	7.00	7438	2.28	30.04
π^-	21484	6.08	20396	6.24	94.94
p	15965	4.51	15738	4.82	98.58
μ^+	1996	0.56	1586	0.49	79.46
e^+	3997	1.13	765	0.23	19.14
π^+	8567	2.42	6651	2.04	77.64
unknown	374	0.11	345	0.11	92.25
Total	353637	100.0	326757	100.0	92.40

Table 5.2: Effect of the PID cut based on the muon pull and the electron pull.

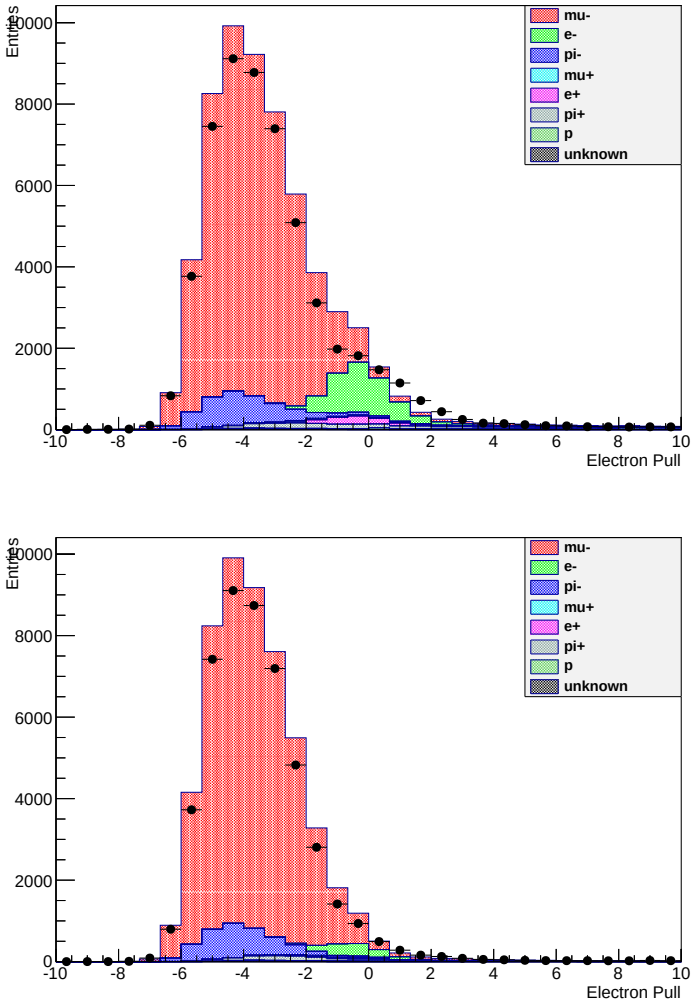

Figure 5.9: PID pull for the electron hypothesis for negative tracks starting in the FGD FV (top) before PID selection and (bottom) after the muon pull cut. The points show the data while the colored histograms show the reweighted simulated data according to the true particle type of the μ candidate.

scattering (CCDIS), charged current resonant (CCRES), charged current quasi-elastic (CCQE), and neutral current (NC) neutrino interactions. This is because at high momentum the expected dE/dx values for muons and electrons tend to get closer to each other and so many tracks cannot satisfy both the requirements on δ^{μ} and δ^{e}, causing the efficiency to decrease. This is a substantial problem for our analysis on CCDIS cross section measurements, since many interesting events are at high momentum.

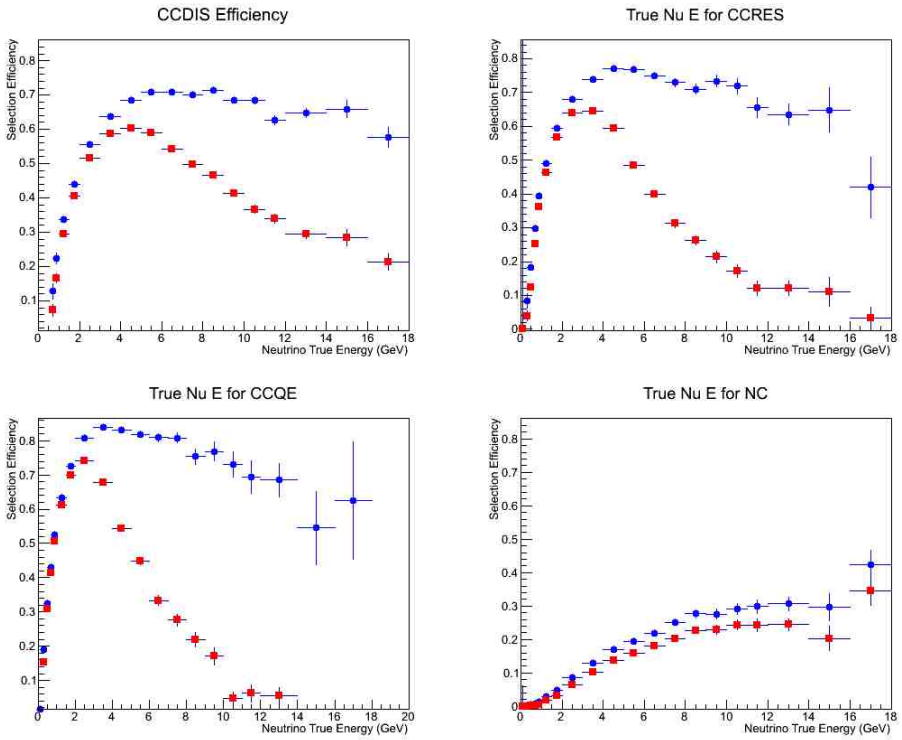

Figure 5.10: Efficiency of the global selection on charged current ν_{μ} interactions for (top left) CCDIS, (top right) CCRES, (bottom left) CCQE, and (bottom right) NC. The blue points is for our nominal selection, while the red points is for a stricter PID selection when applying both the muon pull cut and the electron pull cut.

That is why in our final selection, we do noy apply the AND of the muon pull cut and electron pull cut, but the OR of these two cuts. The effect of the PID selection is shown in table 5.2 according to the various true particle types of the μ candidate. It has been checked that the fit described in chapter 6 gives better

results for the latter configuration than for the former one. Though we lose on purity, we maintain a better efficiency.

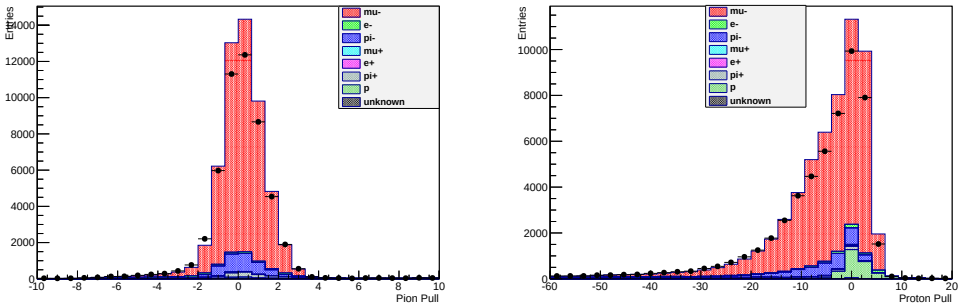

Figure 5.11: PID pull for the (right) pion and the (left) proton hypothesis for negative tracks starting in the FGD FV after the PID cut.

We check the distribution of the pion and the proton pulls after the cut on the PID in figure 5.11. The pions are too similar to the muons to be rejected, while the protons behave quite differently. In the future, the PID selection can certainly be made more cleverly to reach a high purity without losing too much efficiency in the high momentum region.

5.2.2 Summary of the muon selection

All the cuts above taken together define the selection of inclusive charged current ν_μ interactions in the FGD fiducial volume. The events surviving these cuts are included in the final data sample for further analysis described in the following chapters. The effect of the selection in summarised in subsection 5.2.2.1. The composition of the selected sample is studied in subsection 5.2.2.2.

5.2.2.1 Effect of the muon selection

Table 5.3 shows the number of selected events in the data and in the simulated samples using the two generators of neutrino interactions NEUT and GENIE, after each successive cut. Table 5.4 gives the corresponding efficiencies. The simulated samples generated with the NEUT and GENIE generators give very similar results. They are also consistent with the data, except for the first cut

requiring the track to originate from the FGD fiducial volume. This is because there are a lot of sand muons in the data before this cut, which are not simulated and thus are not present in the Monte Carlo.

Reduction table					
	NEUT		GENIE		Data
Cut	Non norma.	normalised	Non norma.	normalised	
Negative track	5578208	839237	4893682	761470	1488983
Track in FGD FV	411869	61945	379850	59105	66113
Good track quality	384660	57853	355393	55299	61722
Forward track	383460	57672	354321	55132	61490
Upstream veto	360657	54243	333593	51907	57110
PID cut	326757	49144	300591	46772	51869

Table 5.3: The number of selected events for the different cuts as predicted by NEUT and GENIE generators compared to data. The MC numbers are normalised to the number of POT in the data using the normalisation factors R(Data/NEUT)= 0.1504 and R(Data/GENIE)= 0.1556.

Reduction of each cut			
	MC NEUT	MC Genie	Data
Track in FGD FV	7.38%	7.76%	4.44%
Good track quality	93.39%	93.56%	93.36%
Forward track	99.69%	99.70%	99.62%
Upstream veto	94.05%	94.15%	92.88%
PID cut	90.60%	90.11%	90.82%

Table 5.4: Reduction factor for each individual cut in data and Monte Carlo.

In table 5.5, the resulting efficiency and purity on inclusive charged current ν_μ interaction in FGD FV (our signal SG) are shown for each cut. The efficiency is computed as the ratio between the number of selected signal events over the number of generated signal events. The efficiency for different neutrino interactions is presented in figure 5.12. The purity is defined as the fraction of signal events in the selected sample. The increase of purity after the PID cut is due to the PID discriminating ability to separate muons from the low momentum electrons.

NEUT				
Cut	N. events	N.SG	$\varepsilon(\%)$	$\eta(\%)$
Good negative track in FV	384660	288184	55.96	74.92
Upstream veto	360657	278992	54.17	77.36
PID cut	326757	273712	53.15	83.77
GENIE				
Cut	N. events	N.SG	$\varepsilon(\%)$	$\eta(\%)$
Good negative track in FV	355393	261520	56.93	73.59
Upstream veto	333593	254107	55.37	76.17
PID cut	300591	249518	54.37	83.01

Table 5.5: The CC ν_μ interaction efficiency, ε, and purity, η, estimated with the MC simulation. The number of generated signal events is 515012 in NEUT and 458940 in GENIE.

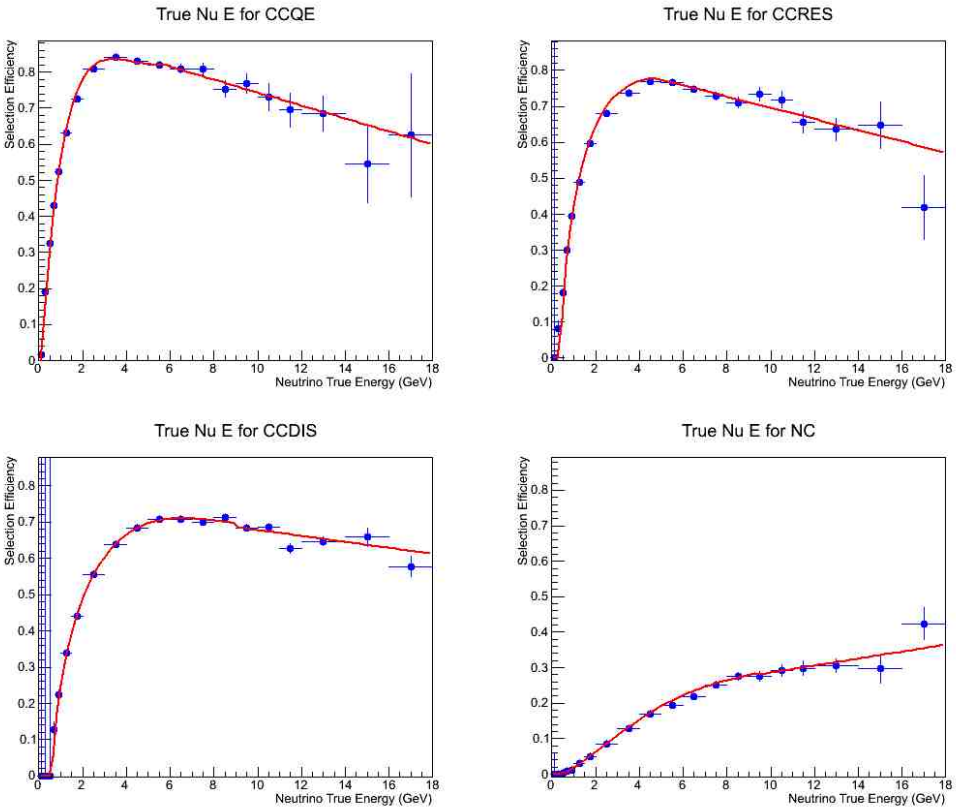

Figure 5.12: The efficiencies for the different interaction types: (top left) CCQE, (top right) CCRES, (bottom left) CCDIS, and (bottom right) NC.

5.2.2.2 Composition of the selected sample

In Table 5.6 we show the composition of the sample in terms of the true type of the particle selected as the muon candidate after the final selection, according to the NEUT Monte Carlo. Signal (SG) is defined as a true charged current ν_μ interactions in the FGD fiducial volume, while background (BG) contains all other interactions. Similarly, table 5.7 gives the true type of the true parent of the muon candidate. At the end of the selection, the muon candidate in the selected sample is correctly identified in 83.8 % of the cases and is a direct production of the ν interaction in 94.9 % of the cases. Almost all selected candidates which are true muons (99.7 %) come directly from the neutrino interaction. This is also the case for most pions and protons. Antimuons are shared about equally between the ones coming from antineutrino interactions and the ones coming from pion decays. Finally electrons and positrons come mainly from photon conversion.

	Selected sample		SG		BG	
	number	f(%)	number	f(%)	number	f(%)
μ^-	273838	83.80	264010	96.46	9828	18.53
π^-	20396	6.24	6011	2.20	14385	27.12
e^-	7438	2.28	1080	0.39	6358	11.99
e^+	765	0.23	74	0.03	691	1.30
μ^+	1586	0.49	58	0.02	1528	2.88
π^+	6651	2.04	587	0.21	6064	11.43
p	15538	4.76	1688	0.62	13850	26.11
others	545	0.17	204	0.07	341	0.64
total particle	326757	100	273712	100	53045	100

Table 5.6: The composition of the final selected sample in terms of true particle type of the μ candidate and the corresponding fractions, f, from the NEUT Monte Carlo.

The momentum and cosine of the polar angle of the muon candidate are important variables since they are used to reconstruct the neutrino energy (see section 1.3.2.1). The momentum distribution of the muon candidate is shown according to the true neutrino interaction type in figure 5.13 and to the true particle nature of the muon candidate in figure 5.14. Similar plots for the signal only (ν_μ charged current interactions in the FGD FV) are shown according to the

	Selected sample		SG		BG	
	number	$f(\%)$	number	$f(\%)$	number	$f(\%)$
ν	310197	94.93	271544	99.21	38653	72.87
π^-	3389	1.04	531	0.19	2858	5.39
π^+	4781	1.46	324	0.12	4457	8.40
p	1581	0.48	179	0.07	1402	2.64
γ	6486	1.98	974	0.36	5512	10.39
others	323	0.10	165	0.06	158	0.30
total particle	326757	100	273712	100	53045	100

Table 5.7: The composition of the final selected sample in terms of the true parent type of the muon candidate and the corresponding fractions, f, from the NEUT Monte Carlo.

true neutrino interaction type in figure 5.15 and to the true particle nature of the muon candidate in figure 5.16. Finally for the background only, these plots are shown according to the true neutrino interaction type in figure 5.17 and to the true particle nature of the muon candidate in figure 5.18. The agreement between data and Monte Carlo, though not perfect, is reasonable. The background is more important in the low momentum region. It is due mainly to particles other than muons: π^+ and electrons at very low momentum, protons between 0.4 and 1 GeV/c and π^- over the whole momentum range.

The angular distribution is shown for the cosine of the muon polar angle with respect to the neutrino beam direction according to the true neutrino interaction type in figure 5.20 and to true particle nature of the muon candidate in figure 5.19. The correlation between the momentum and cosine of the polar angle of the muon candidate for the events selected in the NEUT MC is illustrated figure 5.21.

The signal and the various backgrounds in the selected sample are shown in table 5.8. The main background comes from the interactions outside the FGD.

5.2.3 Two topologies for the muon selection

Our goal is to study the CCDIS events. The inclusive charged current selected sample is divided into two topologies: the topology with a high multiplicity of tracks (at least three) topologie 1 and the topology with at maximum two reconstructed tracks topologie 2. This division is aimed for a separation between

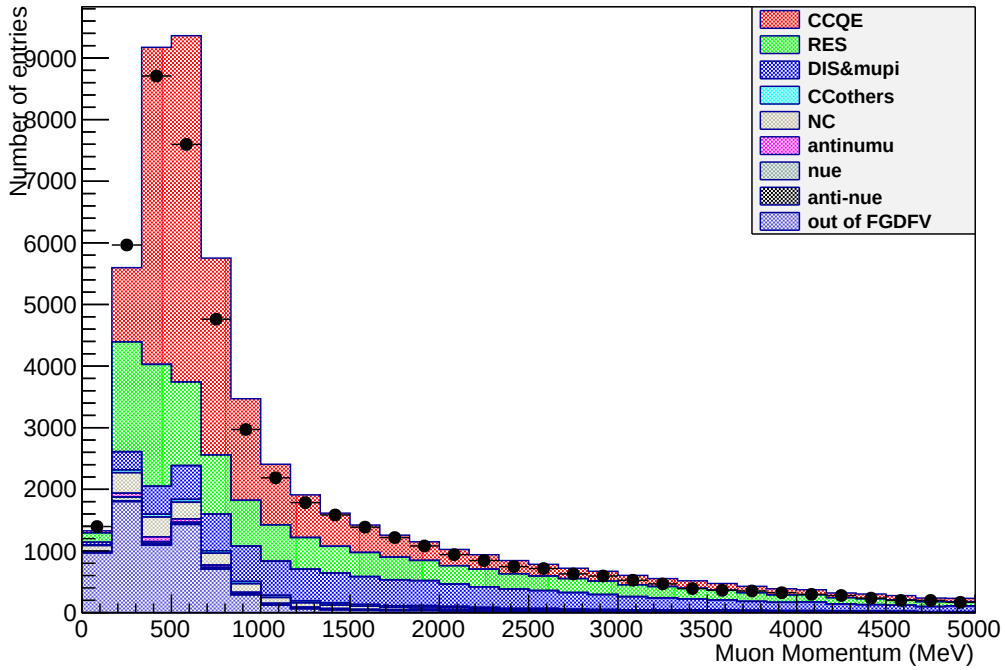

Figure 5.13: The momentum distribution of the muon candidate for the selected events. The points show the data while the colored histograms show the reweighted simulated data according to the true neutrino interaction type.

Neutrino interaction type				
	NEUT		GENIE	
neutrino interaction type	number	fraction %	number	fraction %
out of FGD	36353	11.13%	33307	11.08%
in FGD out of FV	1646	0.50%	1711	0.57%
$\overline{\nu}_e$ in FGD FV	211	0.06%	183	0.06%
ν_e in FGD FV	2107	0.64%	1885	0.63%
$\overline{\nu}_\mu$ in FGD FV	2177	0.67%	2072	0.69%
$NC\ \nu_\mu$ in FGD FV	10551	3.23%	11145	3.71%
$CC\ \nu_\mu$ in FGD FV	273712	83.77%	250288	83.27%
Total	326757	100%	300591	100%

Table 5.8: Composition of CC inclusive selected sample according to the NEUT and GENIE MC generators.

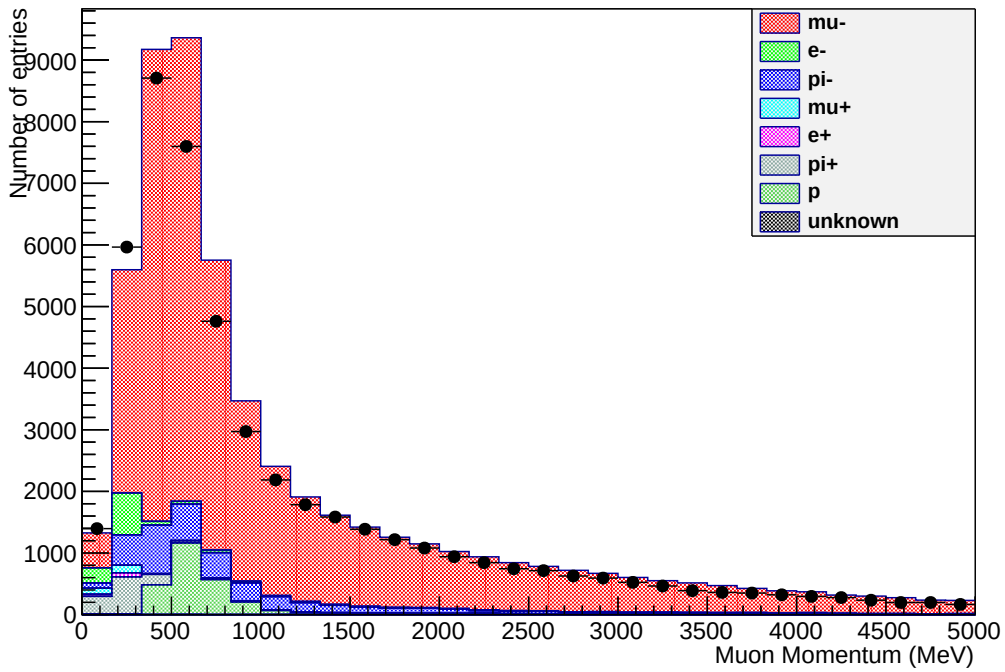

Figure 5.14: The momentum distribution of the muon candidate for the selected events. The points show the data while the colored histograms show the reweighted simulated data according to the true particle type of the μ candidate.

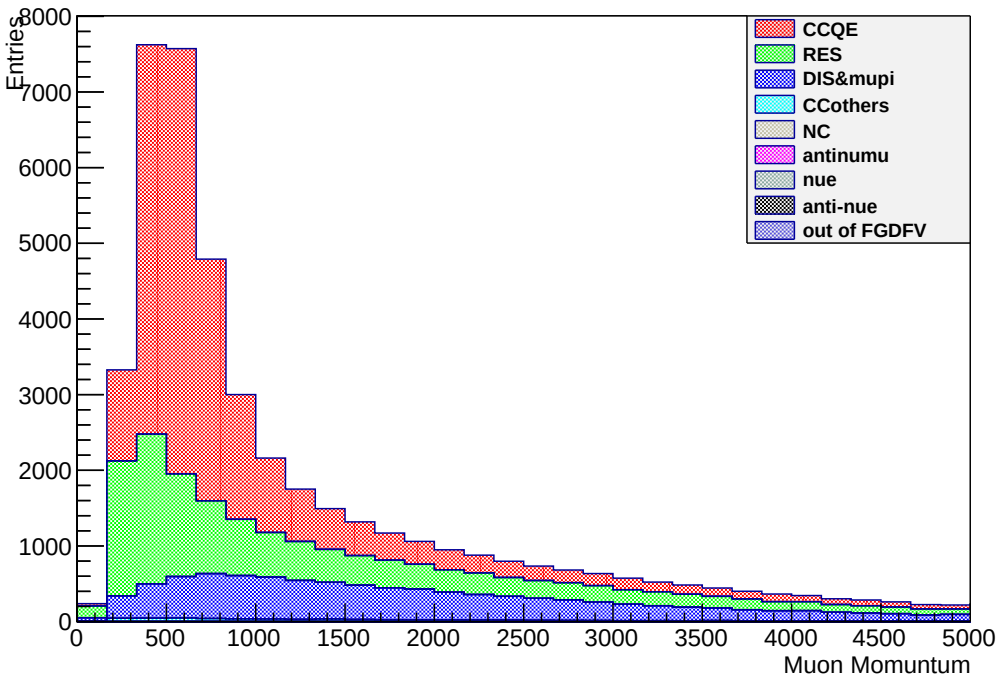

Figure 5.15: The momentum distribution of the muon candidate for the selected events in the MC for the signal only. The colored histograms show the reweighted simulated data according to the true neutrino interaction type.

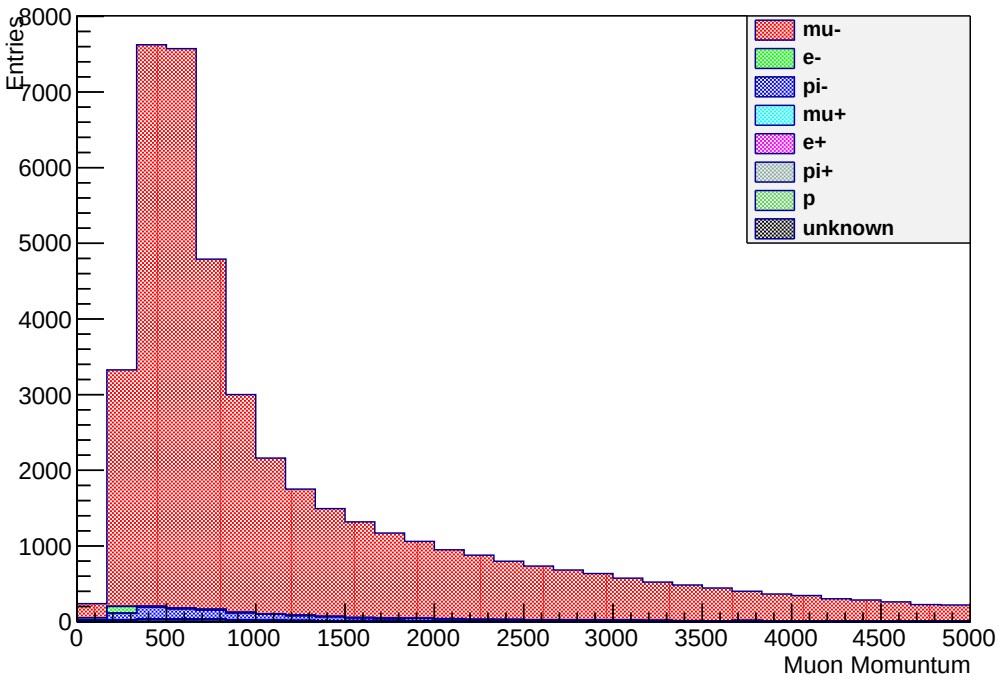

Figure 5.16: The momentum distribution of the muon candidate for the selected events in the MC for the signal only. The colored histograms show the reweighted simulated data according to the true particle type of the μ candidate.

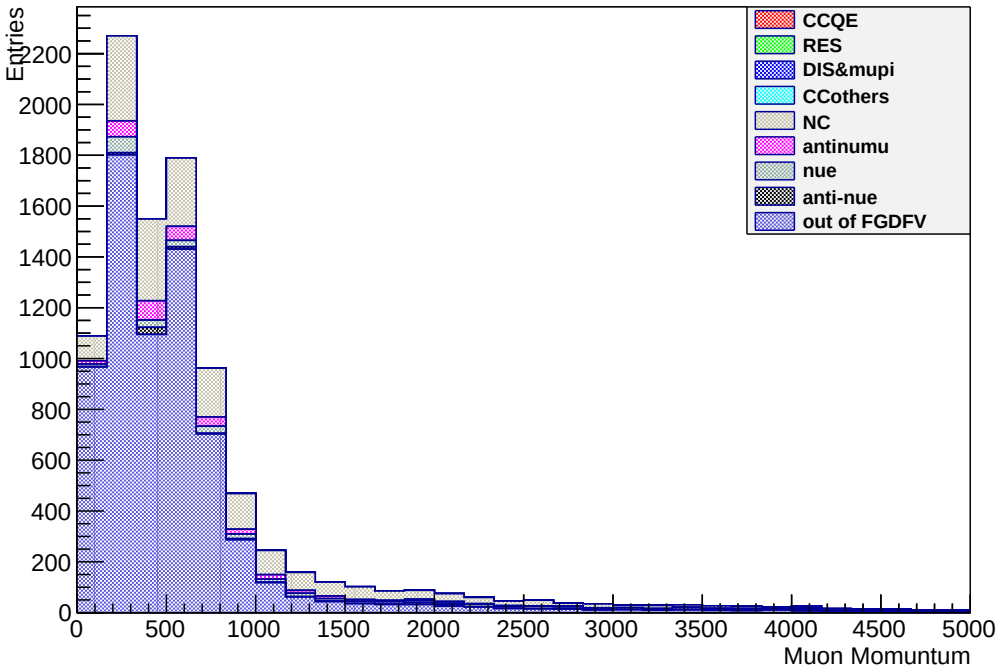

Figure 5.17: The momentum distribution of the muon candidate for the selected events in the MC for the background only. The colored histograms show the reweighted simulated data according to the true neutrino interaction type.

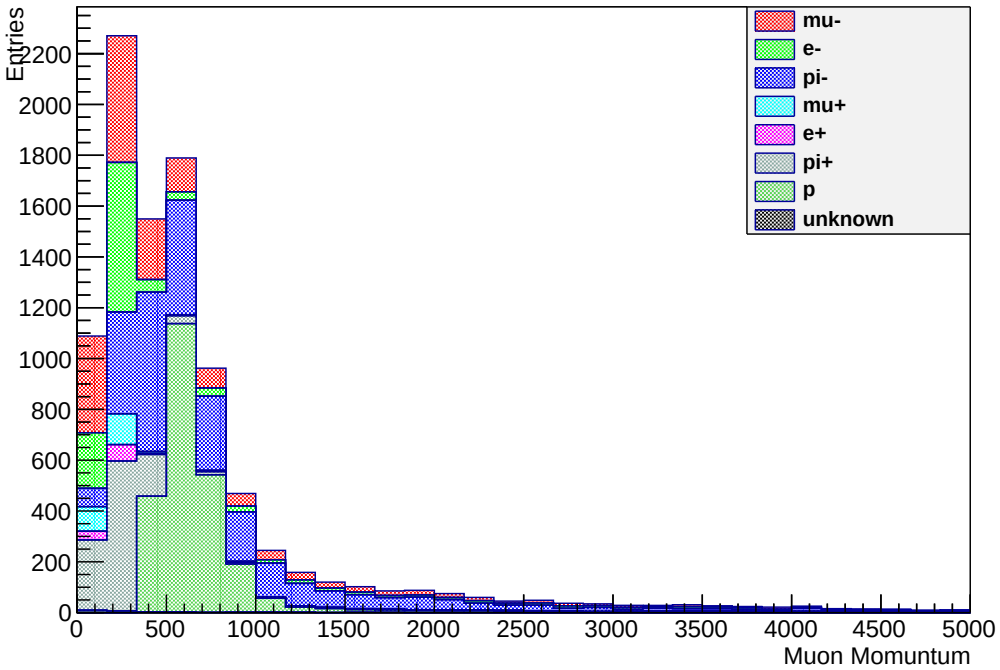

Figure 5.18: The momentum distribution of the muon candidate for the selected events in the MC for the background only. The colored histograms show the reweighted simulated data according to the true particle type of the μ candidate.

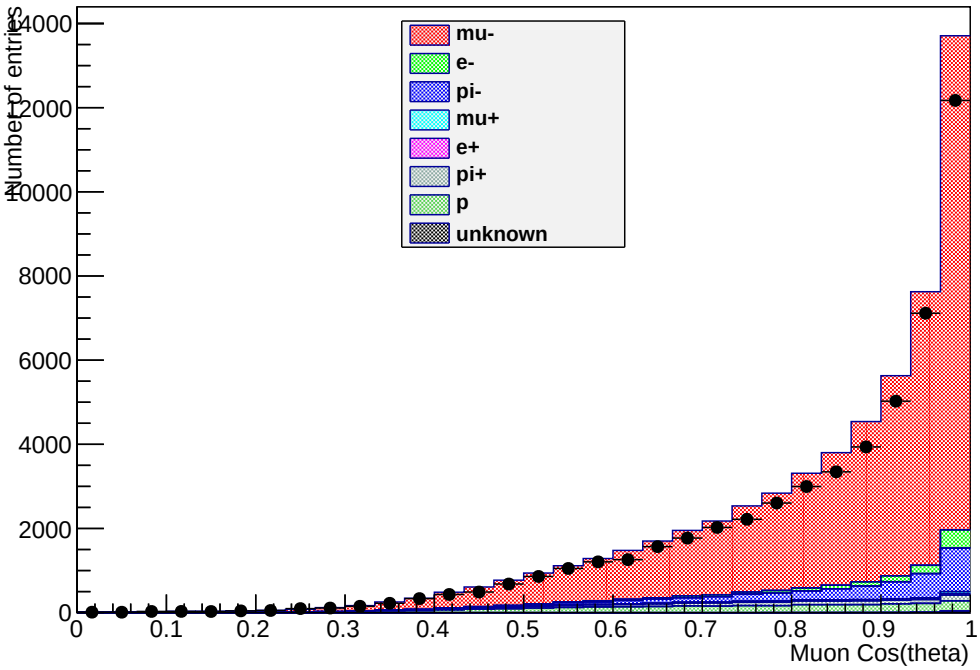

Figure 5.19: The cos theta distribution of the muon candidate for the selected events. The points show the data while the colored histograms show the reweighted simulated data according to the true particle type of the μ candidate.

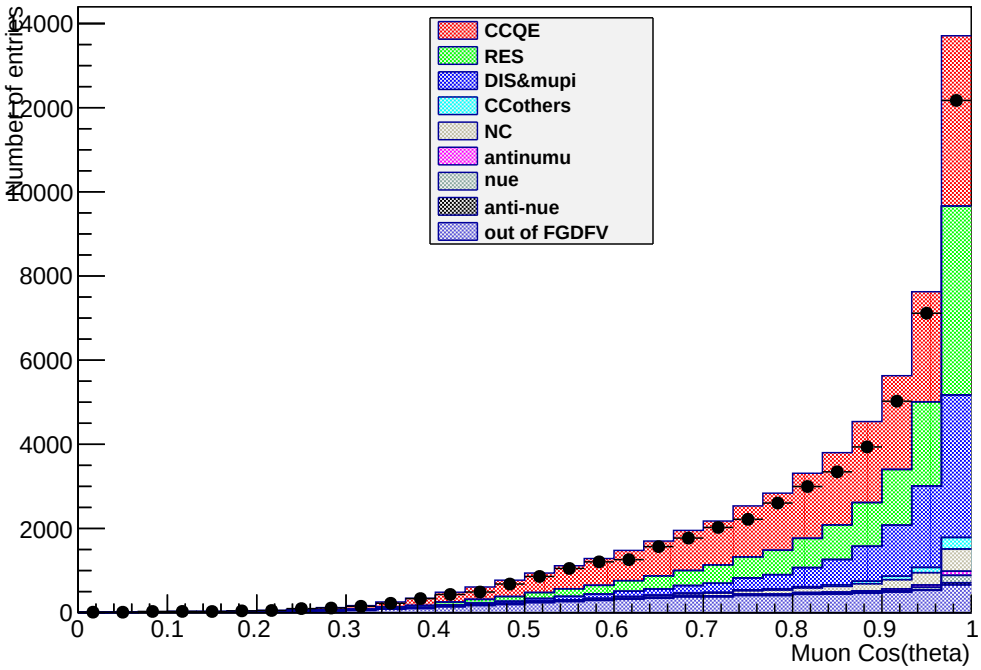

Figure 5.20: The cos theta distribution of the muon candidate for the selected events. The points show the data while the colored histograms show the reweighted simulated data according to the true neutrino interaction type.

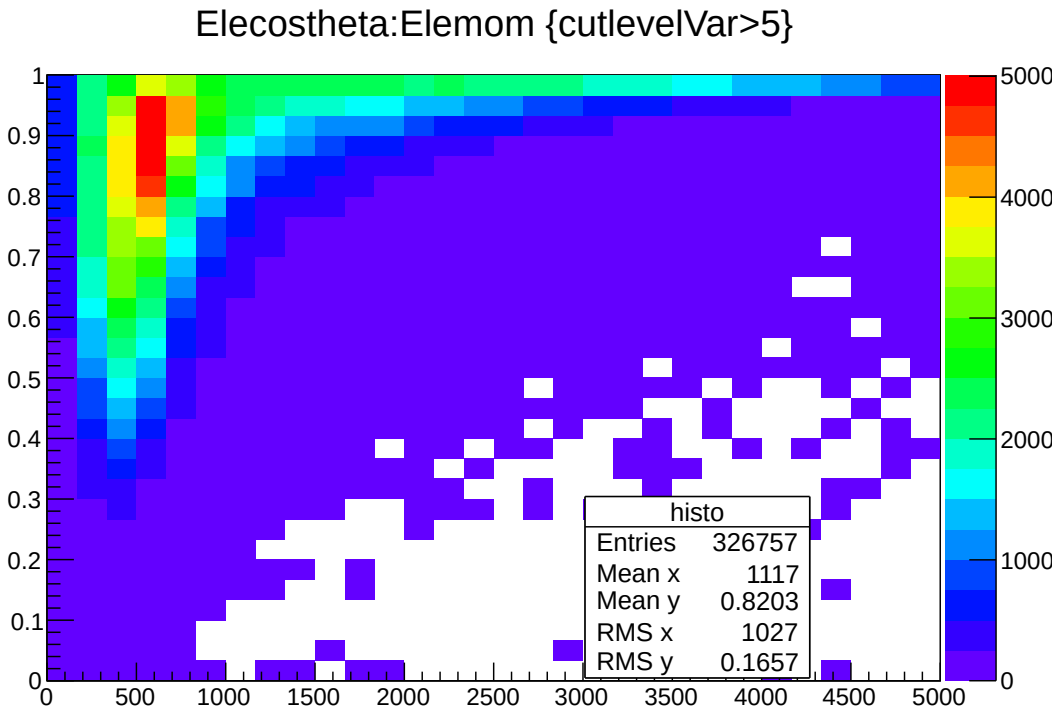

Figure 5.21: The space phase distribution of the muon candidate for the selected events in the MC. The cosine of the polar angle is plotted as a function of the momentum (in MeV).

CCDIS events in the former topology and CCQE events in the latter. In figure 5.22, we show the momentum distribution of the muon candidate for the events of topology 2. We observe that the momentum spectra is harder for topology 2 than for all selected events.

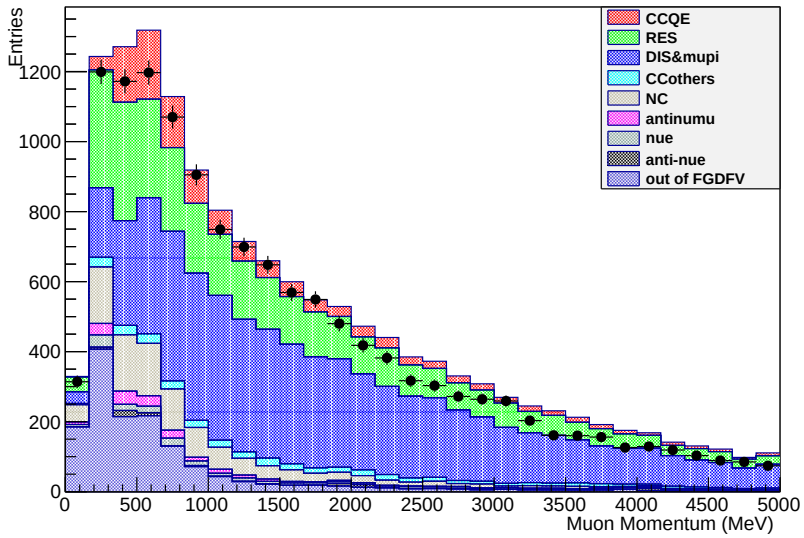

Figure 5.22: The momentum distribution of the muon candidate for topology 2. The points show the data while the colored histograms show the reweighted simulated data according to the true neutrino interaction type.

The MC composition at the generation level is given in the second column of table 5.9 as a function of the type of neutrino interactions. The composition of the MC inclusive ν_μ sample, after the CC inclusive selection, is shown in the third column of table 5.9. In the fourth and fifth columns of table 5.9, we show the different neutrino interaction types in the topology with low track multiplicity and in the topology with many tracks.

The CCDIS interactions represent 10 % of the neutrino interactions at generation level, 20 % at selection level. By the separation into two topologies, the CCDIS component is enriched in the topology with many tracks. The CCDIS interactions represent 50 % of the topology 2 sample, where the main background comes from CCRES. In the topology 1 sample, the dominant process is CCQE.

Interactions in FGD FV				
ν interaction type	Generation	Selection	Sel topo1	Sel topo 2
CCDIS	77820	53419	14445	38974
CCQE	283567	137831	130482	7349
$CC1\pi^0$	25012	12975	8823	4152
$CC1\pi^+(\nu + p)$	87954	42016	30976	11040
$CC1\pi^+(\nu + n)$	25992	14229	9793	4436
NC	209469	10551	4685	5866
$\nu_\mu + {}^{16}_{8}\mathrm{O}$	12483	9270	7817	1453
$\nu_\mu + n \rightarrow \mu + p + \gamma$	115	59	43	16
$\nu_\mu + n \rightarrow \mu + p + \eta$	4771	3289	1424	1865
$\nu_\mu + n \rightarrow \mu + \Lambda + K$	839	624	133	491
all ν_μ	728022	284263	208621	75642
all $\overline{\nu}_\mu$	20991	2177	1029	1148
all ν_e	13726	2107	742	1365
all $\overline{\nu}_e$	1363	211	61	150

Table 5.9: Composition of neutrino interactions in the FGD FV as a function of the neutrino interaction type at the generation level, at the inclusive selection level, and for the two topologies (NEUT Monte Carlo).

5.3 Electron or positron

As neutrino interactions with π^0 production are one of the main backgrounds for the neutrino oscillation analysis, it is interesting to measure the cross section of such interactions. This section is a preliminary study of a selection towards these events. For this π^0 analysis, only the selection is presented in this thesis. Subsection 5.3.1 present the strategy of this study. The details of the selection is given in subsection 5.3.2. The selected sample is described in subsection 5.3.3. Finally a division by topologies is discussed in subsection 5.3.4.

5.3.1 Strategy

Our signal here (in this section only) is the interaction of a neutrino under charge current interaction in the FGD FV with at least one neutral pion directly coming from the neutrino interaction vertex $\nu_\mu + n \rightarrow \mu^- + p + \pi^0 + X$. We call this signal the inclusive charged current neutrino interaction with at least one neutral

pion $CC\pi^0 X$, where X can contain any particle: pion, kaon, electron, ...

The neutral pion π^0 is very unstable. Its mean path is 25 nm. Then it is impossible to detect it directly. We are resorting to detect its decay particles. The decay of π^0 into two photons ($\pi^0 \rightarrow \gamma\gamma$) is the main decay channel. The fraction of this decay mode is 98 %. One of these photons may interact with the dense material of the FGD and convert into an electron and a positron ($\gamma \rightarrow e^+e^-$), which cross the TPC downstream the FGD. The sketch of the signal is illustrated in the figure 5.23.

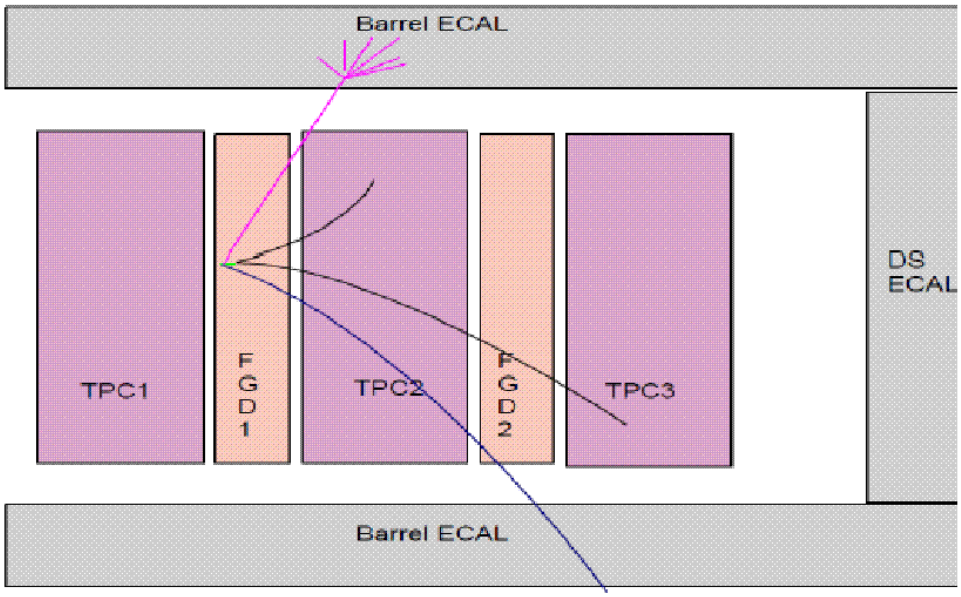

Figure 5.23: The sketch of a signal event. At the neutrino interaction point in FGD1, a muon (track in TPC2) is produced, as well as a π^0, which decays into two photons. The first γ gives a shower in the ECAL, while the second γ converts in FGD1 (displaced vertex) into an electron and a positron (tracks with opposite curvature in TPC2).

We want to select charged current neutrino interactions producing at least one neutral pion using the ND280 tracker. In order to tag this signal, we require the detection of a muon, which signs the charged current neutrino interaction,

and of an electron or a positron, which signs the production of a π^0. Note that we decided to require one electron or one positron, but we did not demand both to be detected. This choice is made in order to keep enough statistics for the analysis and to measure the cross-section with maximal efficiency.

Does the electron or the positron selected this way correpond to the second highest momentum track in the event after the muon candidate ? The answer in given in figure 5.24. The second highest momentum track in the event is mainly a proton. It is an electron or a positron in only 15 % of the cases.

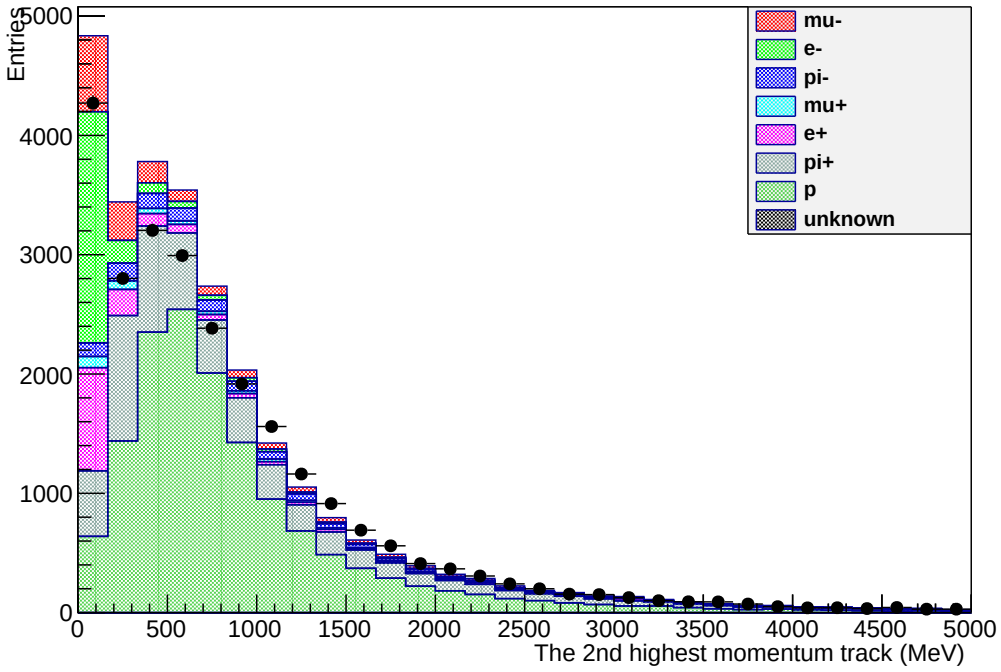

Figure 5.24: The true nature of the second highest momentum track in the event. The points show the data while the colored histograms show the reweighted simulated data according to the true particle type of this track.

In figure 5.25, we show the number of electrons or positrons in the inclusive CC sample, once a muon track is selected. The majority of neutrino interactions do not produce a detected electron or positron in the final state. If both photons from the π^0 decay converted into electron-positron pairs, we would expect 2 electrons and 2 positrons. But we see that by selecting 2 electrons and 2 positrons, we

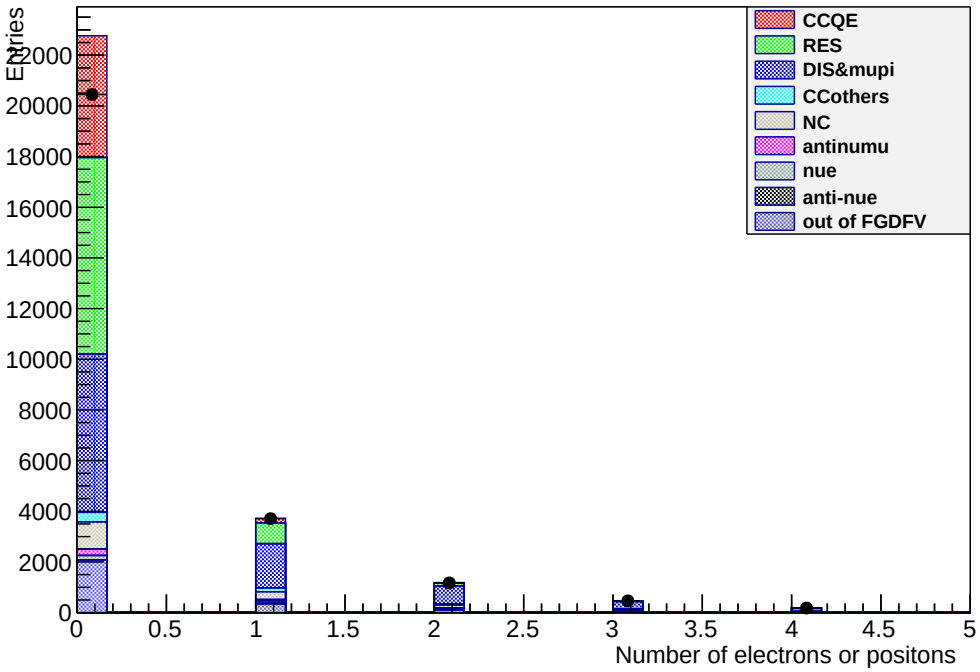

Figure 5.25: The number of electrons or positrons in the inclusive CC sample. The points show the data while the colored histograms show the reweighted simulated data according to the true neutrino interaction type.

have a very low efficiency. So we tag only one photon conversion by detecting one electron or one positron in a neutrino interaction.

5.3.2 The selection of an electron or positron

Once the muon track is selected in an event, then we search for an electron or positron track. In this section, we describe the selection of the electron or the positron which is done under the following order.

1. We look for a global track with a TPC component, i.e. crossing at least one of the three TPCs.

2. This track has to satisfy the bunch condition (the timing of the track is within the width of the bunch, 60 ns). After all the cuts, the muon and the electron or positron timing are shown in figure 5.26. The two tracks are well in the same bunch timing.

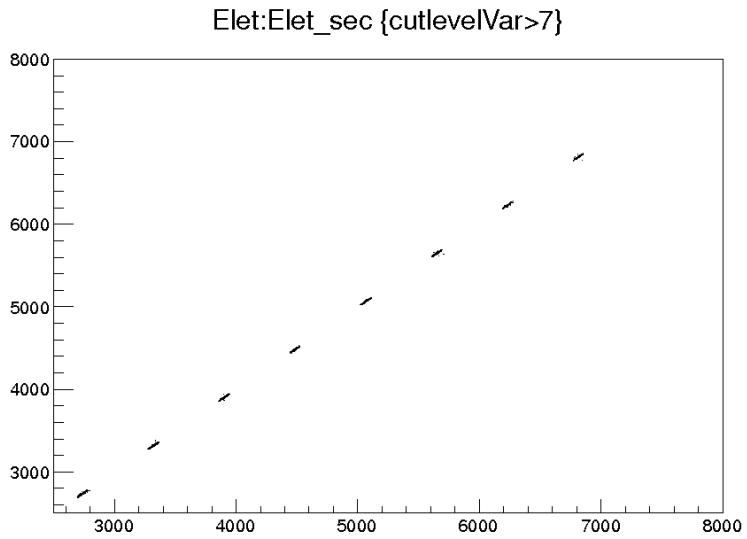

Figure 5.26: The timing of the muon versus the electron or the positron one after all the cuts.

3. The track looked for must be different from the muon track selected first.

4. Tracks with a momentum smaller than 50 MeV/c are rejected. This requirement is applied in order to identify the particle with enough reliability. (Tracks with less than 50 MeV/c are short tracks in the TPC, so bad quality tracks).

5. In addition to the previous cut, there is another cut on the track quality in the TPC. The selected tracks must have at least 36 TPC clusters.

6. Tracks without an FGD segment are rejected. The FGD gives the timing of the tracks.

7. We identify the electron or the positron using the PID pull defined in the TPC. The electron or the positron track candidates are kept if the absolute value of the pull under the electron hyposthesis is smaller than 2. In order to reject the contamination of the proton tracks, if the charge of the track candidate is positive and its momentum larger than 800 MeV, we reject the remaining tracks with a pull under the proton hypothesis smaller that 2. This last cut is mainly to reject misidentifed positrons that can look like a proton. In figure 5.7, we see that the electron and the proton curves in the dE/dx versus momentum plots cross around 800 MeV and are overlapping at high momentum.

8. Once the electron or positron tracks are chosen following the cuts above, if there remain several electron or positron candidates, we select the most energetic one.

9. Its momentum could be required to be smaller than 1 GeV, as the contamination with protons is dominant above that energy.

5.3.3 Summary of the electron or positron selection

The reduction table of the electron or positron selection is given in table 5.10. The reduction of the main cuts is shown in table 5.11.

Our signal is the ν_μ CC interactions in FGD FV with at least one π^0 in the final state, which comes from the vertex of the neutrino interaction. (In

Reduction table					
	NEUT		GENIE		Data
Cut	Non norma.	normalised	Non norma.	normalised	
Inclusive	326757	49144	300591	46772	51869
2nd track	156636	23558	146426	22784	26134
e^+/e^-	30015	4514	29120	4531	5684

Table 5.10: The number of selected events in the electron or positron selection as predicted by NEUT and GENIE generators compared to data. The MC numbers are normalised to the number of POT in the data using the normalisation factors R(Data/NEUT)= 0.1504 and R(Data/GENIE)= 0.1556. Note that the Monte Carlo reweighting has not been applied.

Reduction efficiency			
	MC NEUT	MC Genie	Data
2nd track	47.94%	48.71 %	50.38%
e^+/e^-	19.16%	19.89 %	21.75%

Table 5.11: Reduction factor when requiring a second track different from the muon candidate and when applying the other cuts in the electron or positron selection in data and Monte Carlo.

subsection 5.3.4, we will also consider specifically the exclusive CC1π^0 signal.) The purity and the efficiency is given in table 5.12.

NEUT				
Cut	N. events	N.SG	ε(%)	η(%)
Inclusive	326757	39544	53.33	12.10
2nd track	156636	33358	44.99	21.30
e^+/e^-	30015	12749	17.20	42.48

Table 5.12: The selection of CC ν_μ interaction with at least one neutral pion: efficiency, ε, and purity, η, estimated with the MC simulation. The number of generated signal events in NEUT is 74143.

We show the momentum distribution of the electron or the positron depending on the true neutrino interaction type in figure 5.27. 52 % of the selected events correspond to CCDIS interactions, 21 % to CCRES, 3 % to CCQE, 9 % to NC, and 9 % to out of FGD FV interactions. The same momentum distribution is shown depending on the true particle nature in figure 5.28, the true parent type in figure 5.29 and the true grand parent type in figure 5.30. This illustrates the fraction of candidates that are genuine electrons or positrons (70 %) coming from a photon (63 %) produced by a π^0 (48 %).

We select more positive tracks than negative ones: 3296 positrons and 2388 electrons in the data. In figure 5.31 we show the neutrino interaction type according to the charge of the electron or positron candidate. In figure 5.32 we show the true nature of the electron or positron candidate. The positrons are more often confused with positive pions and protons.

The distance between the start position of the muon candidate and the start position of the electron or positron candidate is shown in figure 5.33. We remark two regions in this distribution. The first one at short distance corresponds to the muon candidate and electron or positron candidate being detected in the same TPC, while the second one at larger distance is when they are detected in two different TPCs. The background of protons and pions, coming directly from the neutrino intercation, is located in the peak at very short distance.

The direction of the electron or positron candidate relative to the beam axis is shown on the distribution of the cosine of its polar angle in figure 5.34 according

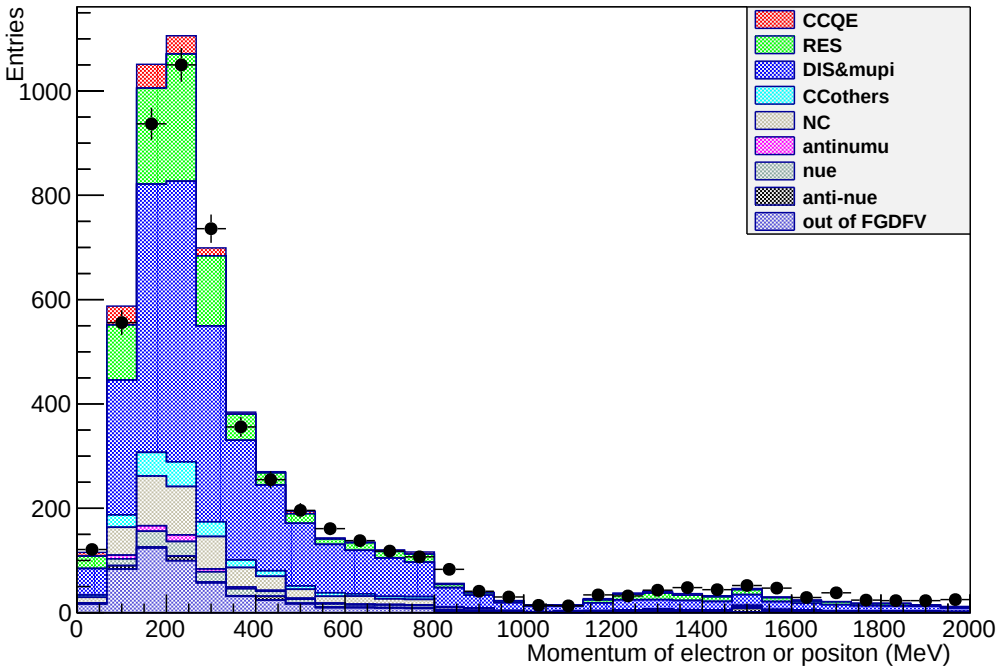

Figure 5.27: The momentum distribution of the electron or positron candidate. The points show the data while the colored histograms show the reweighted simulated data according to the true neutrino interaction type.

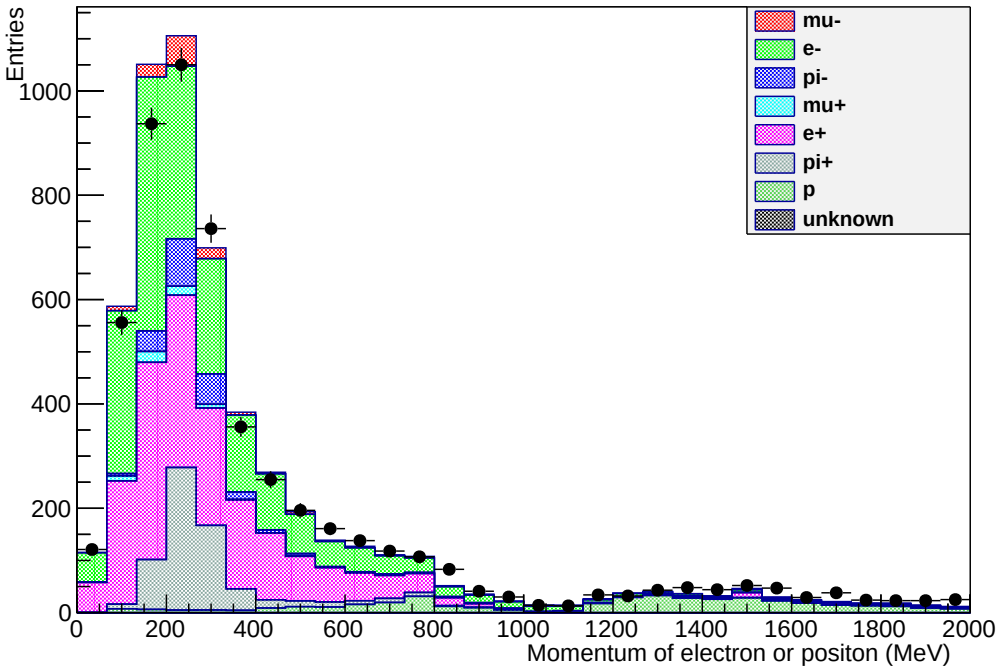

Figure 5.28: The momentum distribution of the electron or the positron candidate. The points show the data while the colored histograms show the reweighted simulated data according to the true particle nature of the candidate.

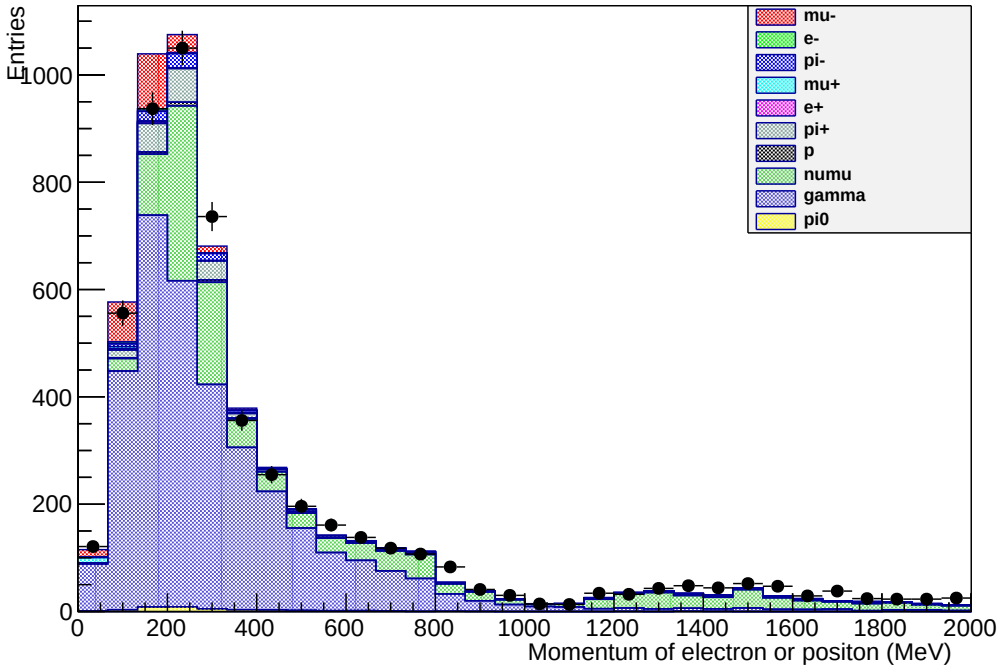

Figure 5.29: The momentum distribution of the electron or the positron candidate. The points show the data while the colored histograms show the reweighted simulated data according to the true particle nature of the true parent of the candidate.

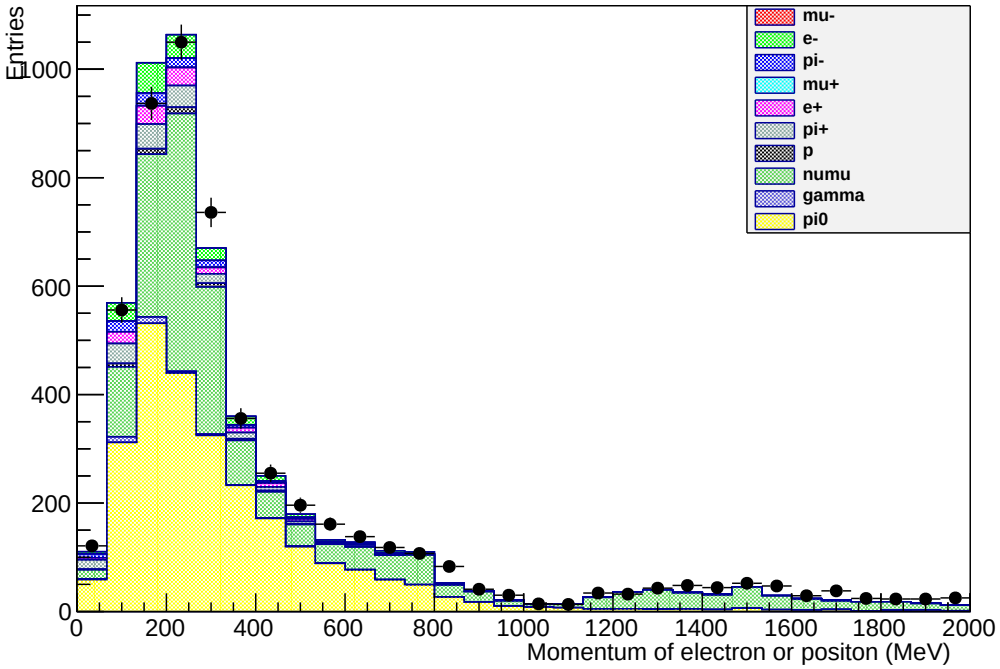

Figure 5.30: The momentum distribution of the electron or the positron candidate. The points show the data while the colored histograms show the reweighted simulated data according to the true particle nature of the true grand parent of the candidate.

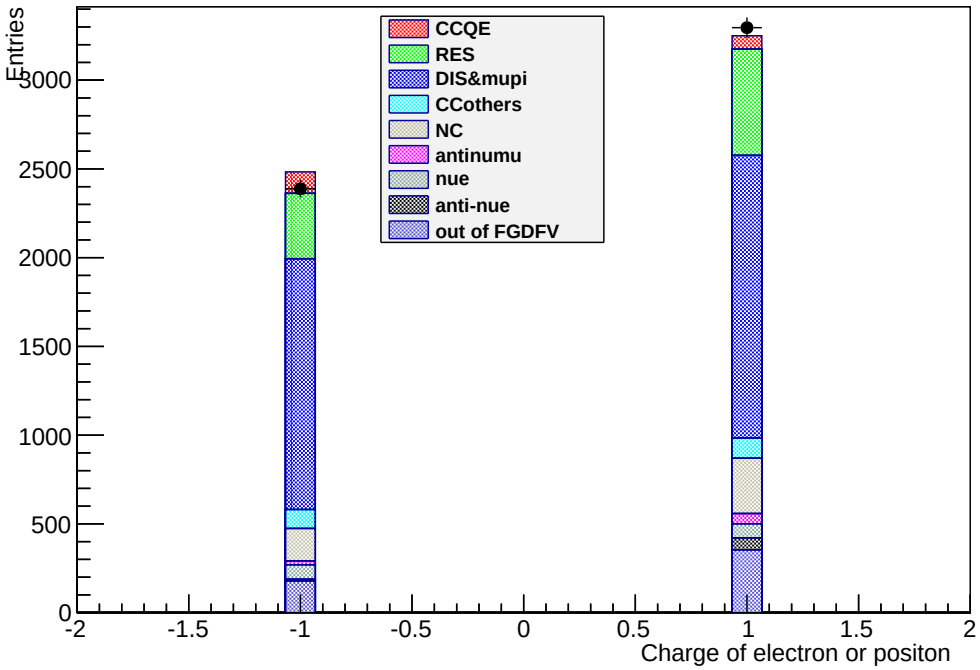

Figure 5.31: The electric charge of the electron or positron candidate. The points show the data while the colored histograms show the reweighted simulated data according to the true neutrino interaction type.

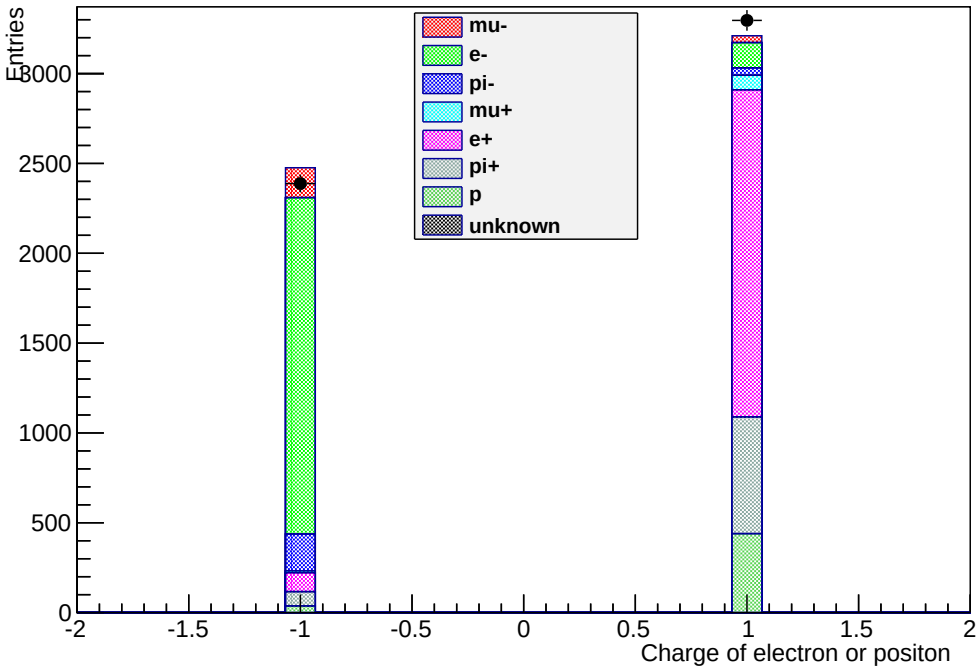

Figure 5.32: The electric charge of the electron or positron candidate. The points show the data while the colored histograms show the reweighted simulated data according to the true particle nature of the candidate.

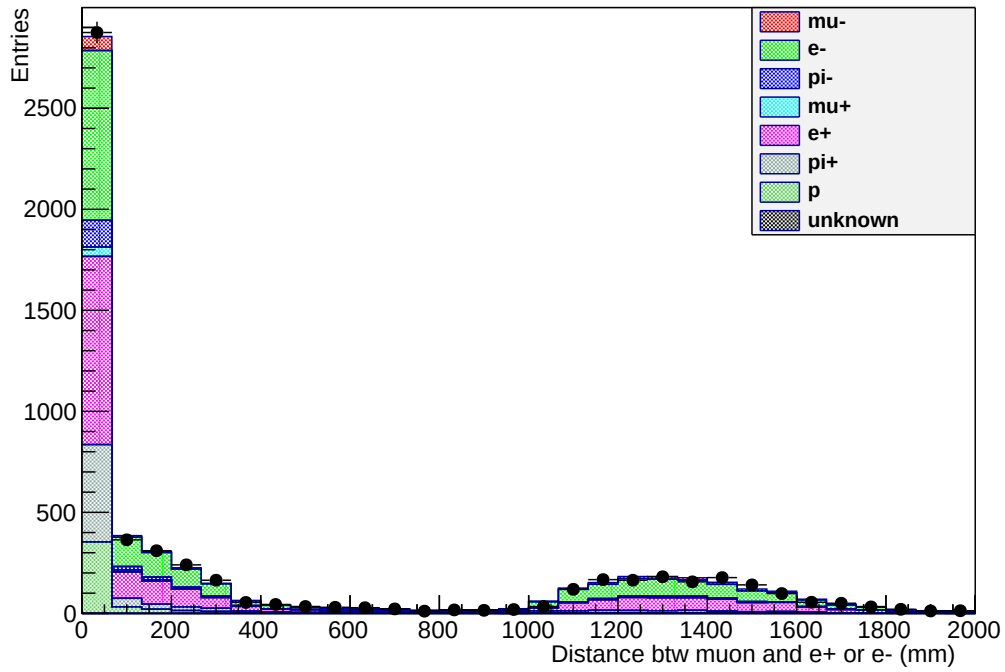

Figure 5.33: The distance between the start position of the muon track and that of the electron or positron track The points show the data while the colored histograms show the reweighted simulated data according to the true nature of the electron or positron candidate.

to the true nature of the candidate and in figure 5.35 according to the true interaction type.

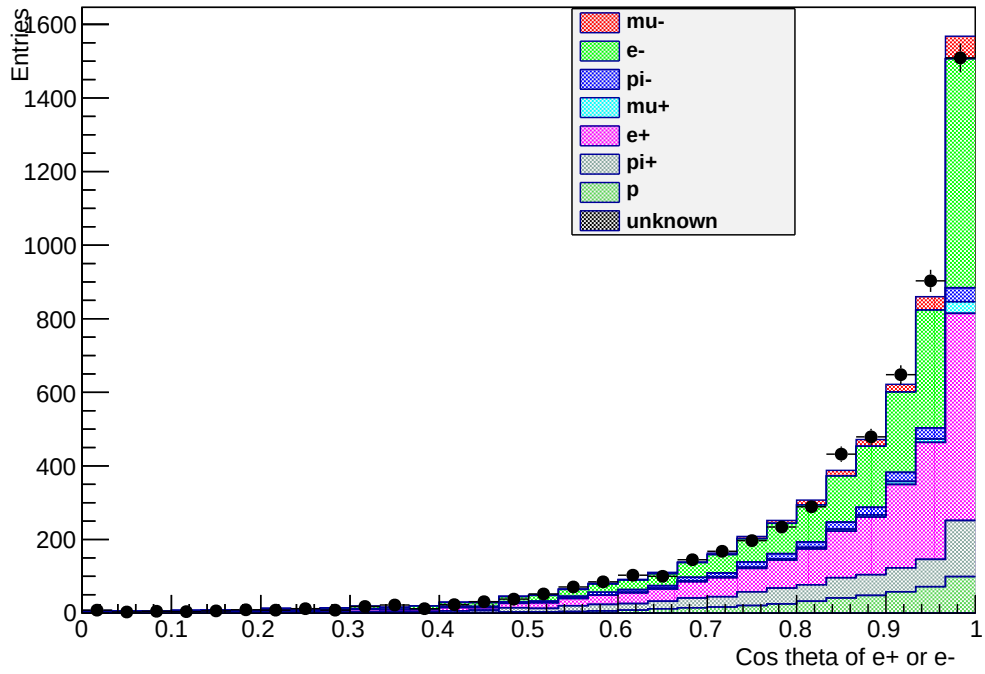

Figure 5.34: The cosine of the polar angle of the electron or positron candidate relative to the beam axis. The points show the data while the colored histograms show the reweighted simulated data according to the true nature of the electron or positron candidate.

Finally, the distribution of the muon candidate momentum once we select the electron or positron is shown in figure 5.36. It is significantly harder than before the electron or positron selection, which can be expected since this selection is enriched in CCDIS events.

Another way to see this effect is to compare the distribution of the true neutrino energy after the muon selection, shown in figure 5.37, and after the subsequent electron and positron selection, shown in figure 5.38, The neutrino energy spectrum is harder after the second selection. The two plots also show the relative contributions of the signal (defined here as a ν_μ CC interaction in the FGD fiducial volume with at least one π^0 in the final state) and the background. The

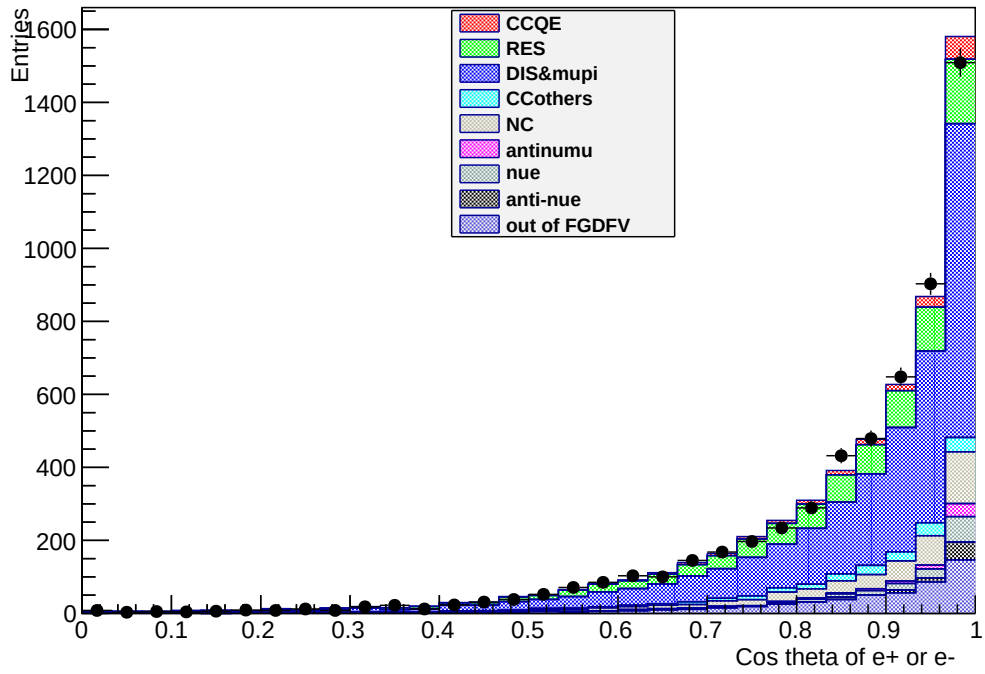

Figure 5.35: The cosine of the polar angle of the electron or positron candidate relative to the beam axis. The points show the data while the colored histograms show the reweighted simulated data according to the true neutrino interaction type.

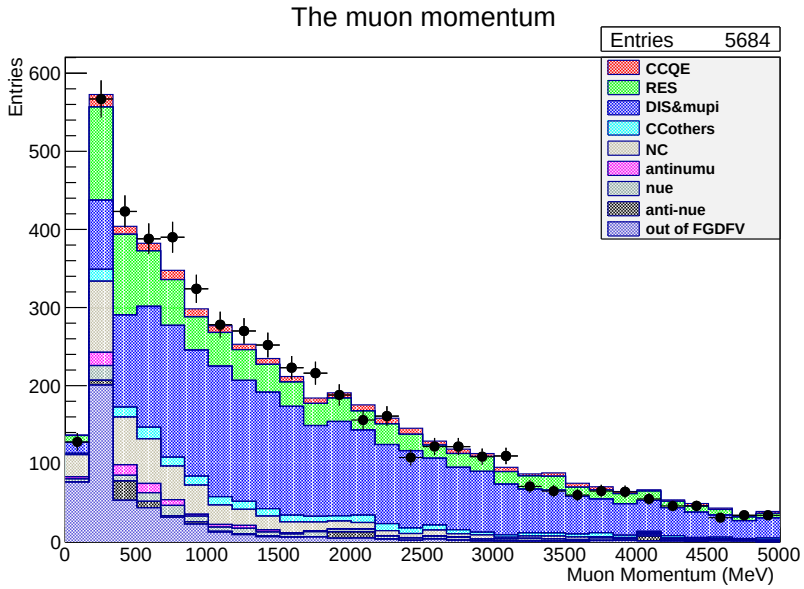

Figure 5.36: The momentum distibution of the muon candidate once the electron or positron is selected. The points show the data while the colored histograms show the reweighted simulated data according to the true neutrino interaction type.

signal fraction increases from 12.9 % after the CC inclusive selection to 42.8 % after the additional requirement of an electron or positron.

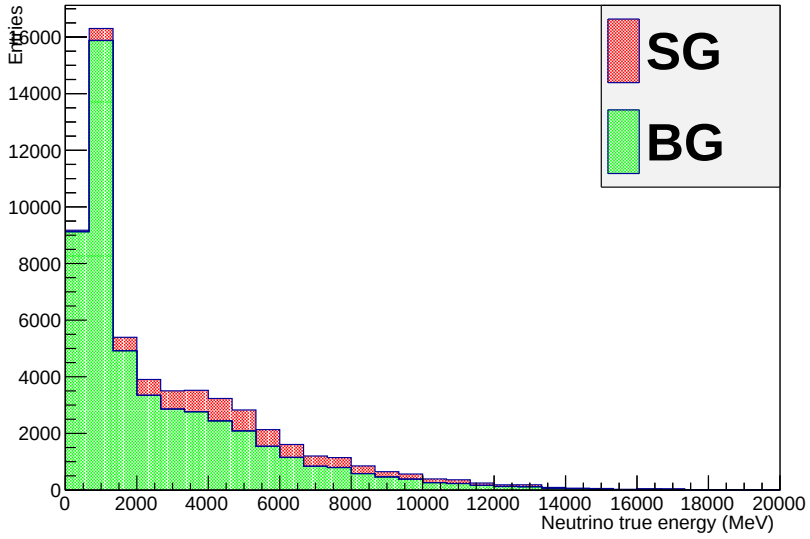

Figure 5.37: The neutrino true energy at the muon selection level with contributions from signal (SG) and background (BG).

5.3.4 Two topologies

The aim of these two topologies is to discriminate between the exclusive CC1π^0 interactions and the other interactions. The other interactions are mainly CCDIS.

The CC1π^0 interaction is the following process: $\nu_\mu + n \rightarrow \mu^- + p + \pi^0$. So in the final state, we may have one muon, one proton (if it is detected in the TPC), and some electrons or positrons coming from the conversion of one (or both) photon(s) from the π^0 decay. Consequently, we define here topology 1 as the subset of events with a muon candidate, zero or one track identified as a proton, and one or two (we also considered one to four, which brings no substantial difference) tracks identified as an electron, and no other tracks. Topology 2 is the subset of events that do not satisfy these conditions, i.e. which have additional tracks.

The composition of these two topologies according to the true neutrino interaction type is illustrated in figure 5.39 for topology 1 and in figure 5.40 for

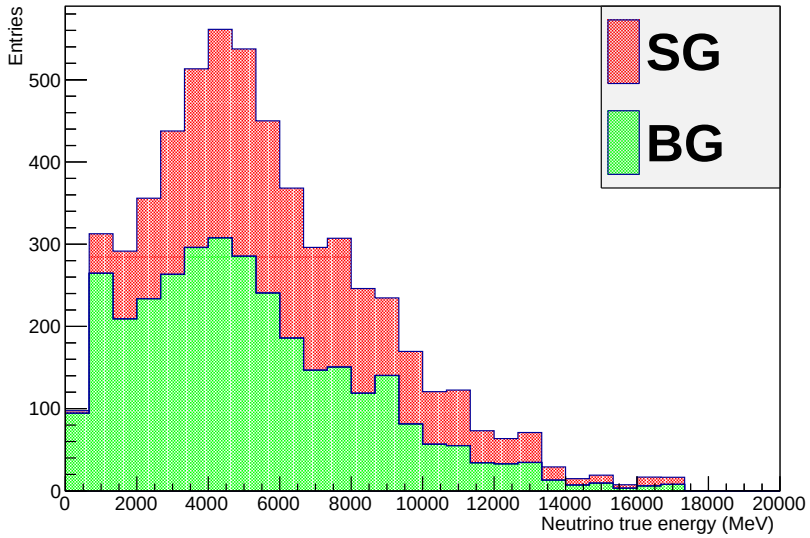

Figure 5.38: The neutrino true energy at the muon and electron or positron selection level with contributions from signal (SG) and background (BG).

topology 2. Topology 2 is enriched in CCDIS events (60 %), while topology 1 is enriched in CCRES events as shown in table 5.13. There is a good agreement between data and Monte Carlo.

The neutrino true energy distribution is shown for the exclusive CC1π^0-enriched topology 1 in figure 5.41 and for the CCDIS-enriched topology 2 in figure 5.42. The fraction of the signal (here ν_μ CC interaction in FGD fiducial volume with at least one π^0 in the final state) is 31.9 % for topology 1 and 46.8 % in topology 2. The composition of the signal in the various samples is given in

ν interaction type	All	Topo1	Topo 2
CCDIS	52.4	30.2	60.1
CCRES	20.8	35.0	15.7
CCQE	3.4	8.6	1.5
NC	8.7	7.9	9.2
Out of FGD FV	9.2	13.8	7.7

Table 5.13: Composition (in %) of neutrino interactions in the FGD FV as a function of the neutrino interaction type for the whole sample and the two topologies (NEUT Monte Carlo).

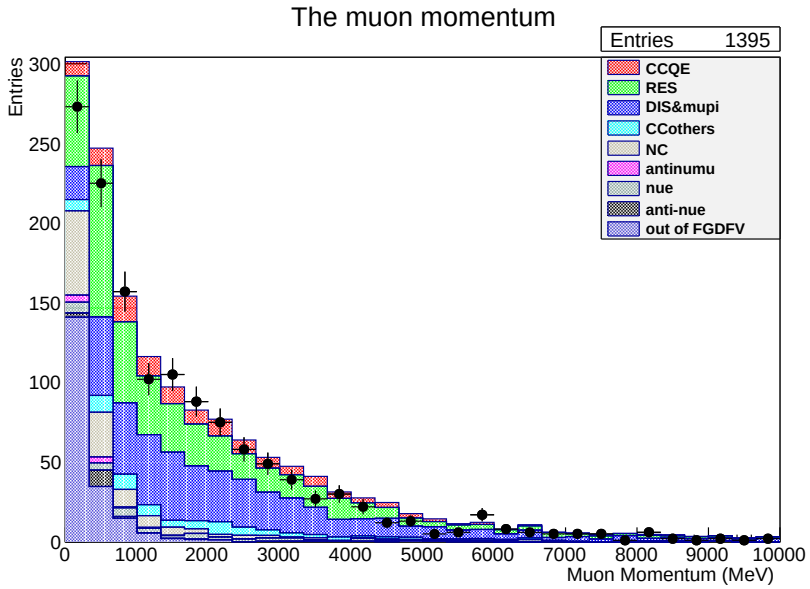

Figure 5.39: The momentum distribution of the muon candiate for topology 1 (enriched in CC1π^0). The points show the data while the colored histograms show the reweighted simulated data according to the true neutrino interaction type.

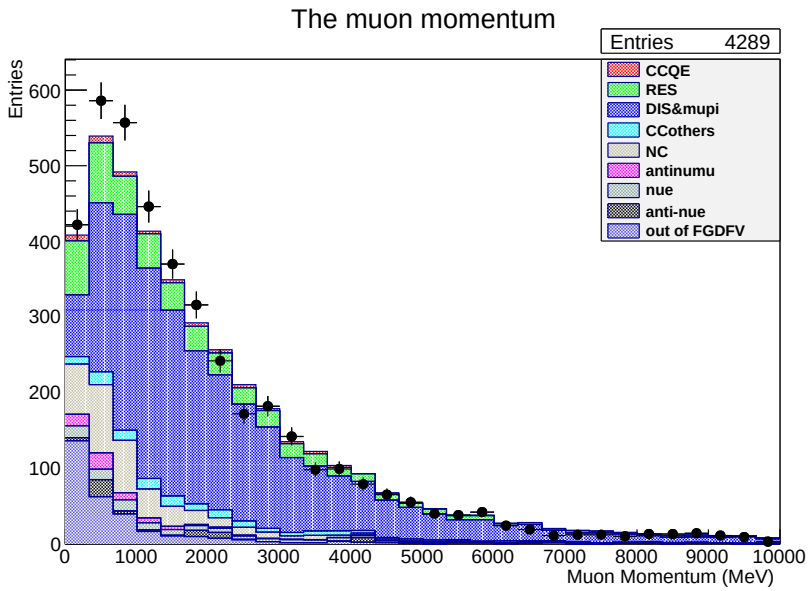

Figure 5.40: The momentum distribution of the muon candidate for topology 2 (enriched in CCDIS). The points show the data while the colored histograms show the reweighted simulated data according to the true neutrino interaction type.

table 5.14.

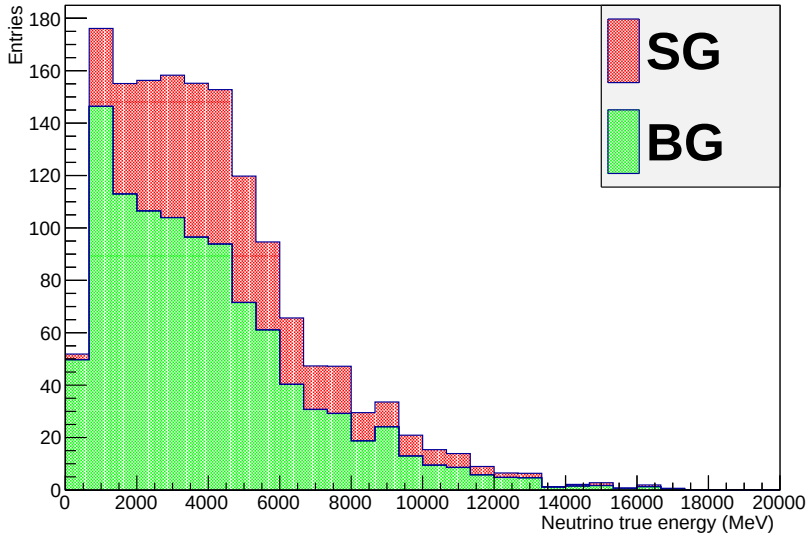

Figure 5.41: The neutrino true energy for the exclusive CC1π^0-enriched topology 1 sample with contributions from signal (SG) and background (BG).

As illustrated in figure 5.43, it is interesting to subdivide topology 1 into two sub-categories:

- topology 1-a: events with exactly one electron or positron candidate,
- topology 1-b: events with more than one electron or positron candidate.

While topology 1-a is dominated by the background, topology 1-b has less background because of the requirement that a second electron or positron is detected. So topology 1-b seems more promising to extract the exclusive CC1π^0 signal.

However, this analysis of ν interactions with π^0 production was not pursued further in this thesis. So the next chapters use the inclusive sample defined in section 5.2 to get the physics results.

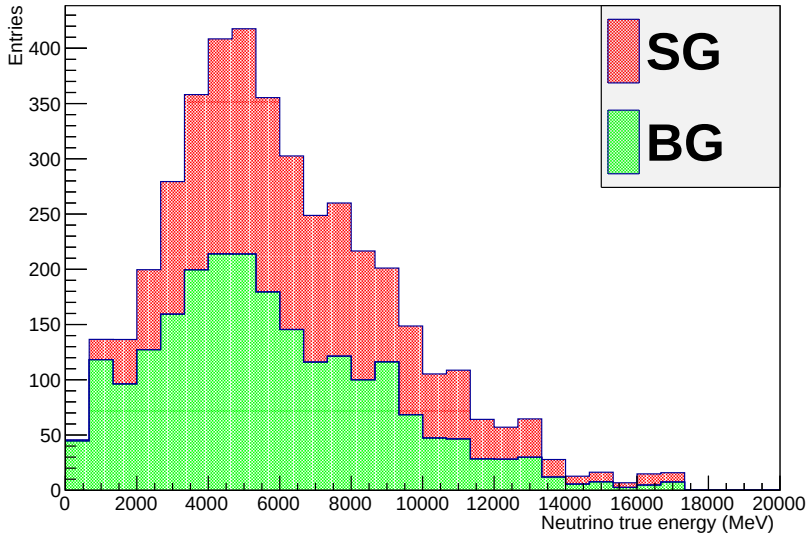

Figure 5.42: The neutrino true energy for the CCDIS-enriched topology 2 sample with contributions from signal (SG) and background (BG).

NEUT signal in FGD FV				
ν interaction type	SG Generation	SG Selection	SG Sel topo1	SG Sel topo 2
CCDIS	48951	10893	1773	9120
$CC1\pi^0$	12651	1002	481	521
$CC1\pi^+(\nu + p)$	6109	352	173	179
$CC1\pi^+(\nu + n)$	3418	317	125	192
CCQE	2502	110	55	55
NC	0	0	0	0
$\nu_\mu + {}^{16}_{8}\mathrm{O}$	0	0	0	0
$\nu_\mu + n \rightarrow \mu + p + \gamma$	1	0	0	0
$\nu_\mu + n \rightarrow \mu + p + \eta$	519	75	28	47
$\nu_\mu + n \rightarrow \mu + \Lambda + K$	0	0	0	0
all ν_μ	74143	12749	2635	10114

Table 5.14: The signal (CC ν_μ interaction with at least one neutral pion) composition at the generation level, at the the selection level, and for the two topologies (NEUT MC).

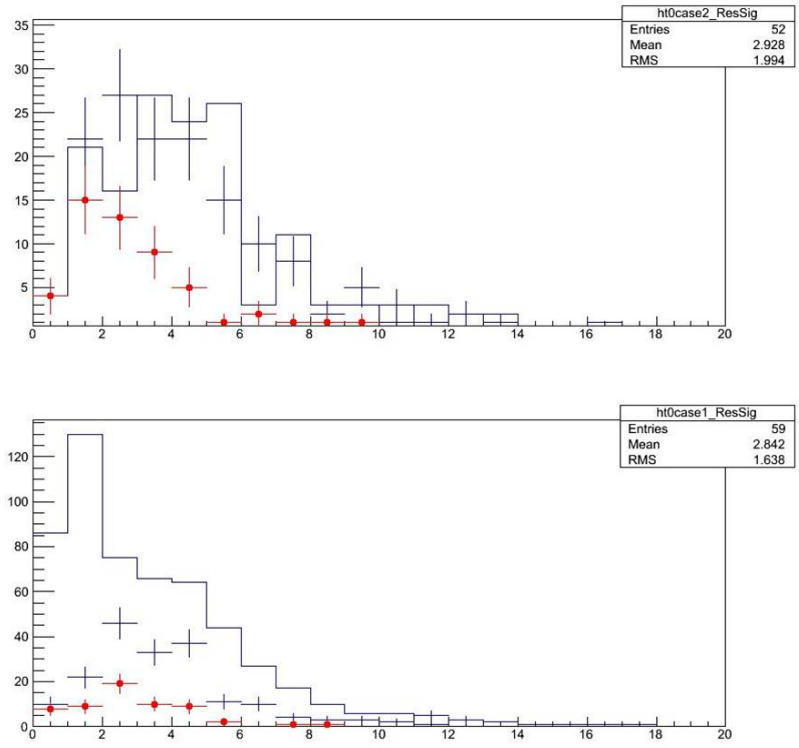

Figure 5.43: Composition of the (top) topology 1-b and (bottom) topology 1-a samples. The red points show the exclusive CC1π^0 interactions. The blanck points show the CCDIS with at least one π^0. The histogram is for the background.

Chapter 6

Analysis tools

The goal of this thesis is to measure the charged current deep inelastic scattering ν_μ cross section. The measurement is interesting for itself. It is also an input to neutrino oscillation analysis, especially for future very long baseline experiments, which will work in a neutrino energy range, where the deep inelasting scattering process is the dominant one.

The charged current deep inelastic scattering neutrino cross section is extracted as a function of neutrino energy by a likelihood fit. In this chapter, the tools used in this measurement are introduced. The reconstruction of the neutrino energy is described in section 6.1. The predictions of various ingredients for the fit are dicussed in section 6.2. The fit used to measure the cross section is explained in section 6.3. Finally, the validation of the fit is presented in section 6.4.

6.1 Energy measurement

The goal of the analysis is to measure for a given process (the charged current deep inelastic scattering in this thesis) the neutrino cross section as a function of its energy. So an important ingredient is the measurement of the neutrino energy. Subsection 6.1.1 describes how the neutrino energy is reconstructed. The resolution of this energy measurement is discussed in subsection 6.1.2.

6.1.1 Neutrino energy reconstruction

Two different methods are used to reconstruct the neutrino energy in the sample obtained after the muon selection described in chapter 5. They are given in subsection 6.1.1.1 for topology 1 and in subsection 6.1.1.2 for topology 2.

6.1.1.1 Energy reconstruction in topology 1

For topology 1, which contains events with at most two reconstructed tracks, the dominant process is the charged current quasi-elastic interaction. So we could try to use the formula giving the energy reconstructed under the CCQE hypothesis. As discussed in subsection 1.3.2.1, for charged current quasi-elastic ν_μ interactions, the neutrino energy can be accurately reconstructed using only the measured momentum $\boldsymbol{p}_\mu$ and direction $\cos\theta_\mu$ of the muon. The formula, already given in equation 1.10, is repeated here:

$$E_\nu^{CCQE} = \frac{m_P^2 - m_\mu^2 - E_N^2 + 2E_N E_\mu}{2(E_N - E_\mu + \boldsymbol{p}_\mu \cos\theta_\mu)}. \tag{6.1}$$

It works well for the low multilicity events of topology 1, as shown in figure 6.1. The agreement is very good for events with exactly one track. For events with two tracks, the second track being a proton as in the CCQE process or another particle, it is not as good, but still acceptable.

6.1.1.2 Energy reconstruction in topology 2

However, for the events with at least three reconstructed tracks of our topology 2 sample, the CCQE hypothesis is not a good one and the CCQE formula does not work well. There is a a poor agreement between the neutrino true energy and the energy reconstructed with the CCQE formula, as shown in the bottom plot of figure 6.2. So we have to find another way to reconstruct the neutrino energy using the information of all the tracks in the event.

For events of topology 2, the neutrino reconstructed energy is calculated as the sum of the momentum modules of all tracks in the event $\Sigma|p|$. The top plot of figure 6.2 shows that this variable is a good estimator of the true neutrino energy.

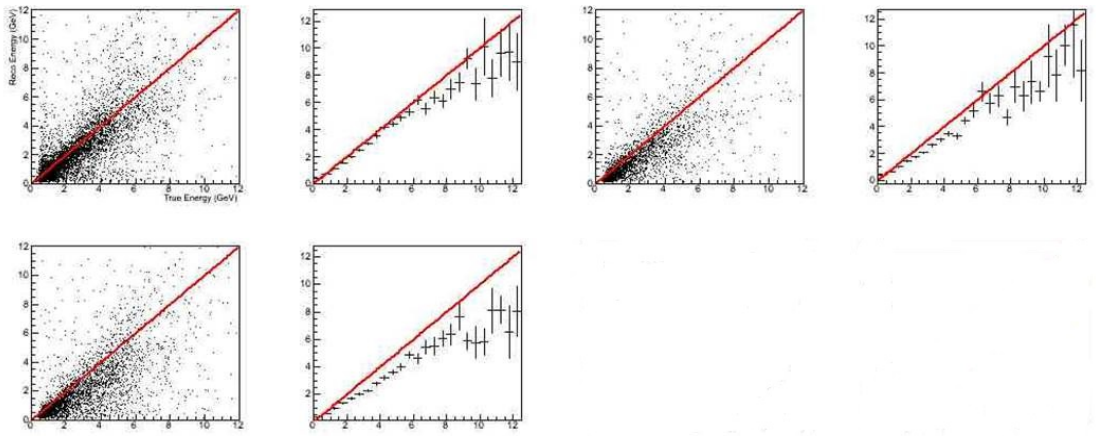

Figure 6.1: Neutrino reconstructed energy as a function of the neutrino true energy for topology 1 Monte Carlo events. The reconstructed energy is calculated with the CCQE formula. The events are divided into three categories: events with (top left) exactly one track, (top right) exactly two tracks with a proton, and (bottom left) exactly two tracks without a proton. For each category, two plots are shown: (left) the scatter-plot and (right) the profile histogram.

6.1.2 Energy resolution

As seen in subsection 6.1.1, the neutrino reconstructed energy does not correspond exactly to its true energy. This energy resolution effect has to be taken into account in the analysis. This is done using so-called transfer matrices, which express the correspondance between the reconstructed energy and the true energy in energy bins. The transfer matrices are calculated separately for the two topologies and, inside each topology, for the four ν interaction categories:

- charged current quasi-elastic (CCQE),
- charged current single pion production (CCRES),
- charged current deep inelastic scattering (CCDIS),
- neutral current (NC).

These transfer matrices are shown graphically in figure 6.3 in case of topology 1 and in figure 6.4 in case of topology 2. For clarity, this figures show only

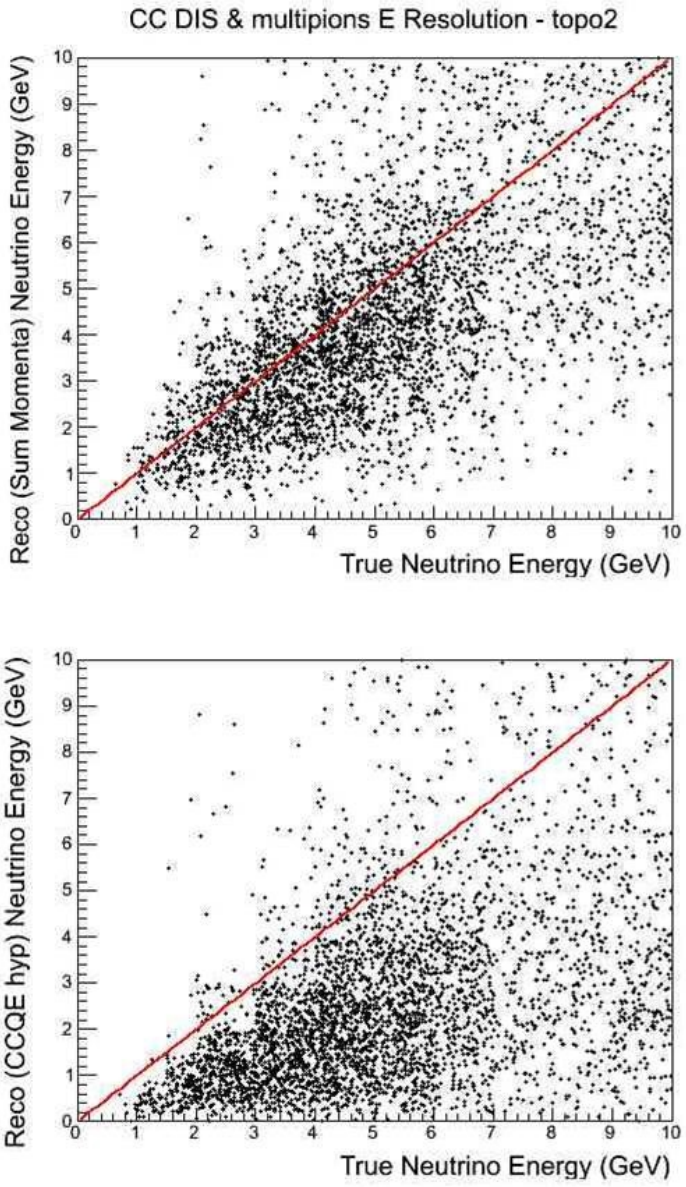

Figure 6.2: Neutrino reconstructed energy as a function of the neutrino true energy for topology 2 Monte Carlo events. The reconstructed energy is calculated (top) as the sum of the momentum modules of all tracks in the event and (bottom) with the CCQE formula.

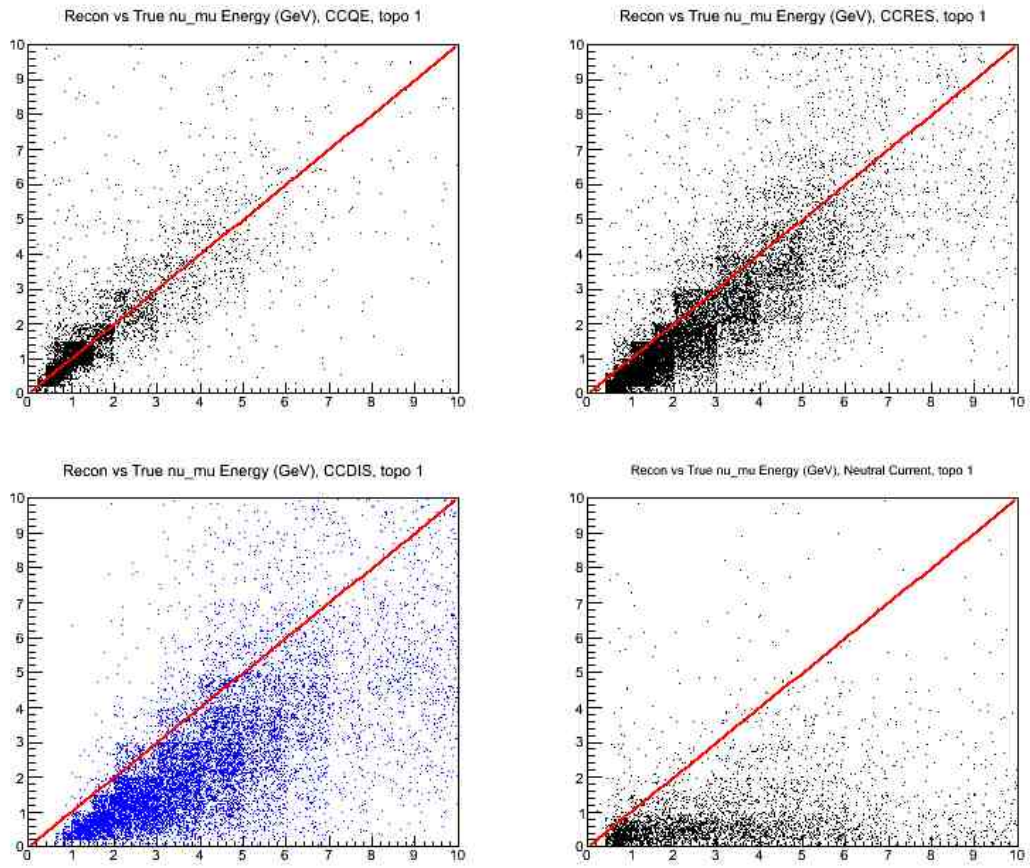

Figure 6.3: Graphical view of the transfer matrices for topology 1 Monte Carlo events. The neutrino reconstructed energy is shown as a function of the neutrino true energy. The four processes are shown separately: (top left) CCQE, (top right) CCRES, (bottom left) CCDIS, and (bottom right) NC.

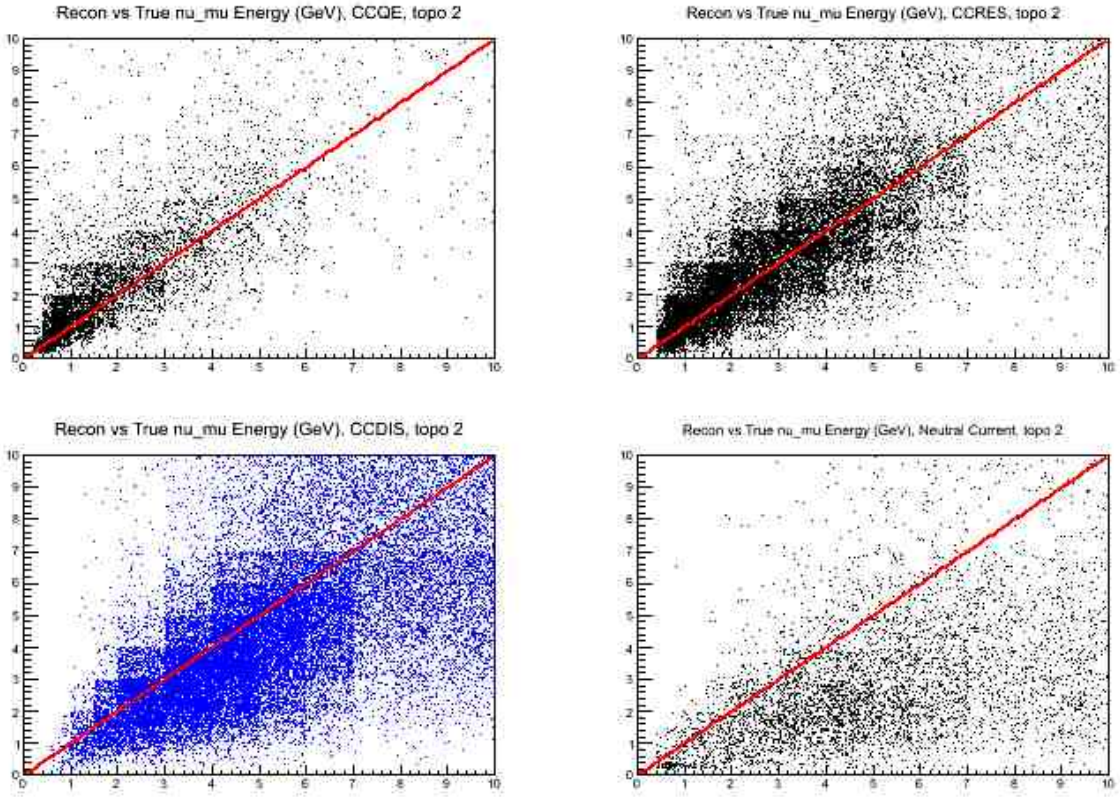

Figure 6.4: Graphical view of the transfer matrices for topology 2 Monte Carlo events. The neutrino reconstructed energy is shown as a function of the neutrino true energy. The four processes are shown separately: (top left) CCQE, (top right) CCRES, (bottom left) CCDIS, and (bottom right) NC.

the most interesting region up to 10 GeV. But the higher energy region is also parametrised in the tranfer matrices.

6.2 Predictions

Prior to performing the fit, a certain number of ingredients are needed. They are reviewed in this section. First the flux prediction is given in subsection 6.2.1. Then the cross section prediction is presented in subsection 6.2.2 and the number of nuclei in the target in subsection 6.2.3. Finally the parametrisation of the efficiencies is discussed in subsection 6.2.4.

6.2.1 Flux

The neutrino flux is predicted by the neutrino beam Monte Carlo. Generating the neutrino beam is the first step in the MC simulation chain of T2K. The interactions of 30 GeV protons with the nuclei of the graphite target and the resulting particles are simulated with FLUKA2008. The MC is tuned to the data of NA61/SHINE [43], a hadroproduction experiment at CERN which uses a replica of the T2K target. The produced particles are then transferred to JNUBEAM, a specific simulation code for the J-PARC neutrino beam based on GEANT3, which was developed to predict the neutrino flux at the ND280 and Super-Kamiokande detectors. This simulation replicates the geometry of the secondary beamline, in particular it includes the horn magnetic fields [57].

There are several versions of the neutrino flux prediction. Since our MC sample was generated with an older version of the flux prediction, we will use the same flux release as the one used to generate the MC to test and validate the flux measurement algorithm. But we will use the latest release to compare data and Monte Carlo and to perform the fit on the data. The ratio of these two flux predictions has been presented in figure 5.1 of section 5.1. The flux prediction can be seen in figure 2.5 of section 2.2. The peak energy is at about 600 MeV, and the energy spectrum has a long high energy tail. Table 6.1 gives the values and uncertainties of the predicted ν_μ flux in different neutrino energy bins.

Bin	Energy range (GeV)	Flux prediction	Uncertainty (%)
1	0.0-0.6	8.967	12.1
2	0.6-1.0	7.238	11.9
3	1.0-2.0	1.807	11.4
4	2.0-3.0	0.472	9.9
5	3.0-4.0	0.295	9.6
6	4.0-5.0	0.202	11.6
7	5.0-7.0	0.174	14.7
8	7.0-10.0	0.081	20.5
9	> 10.0	0.026	19.0

Table 6.1: Prediction of the ν_μ flux in $10^{12}/10^{21}$ POT/cm^2 and its relative uncertainty in % for different bins of neutrino energy from the neutrino beam Monte Carlo tuned with the SHINE data [57].

6.2.2 Cross sections

The neutrino interaction cross sections are computed using the prescriptions indicated in chapter 1 for the four interaction types:

- charged current quasi-elastic (CCQE),
- charged current single pion production (CCRES),
- charged current deep inelastic scattering (CCDIS),
- neutral current (NC).

Figure 6.5 shows the different cross sections as a function of the true neutrino energy, for each atom type and each interaction category.

The uncertainties for each interaction category [36] are summarised in table 6.2. These errors are split in two large energy bins, i.e. $E_\nu < 2$ GeV and $E_\nu > 2$ GeV, and the energy bins are considered to be fully correlated.

Of peculiar interest is the predictions of the cross section for the deep inelastic scattering ν_μ interactions, which we want to measure. They are given in table 6.3 for the three main atom types that are present in the FGD target: carbon, hydrogen, and oxygen.

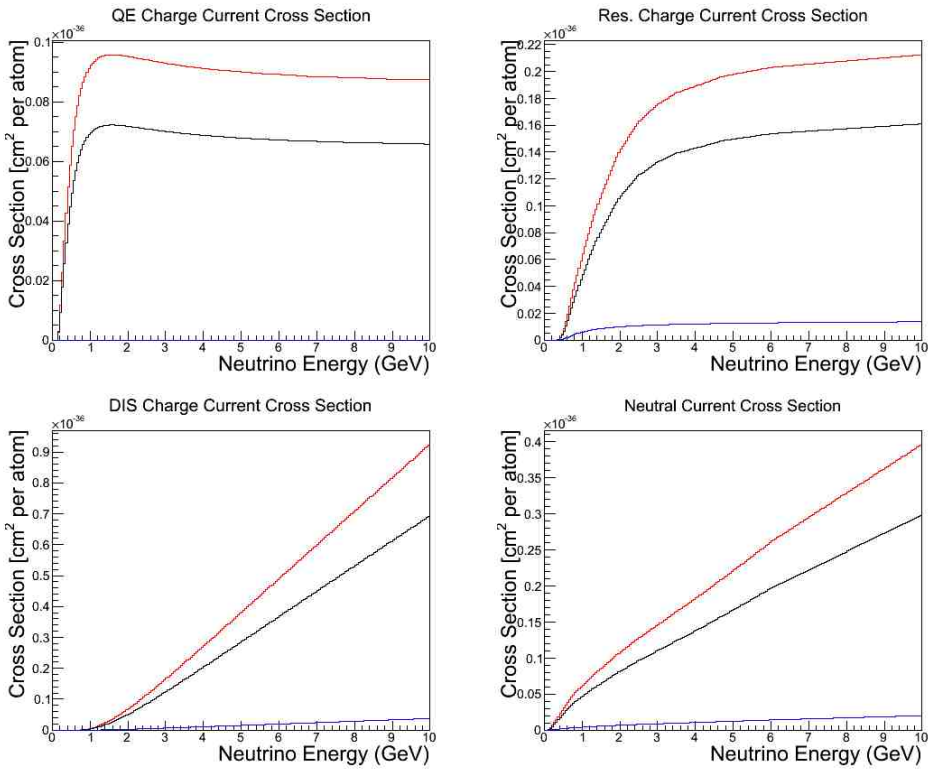

Figure 6.5: Neutrino cross sections on (black) carbon, (red) oxygen, and (blue) hydrogen for the (top left) CCQE, (top right) CCRES, (bottom left) CCDIS, and (bottom right) NC interaction categories. ν_μ cannot interact with hydrogen nuclei via the CCQE channel since these nucelei don't contain any neutron.

	$E_\nu < 2$ GeV	$E_\nu > 2$ GeV
CCQE	25 %	25 %
CCRES	47 %	31 %
CCDIS	30 %	25 %
NC	36 %	36 %

Table 6.2: Uncertainty on the cross section for each interaction category as a function of the true neutrino energy.

Energy range (GeV)	Carbon	Hydrogen	Oxygen
0.0-2.0	0.012	0.0007	0.016
2.0-4.0	0.125	0.0067	0.166
4.0-6.0	0.285	0.0154	0.380
6.0-10.0	0.534	0.0290	0.711

Table 6.3: Prediction of the CCDIS ν_μ cross sections in 10^{-36} cm^2/atom for different bins of neutrino energy on carbon, hydrogen, and oxygen targets, respectively [30].

6.2.3 Number of nuclei

Furthermore, the cross section measurement of neutrino interaction depends on the exact number and type of target nuclei. Table 6.4 gives the number of atoms in the total volume and fiducial volume of each FGD. FGD1, essentially made of plastic scintillator, is mainly composed of carbon and hydrogen atoms. FGD2, which also contains water, has also a lot of oxygen atoms.

N atoms (in 10^{28})	Hydrogen	Carbon	Oxygen	Others
FGD1 total	4.88±0.06	4.80±0.02	0.15±0.01	0.05±0.01
FGD2 total	5.93±0.03	2.68±0.01	1.69±0.01	0.03±0.01
FGD1 fiducial	4.06±0.05	3.99±0.02	0.13±0.01	0.04±0.01
FGD2 fiducial	5.14±0.03	2.24±0.01	1.51±0.01	0.03±0.01

Table 6.4: Atomic composition of each FGD given in 10^{28} atoms, for the total volume and for the fiducial volume.

In this thesis, we will only measure an average neutrino cross section over the various nuclei present in the FGD.

6.2.4 Efficiencies

The global selection efficiency has been introduced in chapter 5. In the subsequent fit, we need the selection efficiency per interaction type (CCQE, CCRES, CCDIS, and NC). It is defined as the ratio of the number of selected events of a given interaction type over the number of generated events of this interaction type in the FGD fiducial volume. It is expressed as a function of the neutrino true energy

and was shown in figure 5.12. The efficiency decreases rapidly at small neutrino energy.

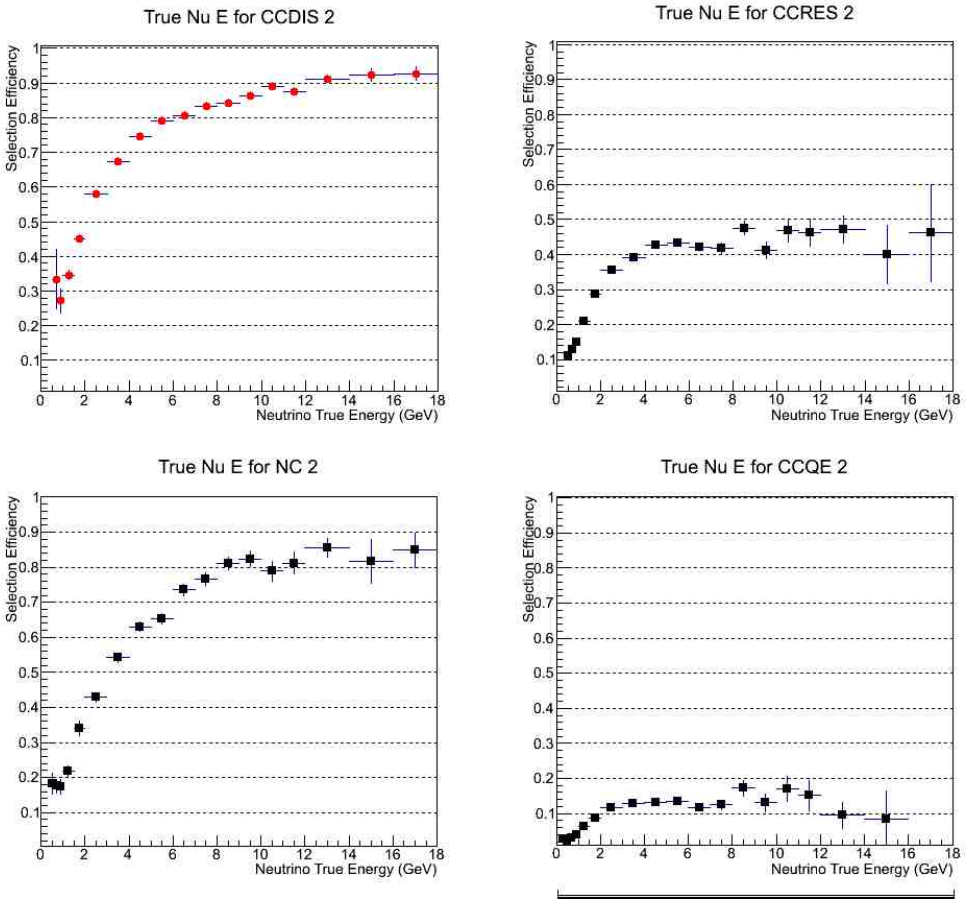

Figure 6.6: Relative efficiencies, defined as the fraction of topology events, as a function of neutrino true energy for the (top left) CCDIS, (top right) CCRES, (bottom left) NC, and (bottom right) CCQE interaction categories.

Besides, for the fit by topologies, we need an additional quantity, which we call the relative efficiency ϵ_r^i for topology i ($i = 1$ or 2). It is defined for each interaction process as the fraction of selected events of this process which belongs to topology i. With exactly two topologies, we have of course $\epsilon_r^1 + \epsilon_r^2 = 1$. The relative efficiency for topology 2 is illustrated in figure 6.6. It increases with the neutrino energy to reach a plateau around 90 % for our CCDIS signal, and 80 %

for the NC (most of the selected NC is NC DIS), 40 % for the CCRES, and 10 % for the CCQE backgrounds.

In the fit with topologies, the efficiencies used are the products of the global efficiencies by the relative efficiencies.

6.3 The fit description

The analysis is based on a binned maximum likelihood fit of the measured neutrino energy distributions in two topologies. The likelihood used is introduced in subsection 6.3.1. The various fits, according to which parameters are left free, are discussed in subsection 6.3.2.

6.3.1 The likelihood

Once the neutrino energy has been computed, for each reconstructed neutrino energy bin, the probability of observing n_{obs} events knowing that we expect n_{exp} events for the same measured neutrino energy bin is given by the Poisson distribution:

$$P(n_{obs}|n_{exp}) = \frac{e^{-n_{exp}} \times n_{exp}^{n_{obs}}}{n_{obs}!}. \tag{6.2}$$

Therefore, the likelihood function can be written as a product over the N measured energy (e_{meas})bins:

$$\mathcal{L} = \prod_{e_{meas}=1}^{N} \frac{n_{exp}(e_{meas})^{n_{obs}(e_{meas})}}{e^{n_{exp}(e_{meas})}} \tag{6.3}$$

While $n_{exp}(e_{meas})$ depends upon the free variables in the fit, $n_{obs}(e_{meas})$ does not, as it is given by the number of events from the data sample in the relevant energy bin. Thus the terms $n_{obs}!$ from equation 6.2 for each energy bin have been removed since these are constant and therefore do not intervene in the maximisation of the likelihood. For practical reasons, we will minimise a quantity equal to minus

the logarithm of the likelihood:

$$-ln(\mathcal{L}) = \sum_{e_{meas}=1}^{N} n_{exp}(e_{meas}) - n_{obs}(e_{meas}) \times ln(n_{exp}(e_{meas})) \tag{6.4}$$

which is equivalent to maximising $\mathcal{L}$.

We can also fit simultaneously the two topologies introduced in subsection 5.2.3. In this case, a likelihood function $\mathcal{L}^{i_{topo}}$ is defined as in equation 6.3 for each topology and we minimise the quantity:

$$\sum_{i_{topo}=1}^{2} -ln(\mathcal{L}^{i_{topo}}) \tag{6.5}$$

While the $n_{obs}(e_{meas})$ are obtained directly from the reconstructed ν_μ energy spectrum, either from the data sample or the MC sample, the expected number of events $n_{exp}(e_{meas})$ for ν_μ interactions in the FGD FV is calculated as an integral over the true neutrino energy e_{true}. In practice, the integral is computed as a sum over small energy bins. We use the following expression:

$$\begin{aligned} n_{exp}(e_{meas}) &= \int_0^\infty n_{exp}(e_{true}) de_{true} \times P(e_{meas}|e_{true}) \\ &+ n_{exp}^{outofFGD}(e_{meas}) + n_{exp}^{\overline{\nu}_\mu}(e_{meas}) + n_{exp}^{\nu_e}(e_{meas}) + n_{exp}^{\overline{\nu}_e}(e_{meas}) \end{aligned} \tag{6.6}$$

where $P(e_{meas}|e_{true})$ is the probability to reconstruct the true neutrino energy e_{true} as a neutrino energy in the e_{meas} bin, which is modelised through the transfer matrices introduced in subsection 6.1.2, and the various $n_{exp}^{background}(e_{meas})$ are the expected contributions from the different background sources, i.e. the contributions from the out-of-FGD, the $\overline{\nu}_\mu$, the ν_e, and the $\overline{\nu}_e$ events. Since these contributions are fixed, we will assign them systematic errors, as it will be explained in section 7.3.

The expected number of events for a given true neutrino energy $n_{exp}(e_{true})$ is calculated from:

- the ν_μ neutrino flux $\Phi(e_{true})$, which is predicted as a function of the true neutrino energy e_{true} ;

- the number of atoms of each type (j_{atom}) in the fiducial volume $N_{j_{atom}}$;
- the cross sections $\sigma_{j_{atom},k_{proc}}$ for different neutrino interaction processes (k_{proc}) on different nuclei ;
- the selection efficiencies $\epsilon_{k_{proc}}(e_{true})$ defined as the ratio of the number of selected events to the number of generated events per interaction type for the given true neutrino energy in the fiducial volume.

Some simplifications have been made to ease the calculation:

- although the FGDs are made of several nuclei, we consider only the three main atomic components, given in table 6.4 of subsection 6.2.3: carbon, hydrogen, and oxygen ;
- the interaction processes have been grouped into four categories: CCQE only ($k_{proc} = 1$), CCRES ($k_{proc} = 2$) which includes charged current incoherent and coherent single pion production, CCDIS ($k_{proc} = 3$) which includes charged current multi-pion production, and NC ($k_{proc} = 4$) which groups all neutral current interactions.
- the fitted parameters, which may be flux factors $f(e_{true})$ or/and cross section factors $F^{k_{proc}}(e_{true})$.

Therefore, $n_{exp}(e_{true})$ can be written as:

$$n_{exp}(e_{true}) = f(e_{true}) \times \Phi(e_{true}) \times \sum_{j_{atom}=C,H,O} N_{j_{atom}} \sum_{k_{proc}=1}^{4} F^{k_{proc}}(e_{true}) \sigma_{j_{atom},k_{proc}} \times \epsilon_{k_{proc}}(e_{true}). \tag{6.7}$$

6.3.2 The free parameters

In practice, the fit is based on the MINUIT minimisation package. A first pass, using MIGRAD, is used to find the fitted parameters corresponding to the the minimum, and the parabolic errors associated with them. A second pass, using MINOS, refines the mimimisation. In particular, it allows a more precise calculation of the errors on the fitted parameters, by giving a negative error and a

positive error. These two quantities can differ in the case that the error is not parabolic, but assymmetric.

We consider several fit configurations, allowing the measurement of various variables.

- Fit of the flux:
  When fixing all cross section factors $F^{k_{proc}}(e_{true}) = 1$ and leaving free the $f(e_{true})$ flux factors, we measure the ν_μ flux, in fact the correction factors of the flux with respect to the predicted flux. In other words, these flux factors should be close to one if the prediction is correct. In practice we consider nine energy bins and consequently nine flux factors $f_i, i = 1, ..., 9$. The energy bins have been given in table 6.1.

- Fit of the CCDIS cross section:
  When now fixing all flux factors $f(e_{true}) = 1$ and cross section factors except for CCDIS $F^{k_{proc}}(e_{true}) = 1$ ($k_{proc} \neq 3$) and leaving free only the CCDIS cross section factors $F^3(e_{true})$, we measure the CCDIS cross section in terms of correction factors with respect to the predicted cross section. Note that this could be done in principle for other processes as well, though in this thesis we focus on the CCDIS cross section measurement. In practice, we use four energy bins shown in table 6.5. Only the three factors F_2, F_3, and F_4 are left free in the fit, F_1 being fixed since the first energy bin contains very few CCDIS events.

Coefficient	Energy range (GeV)
F_1	0.0-2.0
F_2	2.0-4.0
F_3	4.0-6.0
F_4	> 6.0

Table 6.5: Energy bins used for the cross section fit.

- Simultaneous fit of the flux and the CCDIS cross section:
  While still fixing all cross section factors except for CCDIS $F^{k_{proc}}(e_{true}) = 1$ ($k_{proc} \neq 3$), we now leave free both the $f(e_{true})$ flux factors and the CCDIS cross section factors $F^3(e_{true})$. Of course, in this configuration, as

the expected number of events given in equation 6.7 depends on products of the flux and cross section factors, the fit can only work if we add an additional term to the likelihood. This additional term is the beam flux constraint, expressed as:

$$\frac{\chi^2}{2} = \frac{1}{2}\delta f^T V^{-1} \delta f, \tag{6.8}$$

where δf is the column vector giving for several energy bins the difference $f(e_{true}) - 1$ between the fitted and expected flux factors, and V is the beam flux full covariance matrix, coming from the neutrino beam Monte Carlo tuned with the data from the SHINE experiment.

The V covariance matrix is illustrated in fig 6.7 and the square root of each of its diagonal elements, which gives the uncertainty, is listed in the last column of table 6.1. The uncertainty is higher at high energy as the neutrinos come from kaon decays and the uncertainty on hadroproduction is higher for kaons than for pions. The relative flux correlation coefficient are explicited in table 6.6, which shows a strong and positive correlation between all terms. The same physics effects are indeed at the origin of the flux prediction in the different energy bins. This χ^2 term measures how close the fitted flux factors are to the predicted ones, taking into account all the correlations between the fluxes in the different energy bins.

The advantage of this simultaneous fit method is to include in the error returned by the fitting program the systematic error due to the uncertainty on the flux. Another strength of the simultaneous fit is to return central values for the CCDIS cross section factors that are not biased by differences between the predicted neutrino flux and the physical neutrino flux.

6.4 Validation of the fit

Before fitting the data, it is necessary to validate the fitting program on the simulated sample. We first validate the fit of the flux in subsection 6.4.1, then the fit on the cross section in subsection 6.4.2, and then the combined fit in

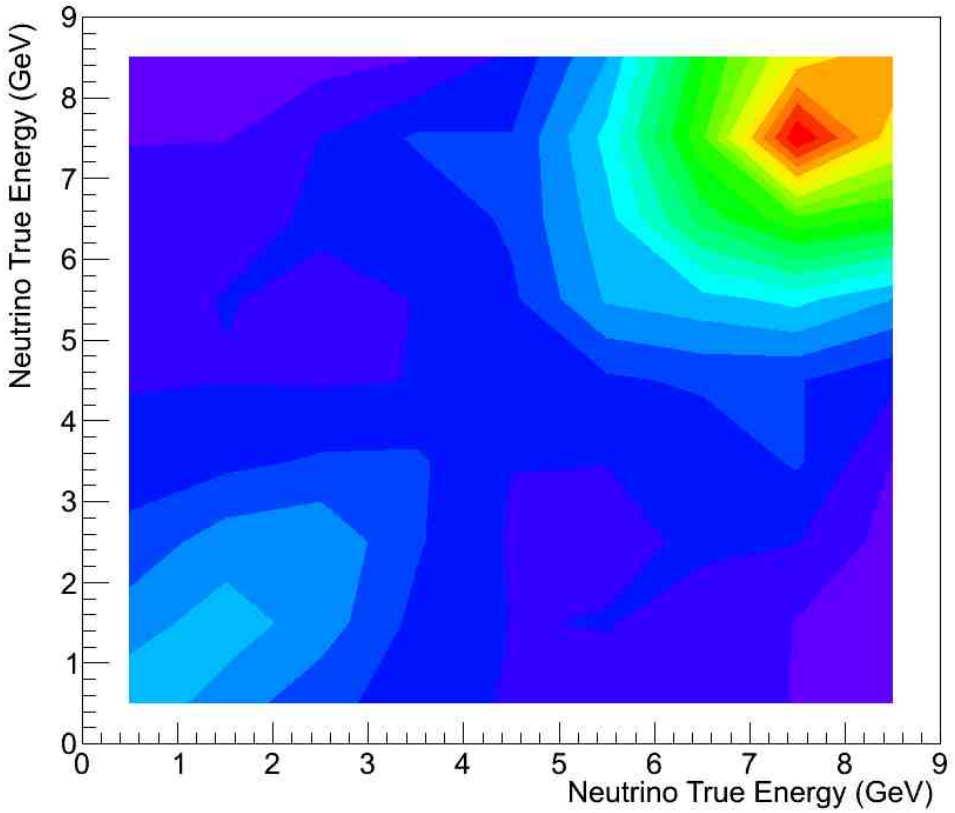

Figure 6.7: Graphical view of the neutrino beam correlation matrix. The color shows the magnitude of each element (increasing from blue to red). The diagonal elements correspond to the squared uncertainties on the relative flux. They are higher at high neutrino energy.

Average fit	f_1	f_2	f_3	f_4	f_5	f_6	f_7	f_8	f_9
f_1	1.00	0.86	0.73	0.72	0.64	0.52	0.37	0.22	0.16
f_2	0.86	1.00	0.91	0.76	0.66	0.55	0.42	0.23	0.19
f_3	0.73	0.91	1.00	0.86	0.67	0.56	0.46	0.33	0.23
f_4	0.72	0.76	0.86	1.00	0.80	0.66	0.55	0.48	0.30
f_5	0.64	0.66	0.67	0.80	1.00	0.82	0.70	0.49	0.44
f_6	0.52	0.55	0.56	0.66	0.82	1.00	0.85	0.66	0.60
f_7	0.37	0.42	0.46	0.55	0.70	0.85	1.00	0.87	0.87
f_8	0.22	0.23	0.33	0.48	0.49	0.66	0.87	1.00	0.85
f_9	0.16	0.19	0.23	0.30	0.44	0.60	0.87	0.85	1.00

Table 6.6: Relative flux correlation coefficients from the neutrino beam Monte Carlo tuned with the SHINE data. There is a strong positive correlation between the flux in the various energy bins.

subsection 6.4.3 on the whole Monte Carlo sample. Finally we do the validation on MC samples with the same number of events as in the data sample to check the statistical effect in subsection 6.4.4.

6.4.1 Flux fit validation

The first step is to verify that, when fitting the flux factors only on the Monte Carlo sample, the fit returns results consistent with 1, which is the expected value. This is indeed the case, as shown by the fit results on the data, summarised in table 6.7 for the simultaneous fit on topologies 1 and 2, and in table 6.8 for the fit on topology 2 only. The latter fit gives of course less precise results, especially at low energy, where the statistics in the topology 2 sample is low There is an anticorrelation between the flux factors in neighbouring energy bins. This is due to the energy resolution, causing migration of events from one energy bin to its neighbours.

The fit is then repeated when adding the beam constraint, which on the contrary gives a positive correlation between the flux factors. The fit results on the data are shown in table 6.9 for the simultaneous fit on topologies 1 and 2, and in table 6.10 for the fit on topology 2 only. Adding the beam constraint does reduce the errors and allows the fit using the topology 2 sample only to be nearly as good as the fit of both samples, except at very low neutrino energy, where

	result	parabolic error	negative error	positive error
Flux factors				
f_1	1.00	0.01	-0.01	$+0.01$
f_2	1.00	0.01	-0.01	$+0.01$
f_3	0.99	0.01	-0.01	$+0.01$
f_4	1.01	0.03	-0.04	$+0.04$
f_5	1.01	0.07	-0.09	$+0.09$
f_6	1.00	0.09	-0.14	$+0.14$
f_7	0.99	0.07	-0.11	$+0.11$
f_8	1.01	0.08	-0.11	$+0.11$
f_9	1.00	0.08	-0.10	$+0.10$

Table 6.7: Result on the flux factors for the flux-only fit on topology 1 and 2 events for the whole MC sample.

	result	parabolic error	negative error	positive error
Flux factors				
f_1	1.11	0.18	-0.19	$+0.19$
f_2	1.00	0.07	-0.08	$+0.08$
f_3	1.00	0.07	-0.07	$+0.07$
f_4	1.04	0.10	-0.12	$+0.12$
f_5	0.96	0.14	-0.19	$+0.19$
f_6	1.01	0.16	-0.23	$+0.23$
f_7	0.99	0.10	-0.14	$+0.14$
f_8	1.01	0.10	-0.13	$+0.13$
f_9	1.00	0.09	-0.11	$+0.11$

Table 6.8: Result on the flux factors for the flux-only fit on topology 2 events for the whole MC sample.

there is not enough statistics.

	result	parabolic error	negative error	positive error
Flux factors				
f_1	1.00	0.01	−0.01	+0.01
f_2	1.00	0.01	−0.01	+0.01
f_3	1.00	0.01	−0.01	+0.01
f_4	1.01	0.02	−0.02	+0.02
f_5	1.01	0.02	−0.02	+0.02
f_6	1.00	0.03	−0.03	+0.03
f_7	1.00	0.02	−0.02	+0.02
f_8	1.00	0.04	−0.04	+0.04
f_9	1.00	0.05	−0.05	+0.05

Table 6.9: Result on the flux factors for the flux-only fit with beam constraint on topology 1 and 2 events for the whole MC sample.

	result	parabolic error	negative error	positive error
Flux factors				
f_1	1.03	0.05	−0.05	+0.05
f_2	1.02	0.02	−0.02	+0.02
f_3	1.01	0.02	−0.02	+0.02
f_4	1.01	0.03	−0.03	+0.03
f_5	1.00	0.03	−0.03	+0.03
f_6	0.99	0.03	−0.03	+0.03
f_7	0.99	0.02	−0.02	+0.02
f_8	1.01	0.04	−0.04	+0.04
f_9	1.00	0.05	−0.05	+0.05

Table 6.10: Result on the flux factors for the flux-only fit with beam constraint on topology 2 events for the whole MC sample.

6.4.2 CCDIS cross section validation

The next cross-check is to check that when fitting the CCDIS cross section factors only on the Monte Carlo sample, the fit returns results consistent with 1, which is

the expected value. This is also the case, as shown by the fit results, summarised in table 6.11 when using both topologies 1 and 2, and in table 6.12 when using only topology 2. The errors on the cross section for CCDIS increase only slightly when we use topology 2 only compared to the use of both topologies. Indeed, most of the CCDIS neutrino interactions have more than two tracks and thus are selected in topology 2.

	result	parabolic error	negative error	positive error
Cross section factors				
F_2	1.017	0.033	−0.033	+0.034
F_3	0.982	0.033	−0.033	+0.033
F_4	1.005	0.019	−0.019	+0.019

Table 6.11: Result on the CCDIS cross section factors for the cross section-only fit on topology 1 and 2 events for the whole MC sample.

	result	parabolic error	negative error	positive error
Cross section factors				
F_2	1.031	0.033	−0.033	+0.037
F_3	0.982	0.033	−0.033	+0.035
F_4	1.005	0.019	−0.019	+0.019

Table 6.12: Result on the CCDIS cross section factors for the cross section-only fit on topology 2 events for the whole MC sample.

6.4.3 Combined fit validation

We now perform the fit of both flux factors and CCDIS cross section factors using the beam constraint for topology 1 and topology 2 events together The result is shown in table 6.13. It is illustrated in figure 6.8 as a function of the two topologies and figure 6.9 as a function of the four interaction types. There is a very good agreement on the neutrino measured energy distributions between the prediction and the fit result on the Monte Carlo.

	result	parabolic error	negative error	positive error
Flux factors				
f_1	1.00	0.01	−0.01	+0.01
f_2	1.00	0.01	−0.01	+0.01
f_3	0.99	0.01	−0.01	+0.01
f_4	1.00	0.02	−0.02	+0.02
f_5	1.01	0.03	−0.03	+0.03
f_6	1.01	0.04	−0.03	+0.03
f_7	1.01	0.03	−0.03	+0.03
f_8	0.99	0.06	−0.05	+0.05
f_9	0.99	0.07	−0.06	+0.06
Cross section factors				
F_2	1.03	0.05	−0.05	+0.05
F_3	0.94	0.06	−0.06	+0.06
F_4	1.02	0.07	−0.05	+0.06

Table 6.13: Result on the flux factors and the CCDIS cross section factors for the nominal fit on topology 1 and 2 events for the whole MC sample.

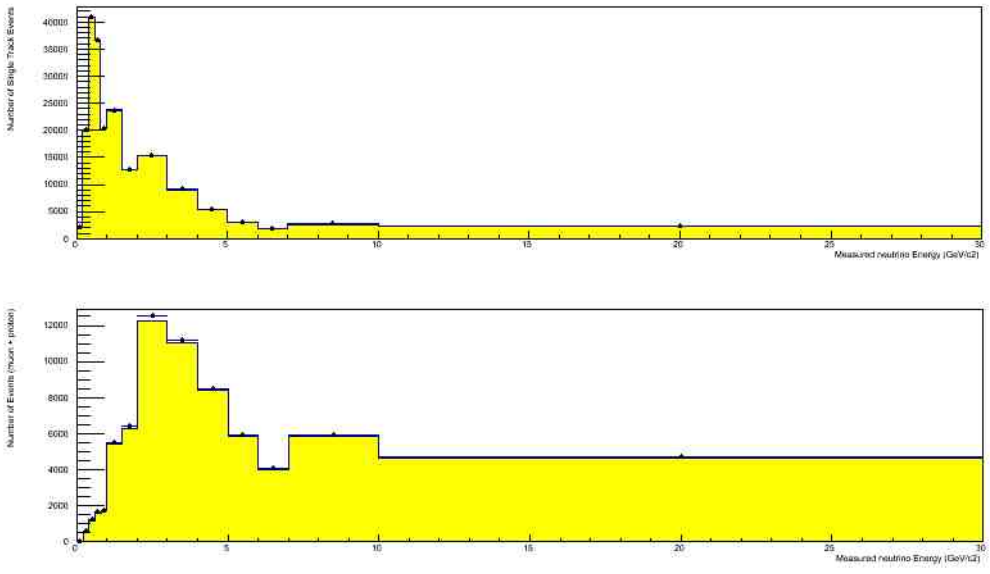

Figure 6.8: Distribution of the neutrino measured energy for (top) topology 1 and (bottom) topology 2 events. The points show the fit results, while the histograms show the expected MC distributions.

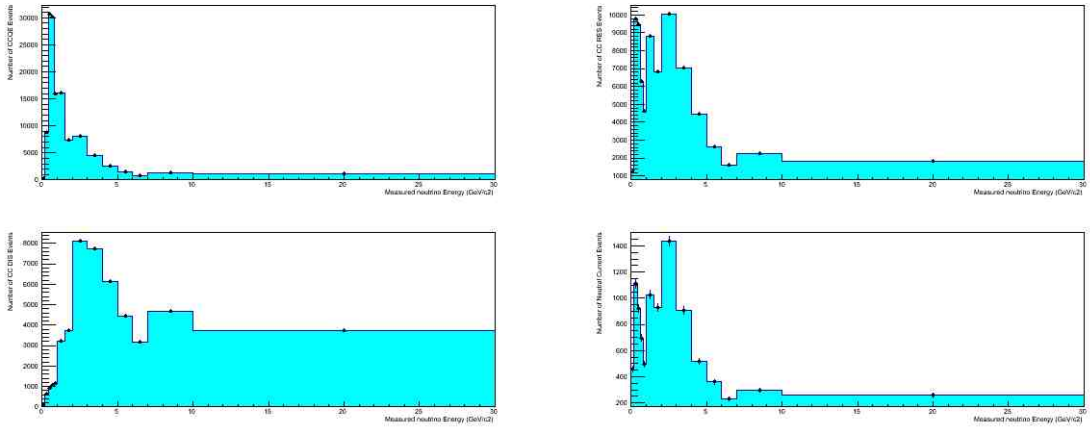

Figure 6.9: Distribution of the neutrino measured energy for (top left) CCQE, (top right) CCRES, (bottom left) CCDIS, and (bottom right) NC events. The points show the fit results, while the histograms show the expected MC distributions.

The errors on the CCDIS cross section factors are somewhat larger for the combined fit than for the CCDIS cross section only fit. This is due to the fact that for the combined fit, the error is not purely statistical, but includes also the systematic error due to the flux through the beam constraint. This flux systematic error can be estimated by calculating the quadratic difference between the error from the combined fit and the error from the cross section-only fit. It is given in table 6.14. This error is smaller than the systematic error we would get by doing a CCDIS cross section-only fit and varying the flux prediction by its uncertainties, which were given in table 6.1. This demonstrates that it is better to do the combined fit with the beam constraint, which has the advantage of taking into account the correlations between the flux in the different neutrino energy bins.

Cross section factor	topo 1 & 2	topo 2
F_2	0.04	0.13
F_3	0.05	0.18
F_4	0.07	0.25

Table 6.14: Systematic error due to the flux uncertainty on the CCDIS cross section factors.

The result of the same fit using only toplogy 2 events is shown in table 6.15. All the fitted parameters are still compatible with 1, the expected value. However we can see that the errors on both the flux factors and the cross section factors are substantially larger, by about a factor three. This shows that topology 1 events, even if they do not contribute directly in the CCDIS cross section measurement, play a big role by constraining the flux factors (correlated to the CCDIS cross section factors).

	result	parabolic error	negative error	positive error
Flux factors				
f_1	1.03	0.05	−0.05	+0.05
f_2	1.02	0.02	−0.02	+0.02
f_3	1.01	0.03	−0.03	+0.03
f_4	1.01	0.06	−0.05	+0.05
f_5	1.01	0.07	−0.07	+0.07
f_6	1.01	0.10	−0.09	+0.09
f_7	1.01	0.15	−0.13	+0.13
f_8	1.01	0.21	−0.19	+0.19
f_9	1.01	0.20	−0.18	+0.18
Cross section factors				
F_2	0.99	0.13	−0.12	+0.13
F_3	0.96	0.18	−0.15	+0.18
F_4	0.99	0.25	−0.19	+0.27

Table 6.15: Result on the flux factors and the CCDIS cross section factors for the nominal fit on topology 2 events for the whole MC sample.

6.4.4 Results on MC samples

The aim here is to have the same statistics as in the the data. Thus we divide the whole MC sample into six subsamples, each having the same number of events as the data sample. The nominal fit is repeated on topology 2 events on each subsample. The results are given in table 6.16.

The errors obtained on the full MC result are of course smaller than the ones obtained on the subsamples. However, they decrease more slowly than $1/\sqrt{N}$.

Subsample	F_2	F_3	F_4
1	$0.83^{+0.18}_{-0.17}$	$1.08^{+0.21}_{-0.18}$	$0.91^{+0.26}_{-0.19}$
2	$1.08^{+0.20}_{-0.18}$	$0.92^{+0.20}_{-0.17}$	$1.08^{+0.33}_{-0.23}$
3	$1.01^{+0.20}_{-0.18}$	$1.02^{+0.21}_{-0.18}$	$0.95^{+0.27}_{-0.19}$
4	$1.15^{+0.21}_{-0.19}$	$0.88^{+0.20}_{-0.17}$	$1.11^{+0.31}_{-0.22}$
5	$0.89^{+0.19}_{-0.17}$	$0.95^{+0.20}_{-0.17}$	$1.00^{+0.28}_{-0.20}$
6	$1.03^{+0.19}_{-0.18}$	$0.91^{+0.19}_{-0.16}$	$0.96^{+0.28}_{-0.19}$

Table 6.16: Result on the CCDIS cross section factors for the nominal fit on topology 2 events for the six MC subsamples.

This is because the error is not simply the statistical error, but contains a part of systematical nature, because of the beam constraint.

	Topo 2		Topo 1 and 2	
	result	error	result	error
Flux factors				
f_1	1.03	0.07	1.00	0.02
f_2	1.04	0.04	1.00	0.01
f_3	1.04	0.05	1.00	0.02
f_4	1.03	0.06	1.00	0.03
f_5	1.02	0.07	1.01	0.04
f_6	1.02	0.10	1.00	0.05
f_7	1.03	0.13	1.00	0.04
f_8	1.02	0.20	1.00	0.09
f_9	1.01	0.19	1.00	0.09
Cross section factors				
F_2	1.03	-0.18 / $+0.19$	1.12	0.12
F_3	0.91	-0.16 / $+0.19$	0.93	0.12
F_4	0.96	-0.19 / $+0.28$	0.99	0.11

Table 6.17: Result on the flux factors and the CCDIS cross section factors for the nominal fit on topology 2 events for the MC subsample number 6.

We also give in table 6.17 the compared results of the fit on topology 2 only and on both topologies simultaneously on one Monte Carlo subsample. Using both topologies allows the reduction of the errors by a factor two on the flux factors (and even more at small neutrino energy) and by a factor 1.6 on the

CCDIS cross section factors (and even more at high neutrino energy). The correlation coefficient for all fitted parameters are given in table 6.18 in the two fit configurations. We observe that, while there is a negative correlation between neighbouring energy bins for the flux and cross section factors when fitting both topologies 1 and 2, there is a positive one when fitting topology 2 only. The effect is the same on the whole Monte Carlo sample. It can also be seen that the mostly negative correlations between the the flux factors and CCDIS cross section factors are stronger for topology 2 alone than for topologies 1 and 2 together. The decrease of these correlations is another advantage of the simultaneous use of both topologies, resulting in a more stable fit.

	Topology 2											
	f_1	f_2	f_3	f_4	f_5	f_6	f_7	f_8	f_9	F_2	F_3	F_4
f_1	1.00	0.53	0.05	0.27	0.24	0.14	0.06	0.03	0.01	-0.25	-0.09	-0.03
f_2	0.53	1.00	0.49	0.13	0.15	0.06	-0.02	-0.11	-0.07	-0.30	0.05	0.07
f_3	0.05	0.49	1.00	0.59	0.33	0.23	0.21	0.22	0.16	-0.65	-0.09	-0.22
f_4	0.27	0.13	0.59	1.00	0.73	0.59	0.54	0.57	0.45	-0.84	-0.47	-0.54
f_5	0.24	0.15	0.33	0.73	1.00	0.82	0.75	0.64	0.63	-0.75	-0.76	-0.65
f_6	0.14	0.06	0.23	0.59	0.82	1.00	0.90	0.81	0.79	-0.63	-0.90	-0.82
f_7	0.06	-0.02	0.21	0.54	0.75	0.90	1.00	0.94	0.95	-0.59	-0.87	-0.96
f_8	0.03	-0.11	0.22	0.57	0.64	0.81	0.94	1.00	0.94	-0.57	-0.78	-0.98
f_9	0.01	-0.07	0.16	0.45	0.63	0.79	0.95	0.94	1.00	-0.51	-0.77	-0.97
F_2	-0.25	-0.30	-0.65	-0.84	-0.75	-0.63	-0.59	-0.57	-0.51	1.00	0.40	0.58
F_3	-0.09	0.05	-0.09	-0.47	-0.76	-0.90	-0.87	-0.78	-0.77	0.40	1.00	0.75
F_4	-0.03	0.07	-0.22	-0.54	-0.65	-0.82	-0.96	-0.98	-0.97	0.58	0.75	1.00
	Topologies 1 & 2											
	f_1	f_2	f_3	f_4	f_5	f_6	f_7	f_8	f_9	F_2	F_3	F_4
f_1	1.00	-0.35	-0.21	0.20	-0.01	-0.03	-0.07	0.06	-0.05	-0.02	0.01	0.00
f_2	-0.35	1.00	-0.04	-0.28	0.07	0.07	0.05	-0.15	0.02	0.02	-0.03	0.06
f_3	-0.21	-0.04	1.00	0.26	-0.09	-0.12	-0.07	0.06	-0.02	-0.46	0.28	-0.07
f_4	0.20	-0.28	0.26	1.00	0.11	-0.15	-0.23	0.18	-0.15	-0.56	0.21	-0.03
f_5	-0.01	0.07	-0.09	0.11	1.00	0.18	0.02	-0.33	-0.14	-0.25	-0.32	0.28
f_6	-0.03	0.07	-0.12	-0.15	0.18	1.00	0.18	-0.20	-0.19	0.11	-0.58	0.20
f_7	-0.07	0.05	-0.07	-0.23	0.02	0.18	1.00	0.38	0.61	0.14	-0.32	-0.56
f_8	0.06	-0.15	0.06	0.18	-0.33	-0.20	0.38	1.00	0.49	-0.06	0.17	-0.81
f_9	-0.05	0.02	-0.02	-0.15	-0.14	-0.19	0.61	0.49	1.00	0.04	0.10	-0.75
F_2	-0.02	0.02	-0.46	-0.56	-0.25	0.11	0.14	-0.06	0.04	1.00	-0.51	0.11
F_3	0.01	-0.03	0.28	0.21	-0.32	-0.58	-0.32	0.17	0.10	-0.51	1.00	-0.32
F_4	0.00	0.06	-0.07	-0.03	0.28	0.20	-0.56	-0.81	-0.75	0.11	-0.32	1.00

Table 6.18: Correlation coefficients between the fitted variables returned by the combined fit on Monta Carlo subsample number 6.

Chapter 7

Analysis results

In this chapter, the fit that has been introduced and validated in chapter 6 is applied to the the data. Unfortunately, there is a disagreement between data and Monte Carlo in the topology 1 sample, explained in section 7.1, which prevents from using it in the fit. Section 7.2 presents the result of the fit on the data using the topology 2 sample. The systematic uncertainties are reviewed in section 7.3. Section 7.4 gives the physics results of this analysis. Finally, some perspectives are given in section 7.5.

7.1 Disagreement in topology 1

There is a disagreement between the data and the MC. It is illustrated on the distribution of neutrino measured energy in figure 7.1. While the data/MC agreement is good in the topology 2 sample, there is a significant difference in the topology 1 sample. The disagreement is further illustrated in figure 7.2, where the ratio data over MC is shown.

The origin of this disagreement has not yet been fully understood. One possible explanation is the multi-nucleon effect: after a neutrino interaction, several nucleons, and not only one proton, could be ejected from the stuck nucleus. It leads to a softer distribution of the muon momentum, since part of the available energy is taken away by the ejected nucleons. This multi-nucleon effect is not simulated in the Monte Carlo, while it may be present in the data. Indeed the

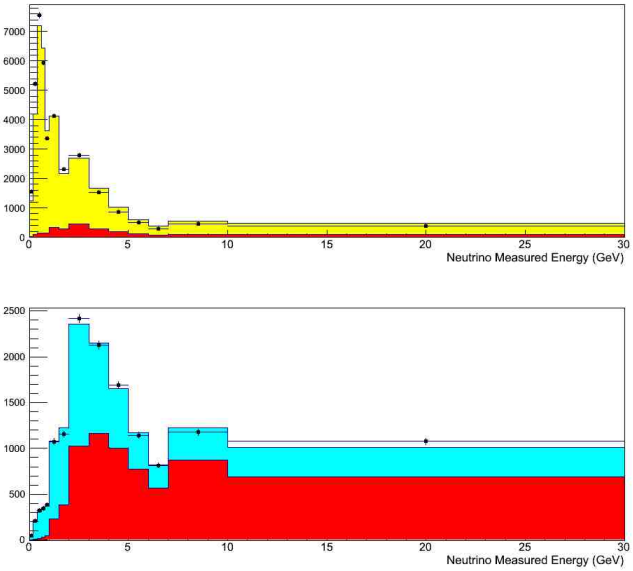

Figure 7.1: Distribution of the neutrino measured energy for (top) topology 1 and (bottom) topology 2 events. The points show the data, while the histograms show the MC distributions. In both plots, the red histogram shows the CCDIS contribution.

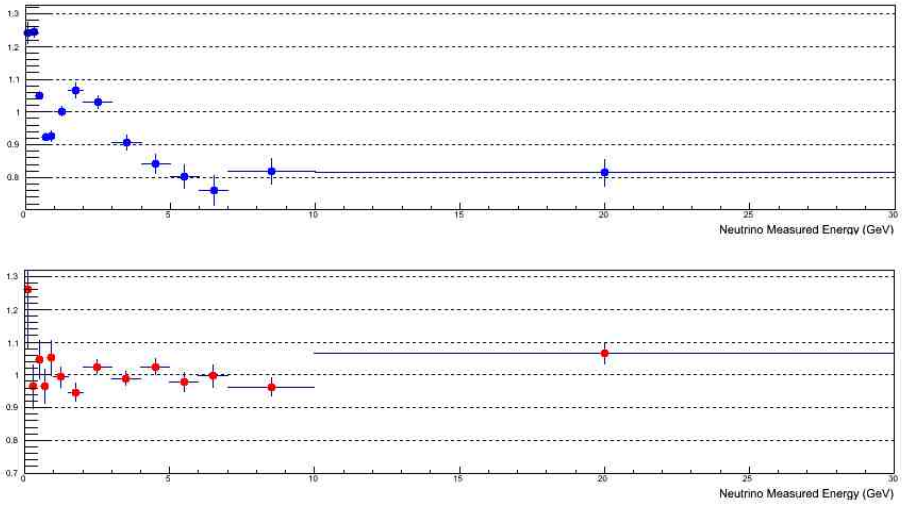

Figure 7.2: Ratio of data over MC as a function of the neutrino measured energy for (top) topology 1 and (bottom) topology 2 events.

momentum spectrum of the muon candidate is softer in the data than in the Monte Carlo.

As a consequence of the disagreement between data and Monte Carlo, the combined fit on topologies 1 and 2 does not give good results. The fit is adjusting the flux factors to correct for the disagreement between data and Monte Carlo and this introduces a bias on the CCDIS cross section measurement.

7.2 Result with topology 2

Thus, the final fit is chosen as the the simultaneous fit of the neutrino flux and CCDIS cross section factors using the beam constraint on the topology 2 sample. The results of the fit on data are given in table 7.1. The fitted flux factors are illustrated in figure 7.3. They are smaller than one, though compatible with that value. The goodness of the fit is shown by the comparison between the neutrino measured energy distribution and the fitted points in figure 7.4.

	result	error
Flux factors		
f_1	0.90	$\pm$ 0.07
f_2	0.87	$\pm$ 0.04
f_3	0.85	$\pm$ 0.04
f_4	0.87	$\pm$ 0.06
f_5	0.91	$\pm$ 0.07
f_6	0.90	$\pm$ 0.10
f_7	0.89	$\pm$ 0.14
f_8	0.85	$\pm$ 0.21
f_9	0.97	$\pm$ 0.18
Cross section factors		
F_2	1.19	$^{+0.22}_{-0.20}$
F_3	1.00	$^{+0.24}_{-0.19}$
F_4	1.09	$^{+0.36}_{-0.27}$

Table 7.1: Result of the nominal fit on topology 2 data events.

The statistical errors obtained on data are rather similar to the ones obtained on the Monte Carlo samples with the same statistics as the data, which were

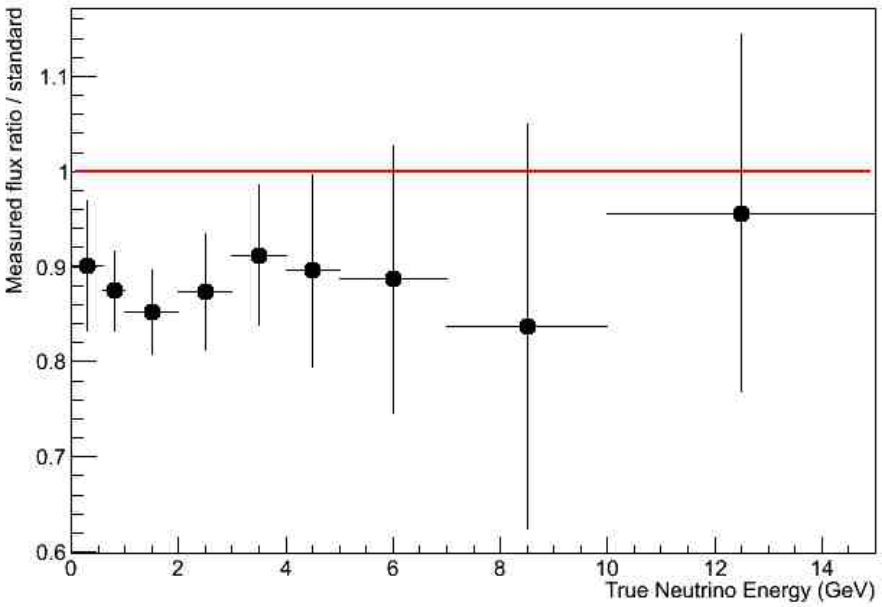

Figure 7.3: Flux factor values found by the fit as a function of neutrino energy.

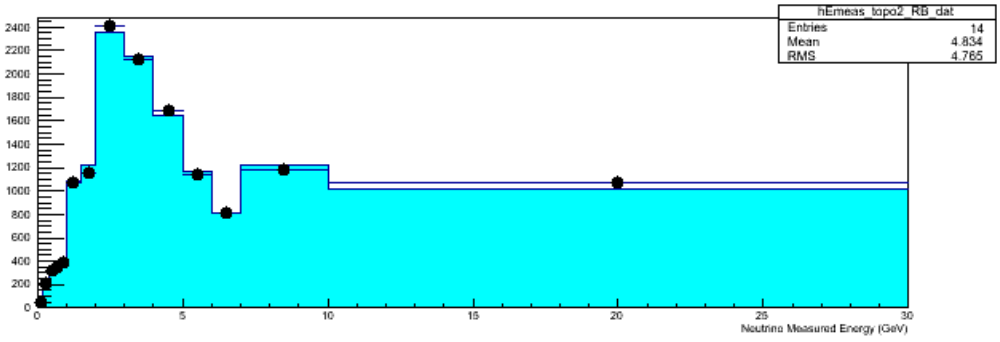

Figure 7.4: Distribution of the neutrino measured energy for topology 2 events. The points show the fit results, while the histograms show the data distribution.

given in subsection 6.4.4.

7.3 Systematic uncertainties

In this section, we review the main sources of systematic uncertainties for our charged current deep inelastic scattering cross section measurement. We start with the uncertainties induced by the out of FGD fiducial volume events. We then go through the cross-section related uncertainties for the various processes other than CCDIS, i.e. NC, CCQE, and CCRES. Finally, we calculate the total systematic uncertainties.

7.3.1 Out of FGD FV

The systematic error due to the out of FGD fiducial volume background is estimated by repeating the nominal fit when varying the fraction of out of FGD FV by 30 %. The variation observed on the CCDIS cross section factors are given in table 7.2.

Parameter	result		
out of FGD FV	-30 %	Nominal	+30 %
F_2	1.01	1.19	1.38
F_3	0.91	1.00	1.10
F_4	1.01	1.09	1.17

Table 7.2: Variation of the fit results with the out of FGD background fraction.

7.3.2 NC

According to table 6.2, the neutral current cross sections that are used in the fit are varied by 36 %. The effect on the fitted CCDIS cross section factors are given in table 7.3.

Parameter	result		
NC	-36 %	Nominal	+36 %
F_2	1.23	1.19	1.16
F_3	0.97	1.00	1.04
F_4	1.06	1.09	1.13

Table 7.3: Variation of the fit results with the NC cross section.

7.3.3 CCQE

Similarly, the charged current quasi-elastic cross sections are varied by 25 %. The effect on the fitted CCDIS cross section factors are given in table 7.4.

Parameter	result		
CCQE	-25 %	Nominal	+25 %
F_2	1.10	1.19	1.28
F_3	0.95	1.00	1.05
F_4	1.05	1.09	1.13

Table 7.4: Variation of the fit results with the CCQE cross section.

7.3.4 CCRES

Finally, the charged current resonant (single pion) cross sections are allowed to vary by 31 %. The effect on the fitted CCDIS cross section factors are given in table 7.5.

Parameter	result		
CCRES	-31 %	Nominal	+31 %
F_2	1.24	1.19	1.14
F_3	0.99	1.00	0.99
F_4	1.05	1.09	1.12

Table 7.5: Variation of the fit results with the CCRES cross section.

7.3.5 Total systematic

The total systematic error is calculated by adding in quadrature the errors due to the main sources explained above. This is summarised in table 7.6. The systematic uncertainty decreases with the neutrino energy, unlike the statistical uncertainty. Both are comparable in the first energy bin. Then the statistical error dominates.

Parameter	outFGD	CCQE	CCRES	NC	total
F_2	15.6	7.5	4.4	2.7	18.1
F_3	9.6	5.0	1.1	3.6	11.4
F_4	7.2	3.8	3.4	3.4	9.5

Table 7.6: Systematic uncertainties (in %) on the CCDIS cross section measurement.

Taking into account the systematic uncertainty, the correction factors to the predicted charged current deep inelastic scattering ν_μ cross section in three neutrino energy bins which we measure are the follwing.

- for $2 < E < 4$ GeV, $F_2 = 1.19^{+0.22}_{-0.20} \pm 0.21$,
- for $4 < E < 6$ GeV, $F_3 = 1.00^{+0.24}_{-0.19} \pm 0.11$,
- for $E > 6$ GeV, $F_4 = 1.09^{+0.36}_{-0.27} \pm 0.10$.

7.4 Physics results

Using the predicted CCDIS cross sections given in table 6.3, the results of the fit reported in table 7.1, and the systematic uncertainties summarised in table 7.6, we can calculate the CCDIS cross sections that we measure. We have to assume that the fitted correction factors are the same for all target nuclei types. In principle, performing the analysis separately for FGD1 and FGD2, where the oxygen content is not the same, could bring some additional information. This can be a future development of the analysis. The measured CCDIS ν_μ cross sections are given with their statistical and systematic errors for the three energy

bins that have been considered in table 7.7 for carbon targets, in table 7.8 for hydrogen targets, and in table 7.9 for oxygen targets.

Energy range (GeV)	Cross section	Statistical uncertainty	Systematic uncertainty
2.0-4.0	0.15	$+0.03/-0.02$	± 0.03
4.0-6.0	0.29	$+0.07/-0.05$	± 0.03
6.0-10.0	0.58	$+0.19/-0.13$	± 0.06

Table 7.7: Measurement of the CCDIS ν_μ cross sections on carbon in 10^{-36} cm^2/atom for different bins of neutrino energy.

Energy range (GeV)	Cross section	Statistical uncertainty	Systematic uncertainty
2.0-4.0	0.008	$+0.002/-0.001$	± 0.001
4.0-6.0	0.015	$+0.004/-0.003$	± 0.002
6.0-10.0	0.032	$+0.010/-0.007$	± 0.003

Table 7.8: Measurement of the CCDIS ν_μ cross sections on hydrogen in 10^{-36} cm^2/atom for different bins of neutrino energy.

Energy range (GeV)	Cross section	Statistical uncertainty	Systematic uncertainty
2.0-4.0	0.20	$+0.04/-0.03$	± 0.04
4.0-6.0	0.38	$+0.09/-0.07$	± 0.04
6.0-10.0	0.77	$+0.26/-0.17$	± 0.07

Table 7.9: Measurement of the CCDIS ν_μ cross sections on oxygen in 10^{-36} cm^2/atom for different bins of neutrino energy.

7.5 Perspectives

We finish this thesis by giving a few perspectives to continue and improve the analysis.

7.5.1 Improving the selection

We have seen in subsection 5.2.1.6 that the selection can probably be improved, in particular the particle identification of the muon candidate. Table 7.10 summarises the effect of the muon pull cut and of the electron pull cut, in terms of efficiencies and of fractions before and after the cut for the various particle types.

	Fraction (%)			Efficiency (%)	
particle	Before cut	$\mid \delta^{\mu} \mid < 2.5$	$\mid \delta^{\mu} \mid < 2.5$ & $\mid \delta^{e} \mid > 2$	$\mid \delta^{\mu} \mid < 2.5$	$\mid \delta^{e} \mid > 2$
muon	77.2	89.8	91.7	97.4	89.3
electron	9.8	2.1	0.2	18.1	7.9
pion	8.4	7.5	7.7	74.6	90.3
proton	4.5	0.5	0.3	9.5	58.3
unkown	0.1	0.1	0.1	76.9	91.0
Total	100.0	100.0	100.0	83.8	87.5

Table 7.10: Effect of the cuts on the muon pull and on the electron pull respectively.

Compared to our current PID selection described in subsection 5.2.1.6, the fraction of muons in the selected sample can be improved by rejecting nearly all electrons and protons. However, in order not to lose efficieny on high energetic muons while rejecting low momentum background tracks, a momentum dependent cut may be considered.

7.5.2 Better understanding of topology 1 sample

The validation studies in section 6.4 have clearly established that the simultaneous fit of both topologies leads to smaller uncertainties than the fit on topology 2 only. A gain by a factor larger than 1.6 is obtained on Monte Carlo samples. However the disagreement observed between data and Monte Carlo in topology 1 events prevented us from using topology 1 in the final fit on the data.

Thus, it is crucial to understand the origin of this disagreement in order to fix it and be able to use the more powerful fit using both topologies. We have seen that the multi-nucleon effect, which is not simulated in the Monte Carlo, may be the cause of the problem.

7.5.3 Technical improvements

Instead of the energy resolution parametrisation described in subsection 6.1.2, we can fit the energy resolution with an appropriate analytical function, for example a triple Gaussian. This should limit the effect of the statistical fluctuations of the Monte Carlo on the fit result.

7.5.4 Dividing the topology 2 sample

We have started to explore another way to extract more information from the data sample. The idea is to divide the topology 2 category itself into two samples:

- the events with exactly three tracks,
- the events with four tracks or more.

In fact, these two samples contain quite different fractions of CCDIS events, our signal, and of CCRES events, the main remaining background. While the sample of events with exactly three tracks has about 32 % CCDIS events and a lot of CCRES events, the sample of events with four tracks or more is depleted in CCRES events and enriched in CCDIS events, since it contains about 53 % of them. It was checked also that this fraction does not vary much when requiring more tracks. So it is not really useful to subdivide the sample even more.

We can also consider using cuts on discriminating variables, that have different distributions for CCDIS events and non-CCDIS events. The sum of the momentum modules of all tracks in the event except the muon candidate could be such a discriminating variable.

7.5.5 Measuring the cross section of neutrino interaction with at least one neutral pion

Using the selection of events with one muon and one electron or positron, introduced in section 5.3, and a similar approach as the one used in the CCDIS cross section measurement, we could fit:

- the exclusive $CC1\pi^0$ cross section, using low multiplicity events.

- the inclusive cross section of CC events with at least one π^0. As this sample is dominated by CCDIS events, this could give the fraction of CCDIS event, where a π^0 is produced.

Conclusion

This thesis describes the work done from February 2011 to June 2014 within the T2K collaboration at the particle physics division of the institute of research into the fundamental laws of the Universe at CEA-Saclay. T2K is a neutrino experiment taking place in Japan.

During my thesis, I was in charge of the data quality of the time projection chambers in 2012 and 2013. The three TPCs are a crucial element of the ND280 near detector of the T2K experiment. Therefore it is important to make sure that they are working properly. The various checks performed to control the data quality have been presented in this thesis. The overall efficiency of the data quality requirements for the whole ND280 detector is good, higher than 90 %, and has improved with time.

The main analysis described in this thesis is a measurement of the charged current deep inelastic scattering ν_μ cross section. It uses the whole dataset recorded by the T2K experiment. It is based on a sample of inclusive charged current ν_μ interactions, selected by identifying a muon candidate: an energetic track with a long enough TPC segment corresponding to a negatively charged particle and satisfying particle identification requirements. This sample is then divided into two parts according to the number of detected tracks in the event. In particular, we obtain a sample enriched in deep inelastic scattering events by requiring at least three tracks in the event. A fitting program has been build to extract from this sample the values of the charged current deep inelastic scattering ν_μ cross section. It is first validated on simulated samples and then applied to the data. The results are given as correction factors to the predicted charged current deep inelastic scattering ν_μ cross section in three neutrino energy bins (the first error is statistical and the second one is systematic):

- for $2 < E < 4$ GeV, $F_2 = 1.19^{+0.22}_{-0.20} \pm 0.21$,
- for $4 < E < 6$ GeV, $F_3 = 1.00^{+0.24}_{-0.19} \pm 0.11$,
- for $6 < E < 10$ GeV, $F_4 = 1.09^{+0.36}_{-0.27} \pm 0.10$.

They lead to the measurements of the charged current deep inelastic ν_μ cross sections summarised in the following table.

Energy (GeV)	Carbon	Hydrogen	Oxygen
2.0-4.0	$0.15^{+0.03}_{-0.02} \pm 0.03$	$0.008^{+0.002}_{-0.001} \pm 0.001$	$0.20^{+0.04}_{-0.03} \pm 0.04$
4.0-6.0	$0.29^{+0.07}_{-0.05} \pm 0.03$	$0.015^{+0.004}_{-0.003} \pm 0.002$	$0.38^{+0.09}_{-0.07} \pm 0.04$
6.0-10.0	$0.58^{+0.19}_{-0.13} \pm 0.06$	$0.032^{+0.010}_{-0.007} \pm 0.003$	$0.77^{+0.26}_{-0.17} \pm 0.07$

Table 7.11: Measurement of the CCDIS ν_μ cross sections on carbon, hydrogen and oxygen in 10^{-36} cm^2/atom for different bins of neutrino energy.

References

[1] W. Pauli. *Physics Today*, 31:27, 1978. 4

[2] E. Fermi. *Z. Phys.*, 88:161, 1934. 4

[3] C.L. Cowan et al. *Science*, 124:103, 1956. 4

[4] G. Danby et al. *Phys. Rev. Lett.*, 9:36, 1962. 4

[5] D. Decamo et al. *Phys. Lett. B*, 276:247, 1991. 5, 6

[6] K. Kodama et al. *Phys. Lett. B*, 504:218, 2001. 6

[7] R.J. Davis et al. *Phys. Rev. Lett.*, 20:1205, 1968. 6

[8] J.N. Abdurashitov et al. *Astropart. Phys.*, 25:7, 2006. 6

[9] W. Hampel et al. *Phys. Lett. B*, 420:114, 1998. 6

[10] M. Altmann et al. *Phys. Lett. B*, 616:174, 2005. 6

[11] K.S. Hirata et al. *Phys. Rev. Lett.*, 63:16, 1989. 6

[12] S. Fukuda et al. *Phys. Rev. Lett.*, 86:5651, 2001. 6

[13] Q.R. Ahmad et al. *Phys. Rev. Lett.*, 87:071301, 2001. 7

[14] Y. Fukuda et al. *Phys. Rev. Lett.*, 81:8, 1998. 9, 10

[15] N. Agafonova et al. *Phys. Lett. B*, 691:138, 2010. 10, 11

[16] B. Pontecorvo. *Zh. Eksp. Teor. Fiz.*, 34:247, 1958. 11

[17] N. Nakagawa Z. Maki and S. Sakata. *Prog. Theor. Phys.*, 28:870, 1962. 11

[18] M. Kobayashi and T. Maskawa. *Prog. Th. Phys.*, 49:652, 1973. 12

[19] K. Eguchi. *Phys. Rev. Lett.*, 90:021802, 2003. 13

[20] S. Abe. *Phys. Rev. Lett.*, 100:22, 2008. 13

[21] A. Gando et al. *Phys. Rev. D*, 83:052002, 2011. 14

[22] E. Aliu et al. *Phys. Rev. Lett.*, 94:081802, 2005. 14

[23] P. Adamson et al. *Phys. Rev. Lett.*, 97:191801, 2006. 14

[24] K. Abe et al. *Phys. Rev. Lett.*, arXiv:1403.1532, 2014. 14, 15

[25] K. Abe et al. *Phys. Rev. Lett.*, 112:061802, 2014. 16, 17

[26] Y. Abe et al. *Phys. Rev. D*, 86:052008, 2012. 17

[27] F.P. An et al. *Phys. Rev. Lett.*, 108:171803, 2012. 17

[28] J.K. Ahn et al. *Phys. Rev. Lett.*, 108:191802, 2012. 17

[29] E.J. Moniz and R.A. Smith. *Nucl. Phys. B*, 43:605, 1972. 19

[30] Y. Hayato. *Nucl. Phys. Proc. Suppl.*, 112:171, 2002. 19, 84, 149

[31] G.P. Zeller. *Proceedings of third NO-VE workshop*, page 103, 2006. 20, 21

[32] O. Benhar. *Acta Phys. Pol. B*, 40:2389, 2009. 21

[33] E.J. Moniz et al. *Phys. Rev. Lett.*, 26:445, 1971. 22

[34] C.H. Llewelyn-Smith. *Phys. Rep. C*, 3:261, 1972. 22

[35] A.A. Aguilar-Arevalo et al. *Phys. Rev. D*, 81:092005, 2010. 23

[36] F. Blaszczyk. Phd thesis. 2011. 23, 27, 49, 147

[37] R. Bradford et al. *J. Phys. Conf. Ser.*, 110:082004, 2008. 23

[38] V. Lyubushkin et al. *Eur. Phys. J. C*, 63:355, 2009. 23

[39] D. Rein et L.M. Sehgal. *Annals Phys.*, 133:79, 1981. 24

[40] A.A. Aguilar-Arevalo et al. *Phys. Rev. Lett.*, 103:081801, 2009. 24

[41] M. Tzanov. *AIP Conf. Proc.*, 1222:243, 2010. 26

[42] K. Abe et al. *Nucl. Instrum. Meth. A*, 659:106, 2011. 28

[43] N. Abgrall et al. *CERN-PH-EP-2014-003*, 2014. 31, 146

[44] M. Otani et al. *Nucl. Instrum. Meth. A*, 623:368, 2010. 33

[45] S. Assylbekov et al. *Nucl. Instrum. Meth. A*, 686:48, 2012. 36

[46] P.A. Amaudruz et al. *Nucl. Instrum. Meth. A*, 696:1, 2012. 36

[47] D. Allan et al. *J. Inst.*, 8:P10019, 2013. 37

[48] S. Aoki et al. *Nucl. Instrum. Meth. A*, 698:135, 2013. 37

[49] Y. Fukuda et al. *Nucl. Instrum. Meth. A*, 501:418, 2003. 38

[50] P.A. Cerenkov. *Phys. Rev.*, 52:378, 1937. 39

[51] D.R. Nygren and J.N. Marx. *Phys. Today*, 31N10:46, 1978. 43

[52] I. Giomataris et al. *Nucl. Instrum. Meth. A*, 560:405, 2006. 46

[53] N. Abgrall et al. *Nucl. Instrum. Meth. A*, 637:25, 2011. 47

[54] C. Andreopoulos et al. *Nucl. Instrum. Meth. A*, 614:87, 2010. 84

[55] S. Agostinelli et al. *Nucl. Instrum. Meth. A*, 506:250, 2003. 84

[56] C. Giganti. Phd thesis. 2010. 92, 96

[57] K. Abe et al. *Phys. Rev. D*, 87:012001, 2013. 146, 147